Simulation of Ultrashort Laser Pulse Propagation and Plasma Generation in Nonlinear Media

by

Jeremy R. Gulley

(Under the direction of William M. Dennis)

Abstract

In this dissertation, a modified nonlinear Schrödinger equation is derived, which describes the propagation of ultrashort laser pulses through nonlinear materials in which plasma generation and laser-induced damage can occur. Differences between this model and models currently used in the literature are investigated and analyzed by numerical simulations. Ultrafast laser-induced material modification is investigated using this method by simulating the propagation of fully 3+1D (3 spatial plus 1 time dimension) laser pulses, which are numerically constructed from experimentally measured beam profiles and pulse shape data. The latest of these investigations reveals that standard rate-equation models for the free-electron plasma generation in the material may not adequately describe ultrafast plasma dynamics, and possible solutions for this problem are discussed. It is expected that a better understanding of the dynamics of ultrashort laser pulse-induced plasma will enable the accurate simulation of optical damage in a variety of dielectrics, ultimately leading to an enhanced control of laser-induced modification to real materials and optical devices.

Index words: Ultrashort, Ultrafast, Nonlinear Optics, Femtosecond Pulses, Plasma Generation, Laser-induced Damage, Nonlinear Schrödinger Equation

Simulation of Ultrashort Laser Pulse Propagation and Plasma Generation in Nonlinear Media

by

Jeremy R. Gulley

B.S., Furman University, 2003

A Thesis Submitted to the Graduate Faculty
of The University of Georgia in Partial Fulfillment
of the
Requirements for the Degree

Doctor of Philosophy

Athens, Georgia

2009

Simulation of Ultrashort Laser Pulse Propagation and Plasma Generation in Nonlinear Media

by

Jeremy R. Gulley

Approved:

Major Professor: William M. Dennis

Committee: Steven P. Lewis
Susanne Ullrich
Craig Wiegert

Electronic Version Approved:

Maureen Grasso
Dean of the Graduate School
The University of Georgia
May 2009

Dedication

To my parents. It is impossible to repay you for all that you have done for me.

Acknowledgments

I would first like to thank the U.S. Air Force Research Laboratory for the many years of funding and the opportunities it has provided for my research. On the same token I wish to thank the Graduate School of The University of Georgia for the funding I have received in my final year at the University of Georgia through the Doctoral Completion Assistantship. I especially wish to thank the family of Bill Cummings and the benefactors of the James L. Carmon Award. I am most honored to have been the recipient of their goodwill.

I wish to extend my personal gratitude to the graduate students of the Dennis research group. To Sarah and Mohua for the many arduous talks of mine you've had sit through. To Carl, first my graduate student mentor and later my peer who has now graduated and moved on. To Tom, who has time and time again performed the thankless task of checking the rigorous mathematics of this amateur theoretician and has been an invaluable peer critic. And finally to Sebastian. To my great personal and professional benefit, we have collaborated in scientific matters, traveled, tailgated, and challenged each other's minds through discourse of politics, history, and philosophy. You have been a scholarly colleague and a most sincere friend, and I will miss you.

I especially wish to thank my advisor Dr. Bill Dennis. Your sincere guidance, patience, and tireless investment in your students has set a standard for me that will be very difficult to live up to. I am deeply grateful for the advice and encouragement you have so often given me, and for many opportunities and projects for which I received you fullest support. I will not forget it.

Finally, I wish to thank my girls. My beautiful wife Elizabeth and lovely little girl, Sarah. Thanks for putting up with all the years of long hours. I love you both with all my heart. All is yours.

Table of Contents

List of Tables

Chapter 1

Introduction

The latter half of the twentieth century witnessed the simultaneous development and proliferation of high-power laser technology and supercomputers [1]. Each of these individual developments has revolutionized science and engineering in its own right. The advent of the commercial laser has allowed physicists to reliably produce electric field strengths comparable to, and even exceeding, those found within the atom [2]. This provided the first opportunity to study in detail the sub-discipline of nonlinear optics, where strong electromagnetic fields can alter a material's electric and magnetic susceptibilities, normally assumed to be independent of any external field [3]. Further advances in pulsed-laser technology have created powerful fields in the infrared, visible, and ultra-violet spectral regions on the order of femtoseconds in temporal duration [1]. Pulses on this time scale are capable of resolving physical events which would otherwise be considered instantaneous [4], for example the motion of nuclei under the influence of the applied field, and have proven to be a very effective tool for the micromachining of optical materials [5].

Simultaneously, as computers became more powerful and cost efficient, scientists found new expedience in modeling the evolution and properties of complex physical systems by numerical simulation [6]. Initially employed to confirm experimental results or theoretical predictions, simulations are now used frequently as a primary tool of scientific investigation, with theory and experiment then providing appropriate confirmation. In many cases, numerical simulation is the only tool a theorist has for making definite predictions when analytic solutions are unavailable or perturbation theory and other approximation techniques

are inadequate [7]. This advantage is especially useful in the modeling of nonlinear systems, where small variations in initial conditions can dramatically alter the final outcome of observable events [7].

The use of computer simulations to study the interaction of high-power laser fields propagating through nonlinear media is nearly as old as the laser itself [6]. These simulations have continuously grown in sophistication as computers have become more powerful. It has recently become possible to simulate the propagation of fully three-dimensional ultrashort laser pulses, digitally constructed according to experimental data, through nonlinear materials where laser-induced damage is occurring [8; 9]. The theoretical and computational modeling of this phenomenon constitute the primary subject matter of this dissertation.

A general introduction to the fields of nonlinear, ultrashort, computational optics, as well as computational plasma dynamincs is presented in Chapter 3. Here it is discussed how, in the field of computational optics, it is often necessary to model material dynamics in addition to laser pulse propagation in order to accurately describe the field-matter interactions. Although computational optics and computational material dynamics exist as fields in their own right, the attempt to better unify these two disciplines is a primary theme of this dissertation. The other primary theme of this dissertation is the attempt to better interface simulations in nonlinear optics and laser-induced damage with experimentally measured results, and Chapter 5 will demonstrate that these two themes are interdependent.

Chapter 3 contains a rigorous theoretical discussion of ultrashort pulse propagation in nonlinear media, commenting on previously established models and proposing additional corrections to a Drude free current-density contribution to ultrashort pulse propagation. The models for a Drude free current density that are currently used in the literature are found to be limiting cases of the more general model free current density (based again on the Drude model) derived in Chapter 3. This corrected model is then analyzed and compared with the models currently used in the literature. Results from simulations of solving an equation for ultrashort pulse propagation, derived in Chapter 3, are then presented to show

how significant differences between the models for the Drude free current density might arise in experiment. The pulse propagation equation derived in Chapter 3 will also be used to model ultrashort pulse evolution in the subsequent two chapters.

In Chapter 4, the results of simulations that examine the role of laser beam geometry and laser pulse shape in the formation of a free-electron plasma by laser-pulse driven ionization are presented. The understanding of such processes is extremely important because they initiate laser-induced damage and permanent optical modification to dielectric materials [5]. The first ionization events in such a process occur in the form of photoionization, which in transparent materials is a process with a strongly nonlinear dependence on the electric field [10]. Results of simulations presented in Chapter 4 reveal that beam asymmetries, such as those found in a laboratory laser pulse, can significantly change the number of ionization events that occur as a function of spatial coordinates of the material, when compared to an otherwise identical situation where the beam is perfectly symmetrical. In order to model ultrashort laser pulses with an asymmetric beam structure, an experimentally measured beam profile (energy per unit area normal to the propagation axis) was used to numerically construct the beam geometry of the pulses used in the simulations. These simulations were compared directly with simulations which assumed a beam structure given by a cylindrically symmetric Gaussian function of the same beam width, a very common assumption in the field of computational optics [3]. This finding demonstrates the major role that beam asymmetries have in producing the spatial structure of the electron plasma and hence permanent modifications to the material. It thus has direct implications for the use of ultrashort laser pulses in the efforts to effect changes to transparent materials on the micrometer length scale.

Chapter 5 describes an experiment where the models of ultrafast plasma generation currently employed for simulations in computational optics are found to be inadequate. There the pulse propagation equation derived in Chapter 3 is solved simultaneously with a system of coupled rate equations describing the dynamics of the free-electron plasma generated by

ionization for a variety of pulses. The laser pulses in these simulations were numerically constructed both from experimentally measured beam profiles and experimentally measured pulse (temporal) shape information. To the author's knowledge, these simulations were the first of their kind in two specific ways: first, the initial laser pulses were characterized both spatially and temporally with experimental data. Most simulations in computational optics assume analytic forms for both the beam geometry and the pulse shape. Second, it successfully interfaced the multi-rate equation model for plasma dynamics [11] with the pulse propagation equation derived in Chapter 3. The multi-rate equation model was developed by Rethfeld [11] in 2004 to provide a more detailed description of field-electron interactions in the conduction band than that of the single-rate equation model developed by Stuart [12] (which are used in Chs. 3 and 4). Results of these simulations are directly compared with experimental data, and several notable predictions of the simulations are confirmed, which would not have been possible with the assumption of cylindrical beam symmetry. However, there also exists some irreconcilable discrepancies between the results of simulation and experiment, for which a lack of details in the material model is likely responsible. Possible solutions for this problem are discussed and the implications of interfacing more complex material models with the computational optics simulations in this dissertation are examined.

Chapter 6 concludes with a summary of the work contained in this dissertation, as well as observations of necessary steps in the future of this research. Possibilities for new computational applications of this dissertation and its potential for future research are also discussed.

Chapter 2

Simulations in Ultrashort Nonlinear Optics

High-power lasers have become an important tool for investigating the characteristics of all forms of matter [1]. As high-power lasers improve, it is increasingly necessary to understand and predict the effects of high-intensity pulse-material interactions [10]. This chapter provides a necessary yet brief introduction to the relevant disciplines of nonlinear, ultrafast, and computational optics.

Modern commercial lasers produce pulses that, when focused, can easily yield intensities in excess of 10^{12} watts per square centimeter [2]. At these intensities the familiar laws of optics, known as linear optics, break down, and the interaction of light with matter becomes strongly nonlinear and sometimes destructive [3]. The laser pulses produced to achieve these intensities have temporal durations, or pulsewidths, on the time scale of femtoseconds. Such pulses are commonly referred to as ultrashort pulses, a term more generally used to describe any pulse shorter than 0.5 picoseconds [7]. The corresponding field-material interactions that occur on the time scale of femtoseconds are generally referred to as ultrafast processes, although it is not unusual in the literature to find the terms ultrashort and ultrafast used interchangably without regard to pulse or material reference [13]. Exposure of materials to high-intensity laser fields over such short periods of time has allowed for clean, precise modifications of these materials on the micrometer and nanometer length scales [8; 9; 14–19]. Simulations of these processes can provide valuable insight into experimental results and also help predict the onset of laser-induced damage to optical materials [8; 9; 14].

2.1 Nonlinear Optics

The field of nonlinear optics can be characterized with reference to a material polarization $\vec{P}$ (dipole moment per unit volume, not to be confused with the directional polarization of the electric field), which can be expanded in powers of the electric field $\vec{E}$ [3]:

$$\begin{aligned} \vec{P}(\omega) &= \chi^{(1)}(\omega)\cdot\vec{E}(\omega) + \chi^{(2)}(\omega_1,\omega_2) : \vec{E}(\omega_1)\vec{E}(\omega_2) + \\ &\quad \chi^{(3)}(\omega_1,\omega_2,\omega_3)\vdots\vec{E}(\omega_1)\vec{E}(\omega_2)\vec{E}(\omega_3) + \ldots, \end{aligned} \tag{2.1}$$

where $\vec{E}(\omega_i)$ is the Fourier component of the electric field with angular frequency ω_i and the respective $\chi^{(n)}$'s are electric susceptibility tensors of rank $n+1$ (see Appendix B for a discussion on the generality of this expression). Each individual term in Eq. (2.1) is subject to the condition $\omega = \sum \omega_i$, *i.e.* $\omega = \pm\omega_1 \pm \omega_2$ for the second term on the right-hand side, $\omega = \pm\omega_1 \pm \omega_2 \pm \omega_3$ for the third term, *etc.* Here, the plus/minus signs on each frequency value indicate the possibility of both forward and backward propagating field components; although whether the "plus" represents a forward or backward propagating wave depends on the convention one uses to define the electric field [3]. The first term on the right-hand side of Eq. (2.1) describes all of the behavior of linear optics, as the polarization is linear in the electric field. All remaining terms on the right-hand side represent nonlinear optical responses; *i.e.* for which the polarization depends nonlinearly on the applied field. In any circumstance where the nonlinear terms of Eq. (2.1) are required to provide an adequate description of field-matter interactions, the medium involved is referred to as a nonlinear material [3].

It is evident from Eq. (2.1) that the significance of the nonlinear terms increases as the field strength increases. This condition implies that for sufficiently high intensities, all matter eventually becomes nonlinear, even air [20]. However, because of the frequency summation condition, the nonlinear polarization terms are allowed to resonate at frequencies different from those of the applied field components. For example, if the applied field components in the second-order term of Eq. (2.1) each have a frequency of ω_1, then the polarization field

will resonate at a frequency of $2\omega_1$, leading to the process of second harmonic generation [3]. This is a special case of the more general process of sum (or difference) frequency generation, which can occur with an arbitrary combination of frequencies on any nonlinear polarization contribution [1].

Several additional consequences of the nonlinear interactions in Eq. (2.1) warrant special consideration. First, in isotropic materials all of the even-ordered $\chi^{(n)}$ tensors vanish as required by inversion symmetry [1]. The principle concern of this dissertation is the interaction of high-intensity laser pulses in isotropic materials, and therefore the third-order nonlinear term in Eq. (2.1) will be taken as the primary contribution to the nonlinear polarization, as the higher-order terms usually represent perturbations many orders of magnitude weaker than those of the third order [21]. Second, if inversion symmetry is present, then many components of the $\chi^{(n)}$ tensors also vanish, further simplifying both the linear and nonlinear optical responses. Third, the third-order term of Eq. (2.1) is responsible for the phenomenon of self-focusing, more generally referred to as the Kerr effect [3]. This behavior arises when an approximately monochromatic field interacts with its own backwards-propagating frequency component to produce an intensity dependent polarization [1]. For an electric field linearly polarized in the $\hat{x}$ direction, the forward propagating component of this contribution is given by [22]:

$$\begin{aligned} \vec{P}_{NL}(\omega) &= \chi^{(3)}(\omega,-\omega,\omega) \vdots \vec{E}(\omega)\vec{E}(-\omega)\vec{E}(\omega) \\ \vec{P}_{NL}(\omega) &= \chi^{(3)}_{xxxx}(\omega,-\omega,\omega)\frac{3}{8}\left|\vec{E}\right|^2 \vec{E}(\omega) \end{aligned} \tag{2.2}$$

where $\vec{E}(-\omega) = \vec{E}^*(\omega)$ because $\vec{E}(t)$ must be a real function, and $\chi^{(3)}_{xxxx}$ is the (1,1,1,1) matrix element of the $\chi^{(3)}$ tensor. The factor of 3 in Eq. (2.2) is a degeneracy factor arising from the three possible permutations of the frequency components, while the factor of 1/8 arises due to the ansatz $\vec{E}(t) = (1/2)\vec{E}\exp(-i\omega t)$ + c.c. (where c.c. denotes the complex conjugate of the preceding quantity), which distinctly expresses the field in terms of forward (the first term) and backward (the second term) propagating components. From this form one can use the definition of the electric displacement vector, $\vec{D}(\omega)$, to derive an effective

electric permittivity including both linear and nonlinear effects [1; 23]:

$$\vec{D}(\omega) = \epsilon_0 \vec{E}(\omega) + \vec{P}(\omega) = \epsilon_0 \epsilon_r(\omega) \vec{E}(\omega) \tag{2.3}$$

$$\epsilon_r = 1 + \chi^{(1)} + \frac{3}{8} \chi^{(3)}_{xxxx} \left| \vec{E} \right|^2 \tag{2.4}$$

Equation (2.4) can then be used to define an effective index of refraction $n = \sqrt{\epsilon_r}$ expressed in terms of the linear index of refraction $n_0 = \sqrt{1 + \chi^{(1)}}$, the field intensity $I = (1/2) n_0 \epsilon_0 c \left| E \right|^2$, and the nonlinear index of refraction $n_2 = 3\chi^{(3)}_{xxxx}/(4 n_0 \epsilon_0 c)$ [1]:

$$n_{\text{eff}} = n_0 + n_2 I \tag{2.5}$$

Equation (2.5) is obtained through a binomial expansion of Eq. (2.4), treating the nonlinear contribution as a perturbation and truncating after the second-order expansion term. Equation (2.5) explains the self-focusing phenomenon as a function of optical intensity. For $n_2 > 0$, high-intensity light at the center of a laser beam will travel more slowly than the less intense light on the wings of the beam, curving the wavefront as though it were propagating through a lens [24]. If the beam exceeds a critical power, $P_{\text{cr}} = (1.22\pi/2)^2 \lambda^2/(8\pi n_0 n_2)$, where λ is the optical wavelength, then the Kerr effect overcomes spatial diffraction and, if the pulse continues to propagate through the material, can initiate a process of catastrophic focusing (beam collapse) eventually halted by ionization events and plasma effects [5]. In addition to self-focusing, Eq. (2.5) also predicts the phenomenon of self-phase modulation, by which the shape of the temporal phase accumulated by the pulse, $\phi(t) \propto n_2 I(t)$ [3], depends on the pulse shape as given by the optical intensity $I(t)$. For ultrashort pulses, whose temporal pulse shapes are very steep, this results in a time-dependent shift of the instantaneous frequency, $\Delta\omega(t) = -\partial_t \phi(t)$, whereby a pulse will be red-shifted on the leading edge and blue-shifted on the trailing edge for positive values of n_2 [1].

The optical intensities required to produce specific nonlinear optical effects in matter are shown in Fig. (2.1) [25; 26]. These intensities may be divided into several regimes characterized by different nonlinear optical processes and are distinguished in the figure by vertical

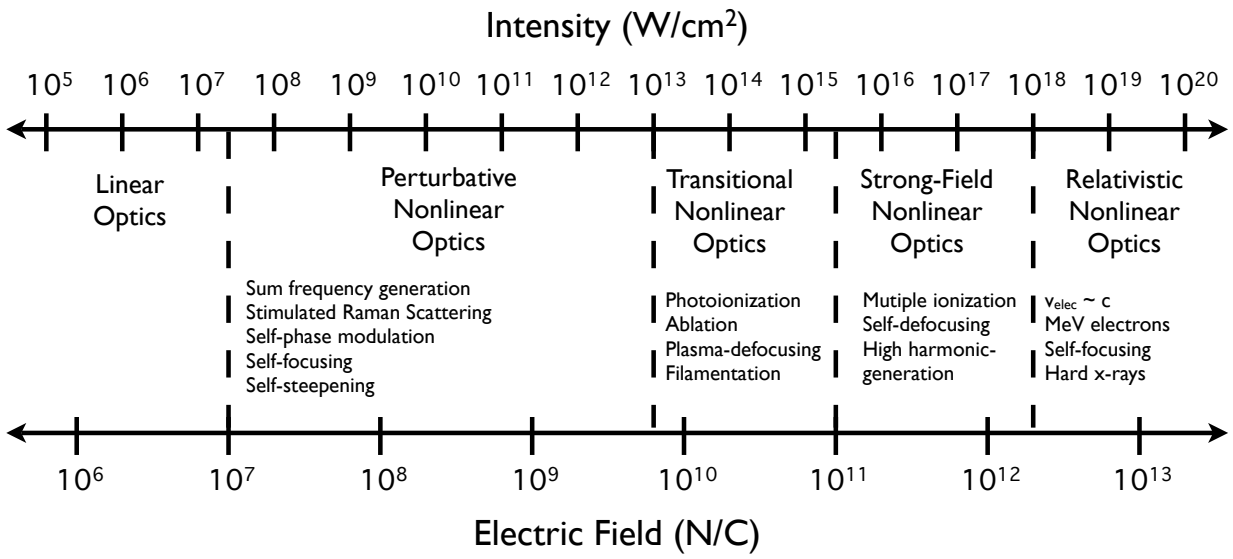

Figure 2.1: The regimes of nonlinear optics.

dashed lines. However, it must be emphasized that such distinctions are only approximate and may vary for different materials [26]. The perturbative regime in Fig. (2.1) is so named because the peak electric fields in this range are orders of magnitude smaller than the electric fields found within the atom [26]. Therefore the laser fields in this regime only perturb the quantum states of the atom (assuming nonresonant excitation conditions), and nonlinear interactions are safely modeled as perturbations to the linear polarization in Eq. (2.1) [26]. For the strong-field and relativistic regimes of Fig. (2.1), the electric field strengths are sufficiently strong to ionize all matter in the immediate vicinity, and optical effects are dominated by the response of free charges and plasmas [26]. In such cases Eq. (2.1) is no longer a complete description of the optical response, since the material polarization, by definition, describes the optical response of bound charges only [23]. Here, one must instead employ an approach that accounts for the presence of a free current density [27]. The transitional regime in Fig. (2.1) comprises the range of intensities where one must account for both the

perturbative nonlinear effects described in Eq. (2.1), as well as the presence and formation of free current densities by ionization [27].

This dissertation is primarily concerned with the perturbative and transitional regimes of Fig. (2.1), more specifically in the intensity range of 10^{12} - 10^{14} W cm^{-2}. At these intensities, perturbative nonlinear effects, such as self-focusing, compete with transitional processes, such as photoionization and plasma defocusing, for control of the spatio-temporal evolution of the laser pulse [19]. Many of the simulations in this dissertation examine the evolution of laser pulses with intensities initially in the perturbative regime that are driven into the transitional regime through the process of self-focusing. A detailed discussion of such phenomena, however, requires some understanding of the ultrashort pulses used to obtain these intensities, and this is the subject of the following section.

2.2 Ultrashort Laser Pulses

To obtain optical intensities sufficient to cause self-focusing and ionization in condensed matter, a laser pulse (in addition to being spatially focused) is often compressed in time to durations on the order of femtoseconds, *i.e.* an ultrashort pulse [1]. Ultrashort pulses can resolve physical events that occur on the same femtosecond time scale (ultrafast processes), since any event must be measured with something of equal size or smaller [13]. Ultrashort pulses also have the advantage of being shorter than the time scale of most phonon interactions (such as lattice heating) [26], and thus materials may be exposed to higher intensity levels without resulting in permanent optical damage [14]. Ultrashort laser pulses also introduce new complications, because processes assumed to be instantaneous for longer pulses (such as nuclear motion under the influence of the laser field [28]) often occur on the time scale of the pulse itself, and therefore require the specification of an explicit time-dependent response for ultrafast processes [29].

The temporal duration of a laser pulse is measured by the full width at half maximum (FWHM) of the intensity and is referred to simply as the pulsewidth [30]. The analogous

spectral width of a pulse is the FWHM of the magnitude squared of the Fourier transform of the electric field into the frequency domain. The relationship between the temporal and spectral widths of a compressed pulse comes in the form of a classical uncertainty relation: $\Delta\omega_{\mathrm{FWHM}}\,\Delta t_{\mathrm{FWHM}} \sim 1$. Specifically, for a Fourier-resolved Gaussian pulse $\Delta\omega_{\mathrm{FWHM}}\,\Delta t_{\mathrm{FWHM}} = 2\,\ln(2)$, where $\Delta\omega_{\mathrm{FWHM}}$ and Δt_{FWHM} are the spectral and temporal widths, respectively [30]. This relation implies that comparatively large spectral widths are required to create pulses of short temporal widths. The spectral width required to create an ultrashort pulse can become comparable (within 20 percent) to the value of the carrier frequency itself and results in unique dispersive properties in addition to traditional group velocity dispersion.

Ultrashort pulses with temporal widths that approach the duration of a single optical cycle of the typical laser field (0.5 fs for the near UV, 1.5 fs for visible light, and 3 fs for the near infrared) present additional challenges. To properly describe any laser pulse, a unique and unambiguous definition of the electric field is required. The real electric field of a 1D ultrashort pulse is commonly described in a complex envelope notation [31]:

$$E(z,t) = \frac{1}{2}\left(\xi(z,t)\; e^{i(k_0 z-\omega_0 t)}\; e^{i\phi_0} + \text{c.c.}\right) \tag{2.6}$$

where $\xi(t)$ is the complex electric field envelope, ω_0 is the carrier frequency of the field, and ϕ_0 is a constant phase offset that determines the relative position of the sinusoidal modulations within the field envelope. Note that the complex field envelope can be expressed as $\xi(t) = |\xi(t)|\, e^{i\phi(t)}$ where $\phi(t)$ is the temporal phase of the field envelope. In addition to the specified pulse shape information contained in $|\xi(t)|$ (commonly assumed to be a Gaussian or hyperbolic secant fucntion), Eq. (2.6) requires *a priori* knowledge of three separate phase terms to uniquely describe a propagating wave; the rapidly varying phase of $(-\omega_0 t)$, the temporal envelope phase $\phi(t)$, and the constant phase offset ϕ_0.

Any envelope description of a laser pulse must begin with a meaningful definition of the carrier frequency ω_0 [31]. This parameter is often assumed to be the frequency value at

the peak of a pulse's spectrum, but a more general definition is provided by the spectrally-weighted average of the frequency [26]

$$\omega_0 = \frac{\int_0^\infty \omega \left|\tilde{E}(\omega)\right|^2 d\omega}{\int_0^\infty \left|\tilde{E}(\omega)\right|^2 d\omega}, \tag{2.7}$$

where $\tilde{E}(\omega)$ is the Fourier transform of the real function $E(t)$ as defined in Appendix A. The primary requirement, however, for using Eq. (2.6) as a mathematical description of an ultrashort pulse is that ω_0 must be invariant under any change in the phase offset ϕ_0 [26]. Brabec and Krauze [26] have shown that the carrier frequency as defined in Eq. (2.7) fulfills this requirement for laser pulses with temporal widths as short as one optical cycle.

The uniqueness of the electric field is another matter. Figure (2.2) shows how a $\pi/2$ shift in the frequency offset ϕ_0 alters the electric field of an ultrashort pulse where the field envelope $\xi(t)$ is described by a Gaussian function (black, solid line) with a flat envelope phase ($\phi(t) = 0$) and a pulsewidth of 3.5 fs. Differences of this kind can potentially affect the evolution of a laser pulse as it propagates through a material [31; 32], particularly in situations where the optical response is nonlinear with respect to the instantaneous electric field, such as tunneling and above-threshold ionization [26]. Whereas there are proven methods to experimentally retrieve both the time dependent amplitude and phase of the field envelope $\xi(t)$ (see for example Trebino's Frequency-Resolved Optical Gating method [13]), the true value for the phase offset ϕ_0 is rarely known with any certainty. In fact, methods for accurately determining this parameter, or rather for the stabilization of it, constitute a current topic of research because of their potential significance for optical frequency metrology and optical clocks [33]. However, since the phase offset is generally not recoverable at the current time, one is restricted to using a description of pulse propagation which is also invariant under changes in ϕ_0. A brief outline of such descriptions and the methods used to model the evolution of the electric field propagating through nonlinear media is presented in the next section.

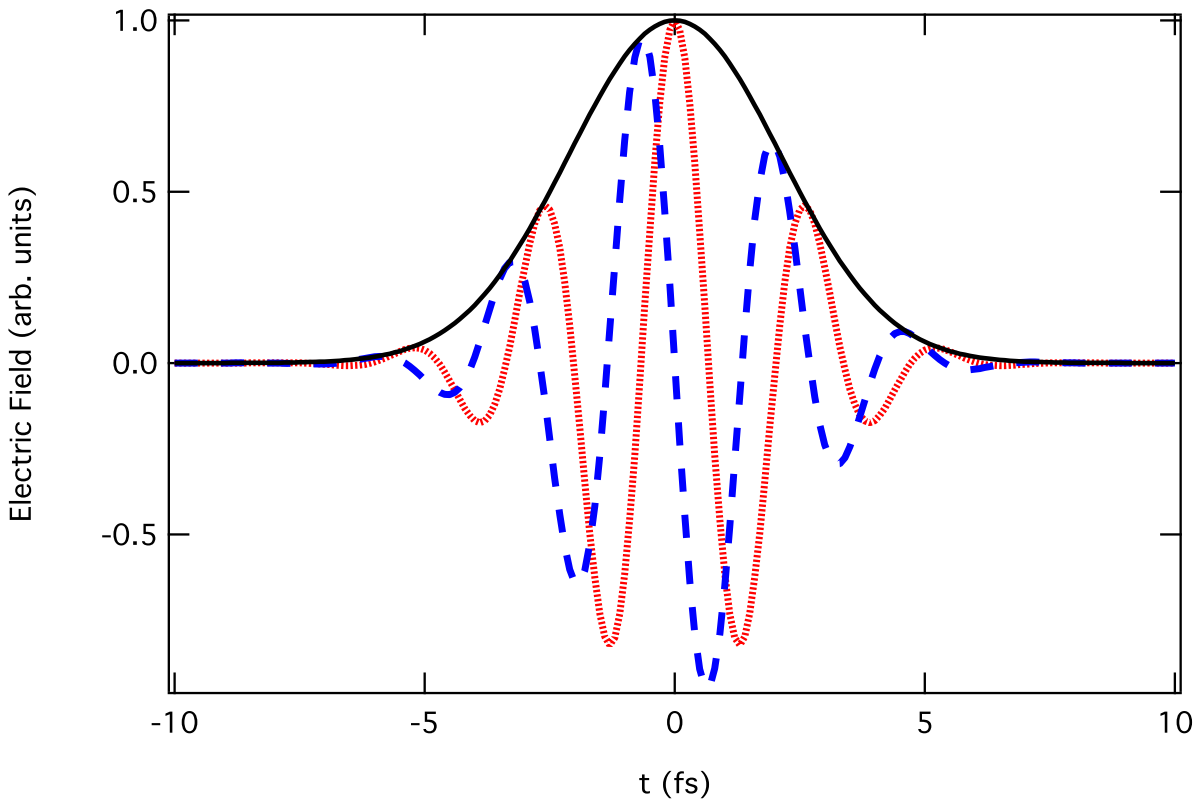

Figure 2.2: Two normalized electric fields for a 3.5 fs laser pulse with peak wavelength of 800 nm, both represented by the same Gaussian field envelope (shown in black). The rapidly varying electric field with zero phase offset ($\phi_0 = 0$) is shown by the dotted red line, and a rapidly varying electric field with a phase offset $\phi_0 = \pi/2$ is shown by the dashed blue line.

2.3 Computational Nonlinear Optics and Ultrafast Material Dynamics

The most common goal of a computational optics project is to obtain numerical values for propagating electric and magnetic fields throughout a specified region of space and time [34]. However, it is often desirable (and sometimes necessary) to include calculations of material dynamics as a secondary yet simultaneous consideration, in order to model field-matter interactions [3]. Equally, there is a rich field of research primarily dedicated to calculating the complicated material response to ultrashort pulses while treating the ultrashort pulse propagation as a secondary yet simultaneous consideration [12; 35–45]. In each case the terms "primary" and "secondary" indicate which concern (optics or material dynamics) is modeled with greater precision and complexity (the primary concern) and which concern is modeled by a comparatively simple approach (the secondary concern). This section briefly outlines both of these fields, their methods and their applications, as well as the contributions of this dissertation to each.

2.3.1 Simulations of Ultrashort Pulse Propagation in Nonlinear Media

When performing a simulation of ultrashort pulse propagation through a nonlinear medium, one often seeks to recover the electromagnetic field at the end of the propagation for spectrographic analysis, as this is the data most easily accessible in the laboratory and is thus appropriate for comparison. However, simulations have the added advantage that one can directly monitor the pulse evolution at any point during the propagation, providing physical insight generally unavailable from experiment. Many methods exist for numerically calculating the evolution of an ultrashort pulse through a nonlinear material, all of which rely on some initially assigned form for the electric and magnetic fields provided by the user [7; 24; 26; 31; 46–49]. These methods include finite-difference time domain schemes [34], beam propagation methods [3], spectral techniques [6], frequency domain finite element methods [7], variance matrix methods [7], and ABCD matrix methods [48].

The most general of these methods is to solve the Maxwell equations directly by a finite difference time domain (FDTD) scheme [6]. In principal, the FDTD scheme requires no assumptions about the field other than its initial numerical form. It monitors all vector components of the real electric and magnetic fields at all points in space and time, and thus allows for arbitrary polarization of these fields. It accounts for both forward and backward propagating waves, multiple materials and interfaces (including dielectric stacks or filters [50]), as well as field reflection and transmission at these interfaces. The disadvantage of the FDTD approach is that the simulations can be computationally prohibitive to perform because they must sample a minimum of two points per field oscillation to avoid violating the Nyquist limit [34]. Because of this, FDTD simulations are often restricted to 1+1D pulse simulations (one dimension in space and one in time) for all but the shortest of pulses and propagation lengths. Therefore, if one wishes to efficiently model 3D spatial dynamics (*i.e.* not only the temporal evolution but also the beam evolution) of a laser pulse over propagation distances much greater than the pulse length, then a simplified approach is typically required in practice. However, as computational power increases FDTD simulations will likely be used for correspondingly more detailed calculations [7].

An alternative approach to numerically solving the Maxwell equations directly is to solve a propagation equation for the electric and/or magnetic fields [25]. In this approach one usually assumes that all bulk materials are non-magnetic and electrically neutral at all times. A derivation of the wave equation for a propagating electric field from the macroscopic Maxwell equations using these assumptions is given in Appendix C. A wave propagation equation has the advantage of being conceptually simpler than Maxwell's equations, but has the considerable disadvantage of being a second-order partial differential equation in space and time. Therefore, a wave equation approach still requires significant computational resources to model any situation other than monochromatic light propagation through isotropic linear media, which can often be solved more simply using analytical techniques. With some additional assumptions, however, one can use the wave equation to obtain a simplified first-order

partial differential equation for the electric field envelope evolving along the propagation axis [24] and which maintains its validity for pulses as short as a single optical cycle [31]. This will be referred to as an envelope equation approach and is used as the primary theoretical method of modeling of ultrashort pulse propagation in this dissertation. The derivation of the general envelope equation used throughout this dissertation is given in Chapter 3. Solving the first-order partial differential envelope equation is far less demanding in terms of computational resources than either the FDTD or wave equation approaches [25]. Most notably, the envelope equation approach has recently been used for the simulation of fully 3+1D (3 spatial plus 1 time dimension) laser pulses through regions where laser-induced damage is occurring [8].

The additional requirements for the envelope equation to be valid are as follows: the laser field is linearly polarized and the material is isotropic, so that a scalar approach can be taken; the pulsewidth is at least one optical cycle in temporal duration; and neither the electric field amplitude nor the temporal phase vary significantly over the propagation distance of one optical wavelength [31]. The latter of these requirements is formally know as the slowly varying wave approximation (SVWA) [31]. Envelope equations describe the evolution of the complex electric field envelope, $\xi(\vec{x},t)$ as defined in Eq. (2.6), as it travels along the propagation axis, z, at the group velocity, v_g, of the laser pulse [3]. The most common form of envelope equation is the nonlinear Schrödinger equation (NLSE) [1], also referred to as the beam propagation equation:

$$\frac{\partial \xi}{\partial z} = \frac{i}{2k_0}\left(\frac{\partial^2}{\partial x^2} + \frac{\partial^2}{\partial y^2} - \frac{k_0}{v_g}\frac{\partial^2}{\partial \tau^2}\right)\xi + i\gamma\left|\xi\right|^2\xi, \tag{2.8}$$

where k_0 is the wave vector evaluated at the carrier frequency ω_0, and $\tau = t - z/v_g$ is the retarded time frame of the laser pulse. Here the first-order derivative in z describes the evolution along the propagation axis, the second-order derivatives in x and y describe the beam evolution (diffraction), the second-order τ derivative describes group velocity dispersion in the retarded time frame, the constant $\gamma = k_0\epsilon_0 c n_2/2$, and the nonlinear term in ξ describes the Kerr effect contribution to the field evolution, which results in self-phase modulation

and self-focusing for positive values of the nonlinear refractive index, n_2. The NLSE is so named because, in the absence of the nonlinear contribution, it has the mathematical form of Schrödinger's famous equation from quantum mechanics, but it should be emphasized that Eq. (2.8) is a classical equation.

The NLSE, and the numerous variations of it, have been used for over three decades to describe the propagation of beams and pulses through a wide variety of nonlinear media [4; 24; 51]. Variations of the NLSE are often referred to as modified NLSE's and are ubiquitous in the literature [8; 14; 19; 29; 31; 32; 52–54]. In Chapter 3 of this dissertation it is shown that one such modification to the NLSE, describing temporal dispersion effects of free-carrier plasmas on ultrashort pulse propagation, is widely inconsistent in the literature. In Chapter 3 it is also demonstrated that all of these inconsistent variants of the free-carrier modification are actually limiting cases of a more general modification. The consequences of this more general modification are then examined both analytically and with simulations to determine when and where differences between the variant models become important. These simulations model fully 3+1D field propagations, solving the envelope equation to demonstrate numerically how this modification would manifest itself experimentally. In Chapter 4 the modified NLSE is solved for a fully 3+1D laser pulse with beam and temporal asymmetries (digitally constructed from experimental data) to examine, for the first time, how these properties can affect the ultrafast generation of free-carrier plasmas in a dielectric material.

2.3.2 Simulations of Ultrafast Plasma Generation

Simulating the interaction of ultrashort laser pulses with matter often requires the modeling of ultrafast free-carrier dynamics in addition to modeling the pulse evolution. Such interactions are usually modeled by one of two methods: 1) a set of classical, coupled rate equations (often a single-rate equation) describing populations of relevant quantities [1; 11; 12; 55], or 2) a combination of partial differential equations (PDEs) describing the distribution of charge carriers and/or phonons in phase space or energy space [35–42]. Researchers engaged

in computational optics (for whom the pulse evolution is primary and material dynamics are secondary) tend to favor the former method, as it is conceptually simpler and easier to implement [11]. By contrast, materials researchers often choose the PDE approach while treating the pulse evolution with a reduced model [56] or an analytical expression [40].

This dissertation uses a combination of the rate equation and PDE approaches. Each chapter uses a different model of the material dynamics, depending on the goal of the simulations, and explains the details of each model in turn. Therefore, only a qualitative introduction to the various models of the material dynamics will be given in this chapter. However, the successive chapters are organized to reflect the growing complexity of the material model used. Chapter 3 is primarily concerned with the macroscopically-averaged effect of free-carrier dynamics on the field propagation, and models free-carrier plasma generation with a single-rate equation describing the promotion of valence electrons to the conduction band by the nonlinear process of photoionization. In Chapter 4 the effects of plasma generation and laser-induced damage in fused silica are simulated as a function of asymmetries in beam and pulse structure. Plasma dynamics in Chapter 4 are again modeled with a single-rate equation, but with the addition of an impact-ionization term and an electron-hole recombination contribution. Chapter 5 interfaces the modified NLSE model for a fully 3+1D ultrashort pulse propagation with a multi-rate equation model for the free-carrier dynamics in a nonlinear medium. This combination, to the author's knowledge, has never before been treated in the literature. Also discussed in Chapter 5 is the possibility, and perhaps the necessity, of instead interfacing PDE models of carrier dynamics with the modified NLSE.

Classical rate equation models of material dynamics are based on macroscopically averaged field-carrier-material interactions [12]. They often consist of a single-rate equation describing the instantaneous generation of a free-carrier plasma, including contributions from photoionization and impact ionization, as well as the possibility of radiative recombination into the valence band (but usually excluding capture by traps and impurities) [11; 14; 19]. This single-rate equation approach was derived in detail by Stuart *et. al.*, [12] from the

Fokker-Planck PDE under the assumption of a constant distribution of electrons in energy space. More recently, Rethfeld developed a multi-rate equation model [11] as an extension of Stuart's single-rate equation model, to account for the fact that free electrons must absorb energy in integer increments of the laser photon energy before accumulating sufficient energy for impact ionization. The Rethfeld model therefore describes the temporal evolution of multiple populations of free electrons on a ladder of levels in energy, evenly spaced by the photon energy. All of the classical rate equation models consist of ordinary differential equations, which are solvable with standard numerical integrators.

The PDEs most commonly used in the literature to describe carrier dynamics in semiconductors and wide bandgap materials are the Boltzmann equation and the Fokker-Planck equation [36; 40], although other related energy and force-balance equations are also used [37–39]. The solution of the Boltzmann equation yields the distribution of carriers in phase space [35] while the solution of the Fokker-Planck equation yields the number carrier density per unit energy in energy space [36]. While the rate equation approach has been widely used in the last twenty years (mostly for the purpose of computational optics rather than materials science), PDEs have been used in the field of material science for well over fifty years [36; 57; 58]. Of the two PDEs, the Fokker-Planck equation is the easier to implement, because it models all carrier-field-material interactions phenomenologically and can be expressed as a continuity equation in energy space [36]. As a continuity equation, it is solvable with standard finite-difference methods [59]. In contrast, the Boltzmann equation is an integro-PDE that requires the evaluation of quantum-mechanical collision integrals and must be solved stochastically, usually with a Monte Carlo method [35]. The Boltzmann equation requires the maintenance of a six dimensions representing the electron distribution in phase space, as opposed to the four-dimensional space of the Fokker-Planck equation. The Boltzmann equation approach also requires the user to solve not just one such equation for the free electrons, but additional Boltzmann equations for the holes and for every phonon mode (both optical and acoustic) that makes a significant contribution to the material dynamics [40].

It is therefore a more cumbersome, but also a more complete and generally more accurate, model than the Fokker-Planck description.

To date, all efforts in computational optics to simulate the propagation of fully 3+1D laser pulses have used the single-rate equation approach. Some 3+1D and 2+1D (pulses with cylindrical beam symmetry) simulations have used the classical multi-rate equation model [55; 60]. To the author's knowledge, no computational optics project has ever attempted to perform a fully 3+1D pulse propagation simulation with field-material interactions modeled by the multi-rate equation approach or either of the PDE approaches. Further, no attempt has been reported in the literature to have included such ultrashort pulse effects as self-frequency shifting in any of the current models of plasma dynamics, whether rate equation or PDE. An attempt to do this is essentially an attempt to better unify the concerns of computational nonlinear optics and computational material dynamics. The theoretical implications as well as the computational challenges of this effort are examined in Chapter 5.

2.3.3 Simulations in This Dissertation

The simulations in this dissertation, with the exception of those in Chapter 5, are performed within the framework of computational optics, with the pulse evolution receiving primary consideration and plasma generation secondary consideration, from a purely computational perspective. In these cases the pulse evolution along the propagation axis is obtained by solving a modified NLSE using a split-step algorithm (see Fig. (2.3)) with all terms linear in the field envelope constituting a linear step and all other terms constituting a nonlinear step [25]. The linear step is solved using a Fast Fourier Transform, Crack-Nicholson, or implicit finite differencing technique, while the nonlinear step is solved using fourth-order and adaptive step-size Runge-Kutta methods. The material dynamics of these simulations are contained in the calculation of plasma generation, *i.e.* the promotion of electrons from the valence band to the conduction band, which is modeled by a single classical rate equation

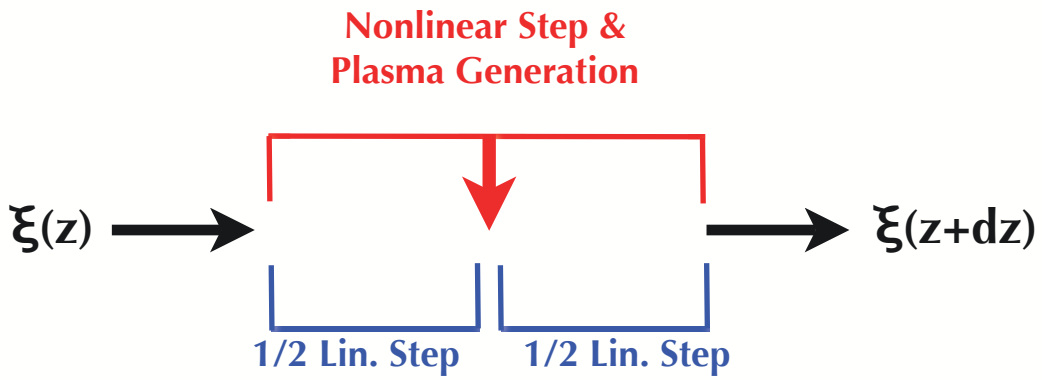

Figure 2.3: Schematic of the split-step method used to solve the equation for the electric field envelope $\xi(z)$ as it evolves along the propagation axis z. The nonlinear step is taken in the middle of the linear step to achieve an extra order of accuracy.

and solved with an adaptive step-size Runge-Kutta method during the nonlinear step of the pulse propagation.

At the end of Chapter 5, simulations of plasma dynamics are performed as the primary computational consideration. These simulations were performed by solving a Fokker-Planck equation and the Rethfeld multi-rate equation for the distribution of free carriers in the conduction band energy space. These simulations used 1+1D electric fields (constructed from experimental data) that propagate through extremely thin slices of material over which pulse evolution is negligible (a common approach in the study of the non-equilibrium statistical mechanics of semiconductors and dielectrics [35]). These results are compared to those predicted by the simpler classical rate equation models commonly used in computational optics. In Chapter 5, the need for a modified Fokker-Planck equation is addressed. This Fokker-Planck equation would be designed to account for instantaneous frequency shifts and other temporal correction effects predicted by the modified NLSE; which to date no

model of plasma dynamics, either rate equation or PDE, has attempted to include. Finally, the challenges of performing fully 3+1D pulse propagation simulations with the modified Fokker-Planck equation are discussed and preliminary results are presented.

Chapter 3

Free-carrier effects of the Modified Nonlinear Schrödinger Equation

The past decade has seen frequent use of a modified nonlinear Schrödinger equation to describe ultrashort pulse propagation in materials where free-carrier plasmas are present. The optical contribution from the resulting free current densities in this equation is often described using a classical Drude model. However, the ultimate form of this contribution in the modified nonlinear Schrödinger equation is somewhat inconsistent in the literature. This ambiguity is clarified in this chapter by deriving the modified nonlinear Schrödinger equation from the classical wave equation containing a free current-density contribution. The Drude model is then used to obtain an expression for the complex free-carrier current-density envelope with temporal dispersion corrections for ultrashort laser pulses. These temporal dispersion corrections to the current-density term differ from all other models in the literature in that they depend more sensitively on the value of the Drude free-carrier collision time. These corrections reduce to the current models in the literature for limiting cases. Theoretical analysis and computer simulations show that these differences can significantly affect the dynamic interactions of plasma absorption and plasma defocusing for materials with free-carrier collision times on the order of one optical cycle (or less) of the applied field.

3.1 Introduction

In the past decade there has been significant interest in the precise modification of materials on both the micrometer and nanometer length scales [14; 15; 17; 61–63]. High-intensity, ultrashort laser pulses are now used in micro-machining and nanostructuring applications, because of the ability to make precise, reversible material modifications both on the surface

and in the bulk, often while avoiding the onset of permanent structural damage to the material [64]. Ultrashort laser pulses are also an important tool for discovering fundamental information about optical and material processes that occur on time scales approaching the limit of one optical cycle of the applied laser field [26; 31]. The widespread use of ultrashort pulses for these purposes necessitates the development of a more detailed and fundamental description of free-carrier effects in the femtosecond time regime [65; 66]. Ultimately, this must involve a systematic investigation of the interplay between high-intensity ultrashort pulse propagation and the presence of free-carrier plasmas within the material [5; 11]. For linearly polarized laser pulses, a scalar electric field envelope equation has proven to be an accurate and efficient method for describing ultrashort pulse propagation in a variety of isotropic nonlinear materials [3; 31].

Nonlinear envelope equations have been used to model high-intensity laser pulse propagation for over three decades [4; 24; 25; 67]. A basic nonlinear Schrödinger equation (NLSE) can account for optical diffraction, dispersion, and a Kerr-type nonlinear polarization [1]. As laser pulses became progressively shorter in duration and correspondingly stronger in intensity, researchers found it necessary to account for high-order energetic and temporal effects [3]. The energetic (high-intensity) corrections include high-order nonlinearities, multi-photon absorption, and free-carrier effects [3]. Temporal corrections to the NLSE can be largely attributed to two papers. In the first of these papers, Blow and Wood [29] provide a basic model for temporal delay of the nonlinear response, for the material of fused silica in particular. In the second of these papers, Brabec and Krausz [31] derive a nonlinear envelope equation valid for laser pulses as short as one optical cycle in duration. This modified NLSE accounts for high-order dispersion, linear shock, and self-steepening without actually specifying the form of the nonlinear polarization, allowing for a direct incorporation of the Blow and Wood model for nonlinear delay.

The inclusion of nonlinear delay and high-order energetic corrections to the nonlinear polarization in the modified NLSE of Ref. [31] is straight-forward. However, inclusion of

free-carrier effects is somewhat ambiguous, as a free current-density term was not included in the original wave equation from which the modified NLSE was derived [31]. Contributions of a Drude free-carrier current density to the modified NLSE to date have frequently been of the form [14; 64; 68; 69]:

$$\left[\frac{\partial \xi}{\partial z}\right]_{fc} = -\frac{\sigma}{2}\left(1 + i\omega_0\tau_c\right)\hat{T}^{-1}\left[\rho\,\xi\right] \ , \tag{3.1}$$

where ξ is the complex electric field envelope, z is the propagation axis, $\sigma = q^2\tau_c/n_0 c\epsilon_0 m(1+\omega_0^2\tau_c^2)$ is the cross-section of inverse Bremsstrahlung absorption, $n_0 = k_0 c/\omega_0$ is the linear index of refraction, q is the free-carrier charge, c is the speed of light in a vacuum, τ_c is the free-carrier collision time, ω_0 is the carrier frequency of the field, ρ is the time dependent free-carrier density, and $\hat{T}^{-1}$ is the inverse of a steepening operator $\hat{T} = 1 + (i/\omega_0)\partial_t$ as defined in Ref. [31]. The inverse steepening operator in Eq. (3.1) is sometimes assumed to be unity for longer pulses (*i.e.* $\hat{T}^{-1} \to 1$), a zeroth temporal order approximation common in the literature [19; 52; 70]. In other recent papers the inverse steepening operator is attached only to the imaginary part of Eq. (3.1) [46; 54]. The author has investigated this matter and has found that Eq. (3.1), and the other aforementioned free-carrier contributions, are limiting cases of a more general Drude free-carrier contribution:

$$\left[\frac{\partial \xi}{\partial z}\right]_{fc} = -\frac{\sigma}{2}\left(1 + i\omega_0\tau_c\right)\hat{G}^{-1}\left[\rho\xi\,\right] \ , \tag{3.2}$$

where $\hat{G}^{-1}$ is the inverse of a free-carrier dispersion operator $\hat{G} = 1+(i/\omega_0)g\partial_t$ derived in this chapter. Here $g = -i\omega_0\tau_c/(1 - i\omega_0\tau_c)$ is a dimensionless complex constant that distinguishes the free-carrier operator $\hat{G}$ from the steepening operator $\hat{T}$. The time derivative coefficient of the $\hat{T}$ operator depends only on the carrier frequency ω_0 while the $\hat{G}$ operator additionally depends on the electron collision time τ_c, which is a material parameter from the Drude model. It will also be demonstrated that Eq. (3.1) is an accurate approximation of Eq. (3.2) only in the limiting case where the collision time is much greater than an optical cycle of the applied field.

In this chapter a derivation of a modified NLSE with a Drude free current-density contribution is presented following the method of Ref. [31]. The resulting equation shows that the contribution of free carriers is given by Eq. (3.2), the results of which are in turn compared analytically with the results predicted by Eq. (3.1). Results from simulations that solve the modified NLSE in fused silica below the threshold of permanent optical damage are also presented, and Eqs. (3.1) and (3.2) are compared as descriptions of free-carrier effects.

3.2 Derivation of a modified NLSE with a free current density

A linearly-polarized laser pulse propagating through a nonlinear isotropic medium with free carriers can be described by the following wave equation [31; 46] (See Appendix C for the derivation of this equation):

$$\nabla^2\vec{E} - \frac{1}{c^2}\frac{\partial^2\vec{E}}{\partial t^2} = \mu_0\frac{\partial^2\vec{P}}{\partial t^2} + \mu_0\frac{\partial\vec{J}_F}{\partial t}. \tag{3.3}$$

Here c is the speed of light in a vacuum and $\vec{E}$ is the electric field that satisfies the condition $\vec{\nabla}\cdot\vec{E} = 0$ [46]. On the right-hand side of Eq. (3.3) are the two source terms, where $\vec{P}$ is the total polarization and represents the optical contribution of bound charges, while $\vec{J}_F$ is the free current density and represents the optical contribution of free carriers. Equation (3.3) requires that the propagation medium is nonmagnetic, and that the magnetic field will not contribute significantly to the motion of the charged particles. The nonlinear polarization, $\vec{P}_{NL}$, is considered to be a perturbation to the linear polarization, $\vec{P}_L$, such that $\vec{P} = \vec{P}_L + \vec{P}_{NL}$.

3.2.1 The nonlinear envelope equation

Equation (3.3) is expressed in terms of a linear displacement field $\vec{D}_L = \epsilon_0\vec{E} + \vec{P}_L$. The resulting expression is Fourier transformed into the frequency domain where $\tilde{\vec{D}}_L(\omega) = (c^2/\omega^2)\tilde{\kappa}^2(\omega)\tilde{\vec{E}}(\omega)$ and $\tilde{\kappa}(\omega) = \tilde{k}(\omega) + i\tilde{\alpha}(\omega)/2$ is the complex linear wave vector, $\tilde{k}(\omega)$ is

the real part of the wave vector, and $\tilde{\alpha}(\omega)$ is the intensity based absorption coefficient:

$$\nabla^2 \tilde{\vec{E}} + \tilde{\kappa}^2 \tilde{\vec{E}} = -\mu_0 \omega^2 \tilde{\vec{P}}_{NL} - i\omega\mu_0 \tilde{\vec{J}}_F. \tag{3.4}$$

Next, all vectors are expressed in complex notation and in terms of their respective complex envelope functions:

$$\vec{E}(\vec{x},t) = \frac{1}{2}\left(\xi(\vec{x},t)\; e^{i(k_0 z - \omega_0 t)} + \text{c.c.}\right)\hat{x}\;, \tag{3.5a}$$

$$\vec{P}_{NL}(\vec{x},t) = \frac{1}{2}\left(p_{nl}(\vec{x},t)\; e^{i(k_0 z - \omega_0 t)} + \text{c.c.}\right)\hat{x}\;, \tag{3.5b}$$

$$\vec{J}_F(\vec{x},t) = \frac{1}{2}\left(j_f(\vec{x},t)\; e^{i(k_0 z - \omega_0 t)} + \text{c.c.}\right)\hat{x}\;, \tag{3.5c}$$

where ω_0 is the carrier frequency, k_0 is the real part of the complex wave vector, *i.e.* $\Re[\tilde{\kappa}(\omega_0)]$, and z is the propagation axis. Equations (3.5a - 3.5c) are Fourier transformed to the frequency domain and substituted into Eq. (3.4). The derivatives along the propagation axis are then taken, the backwards propagating elements are neglected, and the scalar product with the $\hat{x}$ direction is taken to yield a scalar expression in terms of the envelope functions.

$$\begin{aligned}\left(\nabla_\perp^2 + \partial_z^2 + 2ik_0\partial_z + \tilde{\kappa}^2(\omega) - k_0^2\right)\tilde{\xi}(\vec{x},\omega-\omega_0) = \\ -\omega^2\mu_0\tilde{p}_{nl}(\vec{x},\omega-\omega_0) - i\omega\mu_0\tilde{j}_f(\vec{x},\omega-\omega_0)\end{aligned} \tag{3.6}$$

The complex wave vector $\kappa(\omega)$ is Taylor expanded about the carrier frequency ω_0, and Eq (3.6) is inverse Fourier transformed back into the time domain. The equation is then further transformed into the retarded time frame traveling at the group velocity $v_g = 1/\partial_\omega k(\omega_0)$ of the pulse; *i.e.* $z' = z$ is the transformed propagation axis and $\tau = t - z/v_g$ is the retarded time coordinate. The equation is now rearranged to read:

$$\begin{aligned}\left(\nabla_\perp^2 + \partial_{z'}^2 + 2ik_0\hat{U}\partial_{z'} + 2k_0\hat{U}\hat{D}_b + \hat{D}_b^2\right)\xi(\vec{x},\tau) = \\ -\mu_0\omega_0^2\hat{T}^2 p_{nl}(\vec{x},\tau) - i\mu_0\omega_0\hat{T}j_f(\vec{x},\tau)\end{aligned} \tag{3.7}$$

where $\hat{D}_b$ is the bound charge linear dispersion operator, and $\hat{U}$ and $\hat{T}$ are steepening operators defined by:

$$\hat{D}_b = i\frac{\alpha_0}{2} - \frac{\alpha_1}{2}\partial_\tau + \sum_{m=2}^{\infty} \frac{k_m + i\alpha_m/2}{m!}(i\partial_\tau)^m \tag{3.8a}$$

$$\hat{U} = 1 + i\frac{k_1}{k_0}\partial_\tau \tag{3.8b}$$

$$\hat{T} = 1 + i\frac{1}{\omega_0}\partial_\tau \tag{3.8c}$$

where $k_m = \partial^m \tilde{k}/\partial\omega^m|_{\omega_0}$ and $\alpha_m = \partial^m \tilde{\alpha}/\partial\omega^m|_{\omega_0}$. The slowly-varying-wave approximation (SVWA) is now applied, *i.e.* $|\partial_{z'} E| \ll k_0|E|$, allowing one to neglect the second-order derivative along the propagation axis [31]. The equation is then rearranged to read:

$$\begin{aligned} \hat{U}\frac{\partial\xi}{\partial z'} &= i\left[\frac{\nabla_\perp^2}{2k_0} + \left(\hat{U} + \frac{\hat{D}_b}{2k_0}\right)\hat{D}_b\right]\xi(\vec{x},\tau) \\ &\quad + i\frac{\omega_0}{2n_0\epsilon_0 c}\hat{T}^2\, p_{nl}(\vec{x},\tau) - \frac{\hat{T}}{2n_0\epsilon_0 c}\, j_f(\vec{x},\tau). \end{aligned} \tag{3.9}$$

In principle, this equation may now be solved for the pulse envelope ξ once p_{nl} and j_f are specified. Eq. (3.9) is in fact the nonlinear envelope equation used by some authors in the literature [64; 68; 71–73]. However, it is common to make additional approximations that simplify this expression. In transparent materials, it is generally the case that $(\hat{D}_b/2k_0)\xi \ll \xi$. Also, the SVWA requires that the condition $|1-\omega_0 k_1/k_0| \ll 1$ be satisfied in order to describe propagation of pulses with temporal durations approaching the limit of one optical cycle [31]. If this criterion is satisfied, then the approximation $\hat{U} \approx \hat{T}$ becomes applicable. In fused silica, for example, $\omega_0 k_1/k_0 \approx 1.0095$ for 800 nm light and the above condition is sufficiently satisfied. Once these approximations are applied, the equation is multiplied by the inverse steepening operator $\hat{T}^{-1}$ and takes the simpler form:

$$\begin{aligned} \frac{\partial\xi}{\partial z'} &= \left(\frac{i}{2k_0}\hat{T}^{-1}\nabla_\perp^2 + i\hat{D}_b\right)\xi(\vec{x},\tau) \\ &\quad + i\frac{\omega_0}{2n_0\epsilon_0 c}\hat{T}\, p_{nl}(\vec{x},\tau) - \frac{j_f(\vec{x},\tau)}{2n_0\epsilon_0 c}. \end{aligned} \tag{3.10}$$

Equation (3.10) is now identical to the nonlinear envelope equation derived in Ref. [31], but in SI units and with the addition of a free current-density term. It is notable that no steepening operators act on the free current density envelope.

This does not mean to imply that there are no temporal corrections necessary to correctly account for ultrashort pulses propagating through a free-carrier plasma, as per the zeroth order approximation of Eq. (3.1). However, if such corrections are necessary, Eq. (3.10) predicts that they must arise from within the free current density envelope itself. Such corrections will depend explicitly on the model one uses to calculate the free current density. Also, if multiple sources of free current densities exist (*e.g.* a free-electron gas or a photoionization current) then j_f represents the sum of all of their individual contributions. As specific examples, envelopes for a Drude-type free current density as well as a photoionzation current will be derived in the following subsections.

3.2.2 The photoionization current density envelope

An important process in high-intensity laser pulse propagation is photoionization, which often produces the first free charges in an otherwise neutral, nonconducting material [5]. In a strongly insulating medium this may require the simultaneous absorption of multiple photons to excite an electron from the valence band to the conduction band. If the instantaneous intensity within the pulse is in excess of $\sim 10^{14}$ W cm^{-2}, then ionization processes can become strongly dependent on the absolute phase of the pulse, thereby invalidating an envelope treatment in this regime [26]. However, at lower intensities a time-averaged photoionization absorption is ubiquitous in the modified NLSEs of the literature. Here there also exists some ambiguity in the form of this contribution; see for example Refs. [14; 52; 68; 74]. Therefore, an expression for the complex envelope of a time-averaged photoionization current density $\vec{J}_{PI}(\vec{x}, t)$ will be derived.

The optical power loss per volume from photoionization is $\vec{J}_{PI} \cdot \vec{E}$. This quantity, when time-averaged, is expressed in complex envelope notation and directly related to the energy

required for valence electrons to cross the forbidden gap U at a number per volume photoionization rate of W_{PI}; $(1/2)\, j_{pi}^{*}\, \xi = W_{PI}\, U$,[23] where j_{pi} is the photoionization current density envelope. In terms of the intensity $I = (1/2) n_0 \epsilon_0 c |\xi|^2$, the resulting current density envelope in the retarded time frame is

$$j_{pi}(\vec{x}, \tau) = n_0 \epsilon_0 c \, \frac{W_{PI} U}{I} \, \xi(\vec{x}, \tau). \tag{3.11}$$

Eq. (3.11), when substituted into Eq. (3.9) or Eq. (3.10), is in agreement with the form of the photoionization contribution to the modified NLSE most commonly used in the literature [8; 19; 46; 54; 64; 68–73].

3.2.3 The Drude free current density envelope

An expression for a plasma fluid contribution to the free current density envelope $j_f(\vec{x}, t)$ will now be derived. A current-density vector for a free-carrier fluid $\vec{J}_{FC}$ in an electrically neutral medium can be described by an equation of force density according to the Drude model [46].

$$\frac{\partial}{\partial t} \vec{J}_{FC}(\vec{x}, t) + \frac{1}{\tau_c} \vec{J}_{FC}(\vec{x}, t) = \frac{q}{m} \vec{F}(\vec{x}, t). \tag{3.12}$$

Here τ_c is the characteristic free-carrier collision time, m and q are the respective mass and charge of the individual free carriers, $\vec{F}(\vec{x}, t) = q\rho(\vec{x}, t)\vec{E}(\vec{x}, t)$ is the applied force density, and ρ is the free-carrier number density. Also, it is convenient to define $\vec{F}$ in complex envelope notation where $f(\vec{x}, t) = q\rho(\vec{x}, t)\xi(\vec{x}, t)$ is the applied force density envelope function. Equation (3.12) is Fourier transformed into the frequency domain, the complex envelope expressions are substituted and phase matched, the scalar product with the $\hat{x}$ direction is taken, and the free-carrier current density envelope j_{fc} is related to the force density in frequency space.

$$\tilde{j}_{fc}(\vec{x}, \omega - \omega_0) = \frac{q}{m} (\tau_c^{-1} - i\omega)^{-1} \tilde{f}(\vec{x}, \omega - \omega_0) \tag{3.13}$$

The $(\tau_c^{-1} - i\omega)^{-1}$ quantity in Eq. (3.13) is Taylor expanded about ω_0 and the entire equation is inverse Fourier transformed back into the time domain. An investigation of the analyticity

of the expansion in frequency space shows that it will converge for pulses as short as one optical cycle in duration as well as for all values of τ_c, making the result applicable in any situation where Eq. (3.10) is valid. After a transformation into the retarded time frame the final result is

$$j_{fc}(\vec{x},\tau) = \frac{q^2\,\tau_c}{m}\left(\frac{1+i\omega_0\tau_c}{1+\omega_0^2\tau_c^2}\right)\hat{G}^{-1}\,[\rho(\vec{x},\tau)\xi(\vec{x},\tau)] \tag{3.14}$$

where

$$\hat{G}^{-1} = \sum_{m=0}^{\infty}\left(\frac{-i}{\omega_0}g\partial_\tau\right)^m = \left(1+\frac{i}{\omega_0}g\partial_\tau\right)^{-1} \tag{3.15}$$

is the inverse free charge dispersion operator in Eq. (3.2), and $g = (-i\omega_0\tau_c)/(1-i\omega_0\tau_c)$ is a dimensionless complex constant that distinguishes the operators $\hat{T}$ and $\hat{G}$. Substituting Eq. (3.14) into Eq. (3.10) gives the stated result of Eq. (3.2), where the cross section of inverse Bremsstrahlung absorption $\sigma = q^2\tau_c/n_0 c\epsilon_0 m(1+\omega_0^2\tau_c^2)$ and $n_0 = k_0 c/\omega_0$ is the linear index of refraction.

The dispersion corrections for free carriers as predicted by $\hat{G}$ are clearly distinct from the other steepening operators $\hat{T}$ and $\hat{U}$, in that the time derivative coefficient of $\hat{G}$ contains both real and imaginary parts. This distinguishing trait is ultimately traceable to the different physical origins of the respective operators. The operator $\hat{T}$ originates from residual time derivatives on the right-hand side of Eq. (3.3), the operator $\hat{U}$ originates from linear dispersion relations of bound charges and a coordinate transformation, and the operator $\hat{G}$ originates from dispersion relations of free charges according to the Drude model.

Since it has already been established that the approximation $\hat{U} \approx \hat{T}$ is widely applicable then perhaps the same is true of $\hat{G}$. This, however, would require that the constant $g \approx 1$, which is clearly not the case for collision times on the order of the optical cycle, $T_{oc} = 2\pi/\omega_0$, or less. Figure (3.1) shows the magnitude of the real and imaginary parts of g as a function of τ_c/T_{oc}. It is therefore worth examining whether collision times on the order of one optical cycle have been published in the recent literature. Table 3.1 shows a list of free-carrier collision times measured in experiment or used in simulation for a variety of materials in

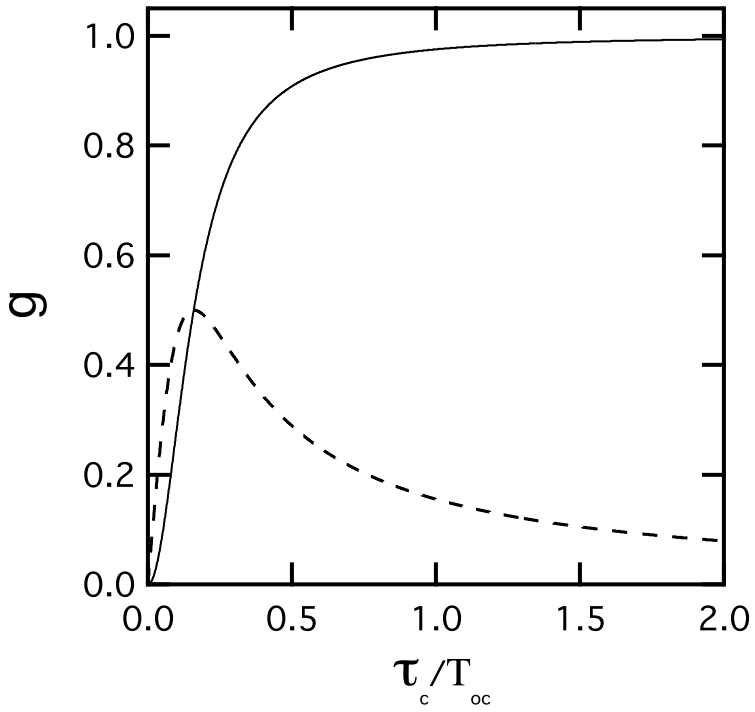

Figure 3.1: The magnitude of the real (solid line) and the imaginary (dashed line) parts of the dimensionless constant g as a function of the characteristic free-carrier collision time τ_{c} scaled by the optical cycle T_{oc} of the applied field.

Table 3.1: A list of electronic collision times τ_c provided in recent literature for experiments and simulations using 800 nm light. Collision times are shown in units of fs as well as number of optical cycles for the 800 nm wavelength. Also shown is the specific material for each collision time and references from which the collision times are taken or calculated.

τ_c (fs)	τ_c/T_{oc}	*Materials*	*References*
0.2	0.075	fused silica	[75]
0.4	0.15	fused silica, epithelium	[76]
0.7	0.26	stroma	[76]
1.0	0.37	fused silica	[19]
1.27	0.48	fused silica	[14]
1.7	0.64	fused silica	[77]
2.12	0.79	sapphire	[74]
3.0	1.12	water	[68]
10	3.8	fused silica	[69] [64]
20	7.5	fused silica	[46]
23.3	9.4	fused silica	[70]
350	112	air	[52]

the recent literature. Note that many of these collision times are indeed on the order of one optical cycle or less.

It should be emphasized, however, that if one examines the $\hat{G}$ operator in the limit of $\tau_c \gg T_{oc}$ then $\hat{G} \rightarrow \hat{T}$ and Eq. (3.1) is recovered. More importantly, in the same limit Eq. (3.14) reduces to the result derived in Ref. [46], which uses an operator expansion in time that requires the condition $\omega_0 \tau_c \gg 1$ to converge. Note that such a condition would not be satisfied for the lower collision times listed in Table 3.1. Additionally, in the extreme limit of zero dissipation (*i.e.* $\tau_c \rightarrow \infty$), then $j_{fc}(\vec{x},t) \rightarrow i(q/m\omega_0)\hat{T}^{-1}\left[\rho(\vec{x},t)\xi(\vec{x},t)\right]$, which is the limiting case for a plasma of truly free particles [78].

3.2.4 The modified NLSE

To fully characterize Eq. (3.10), a form for the nonlinear polarization envelope must be specified. In this dissertation the nonlinear polarization derived in Ref. [29] is selected because of its demonstrated ability to describe the delayed nonlinear optical response of fused silica. Combining this with the free-carrier and photoionization currents derived in Secs. (3.2.2) and (3.2.3) a modified NLSE is obtained.

$$\begin{aligned}\frac{\partial \xi}{\partial z'} &= \frac{i}{2k_0}\hat{T}^{-1}\nabla_\perp^2\xi + i\hat{D}_b\xi + i\frac{k_0\epsilon_0 c n_2}{2}\left(1-f_r\right)\hat{T}|\xi|^2\xi \\ &\quad + i\frac{k_0\epsilon_0 c n_2}{2}f_r\hat{T}\left[\int_{-\infty}^{\tau} d\tau' R(\tau-\tau')|\xi(\tau')|^2\right]\xi \\ &\quad -\frac{\sigma}{2}\left(1+i\omega_0\tau_c\right)\hat{G}^{-1}\left[\rho\xi\right] - \frac{W_{PI}U}{2\,I}\,\xi\end{aligned} \tag{3.16}$$

Here n_2 is the intensity-based nonlinear index of refraction, f_r is the fraction of the Raman contribution to the nonlinear polarization, and $R(\tau)$ is the Raman response function derived in Ref. [29],

$$R(\tau) = \frac{\tau_1^2+\tau_2^2}{\tau_1\tau_2^2}\,e^{-\tau/\tau_2}\,\sin(\tau/\tau_1),$$

where the constants τ_1 and τ_2 are adjustable parameters chosen to provide an adequate fit with the Raman-gain spectrum [25]. The nonlinear polarization term in Eq. (3.16) now accounts for self-focusing, self-steepening (nonlinear shock), and stimulated Raman scattering. Eq. (3.16) is the modified NLSE the author proposes as the generally correct choice for ultrashort pulse propagation through regions of dense plasma. The remainder of this chapter will explore the significant differences that arise from using Eq. (3.1) as the free-carrier contribution to the modified NLSE instead of Eq. (3.2) and how such differences might arise in experiment.

3.3 Analysis of free-carrier contributions to the modified NLSE

This section will explore the predictions of Eqs. (3.1) and (3.2) as descriptions of free-carrier optical effects. It is instructive to examine the corrections to absorption and phase separately

when time derivatives of the complex field envelope are present. Therefore, by taking the free-carrier temporal correction operators $\hat{T}^{-1}$ and $\hat{G}^{-1}$ to first order, the changes in intensity, I, and spatio-temporal phase, ϕ, with respect to the propagation axis are:

$$\left[\frac{\partial I}{\partial z'}\right]_{fc} = -\sigma\rho I - \sigma\beta\tau_{\mathrm{c}}\left[\dot{\rho}I + \rho\frac{\dot{I}}{2}\right] - \sigma\rho I\eta\frac{\dot{\phi}}{\omega_0} \tag{3.17a}$$

$$\left[\frac{\partial \phi}{\partial z'}\right]_{fc} = -\frac{\sigma}{2}\,\omega_0\tau_{\mathrm{c}}\rho + \frac{\sigma\eta}{2\omega_0}\left[\frac{\rho\dot{I}}{2I} + \dot{\rho}\right] - \frac{\sigma}{2}\beta\tau_{\mathrm{c}}\rho\dot{\phi} \tag{3.17b}$$

where all dotted terms indicate time derivatives, and β and η are dimensionless constants which again distinguish between the descriptions of Eq. (3.1) and Eq. (3.2). Table 3.2 lists the values for the constants η and β for three different descriptions of free-carrier effects. If Eq. (3.1) is chosen as a description of free-carrier effects then these constants are simply $\beta = \eta = 1$ and this description will henceforth be referred to as model I. If instead Eq. (3.2) is chosen as a description of free-carrier effects then the two constants are related by $\eta = \beta + 1$ where $\beta = (\omega_0^2\tau_{\mathrm{c}}^2 - 1)/(1 + \omega_0^2\tau_{\mathrm{c}}^2)$; this will be referred to as model II. Additionally, a zeroth temporal order approximation of both models I and II ($\hat{T}^{-1} = 1$ and $\hat{G}^{-1} = 1$, respectively) is shown for comparison and will be referred to as model III. In this case there are no time derivative corrections to the free-carrier contribution and the constants are therefore $\eta = \beta = 0$. Table 3.2 also introduces a color scheme that will be used to distinguish between the three models in the data to be presented throughout this chapter; model I shown in blue, model II shown in red, and model III shown in black.

Figure (3.2) shows the numerical value of β as function of $\tau_{\mathrm{c}}/T_{\mathrm{oc}}$ for model II. As expected, for collision times of one optical cycle or less the value of β for model II shows considerable deviation from unity, and thus models I and II are not in agreement in this regime. For collision times greater than two optical cycles, Fig. (3.2) shows that models I and II will be in very good agreement on the value of $\beta = 1$. However, agreement between the models for the constant η is a very different matter. In fact models I and II only agree on the value of η at a single collision time of $\tau_{\mathrm{c}} = \omega_0^{-1}$, which is only a fraction of an optical cycle and simultaneously where $\beta = 0$ for model II. Furthermore, models I and II will disagree

Table 3.2: Three different models of free-carrier effects used in this chapter and their respective values for the constants η and β in Eq. (3.17).

Model I (*red, dotted*)	*Model* II (*blue, dashed*)	*Model* III (*black, solid*)
Eq. (3.1)	Eq. (3.2)	Eq. (3.1), $\hat{T}^{-1} = 1$
$\eta = 1$	$\eta = \beta + 1$	$\eta = 0$
$\beta = 1$	$\beta = (\omega_0^2\tau_c^2 - 1)/(1 + \omega_0^2\tau_c^2)$	$\beta = 0$

on the value of η by a factor of two for any collision time greater than two optical cycles, thereby extending the range of collision times where such differences could be significant. Here it is important to recall that the cross section of inverse Bremsstrahlung absorption, σ, is also a function of the collision time and will decrease as the imaginary part of g decays for increasing τ_c (see the dashed line in Fig. (3.1)). This ensures that differences between the respective calculations of η will become gradually less significant as one approaches the limit of small dissipation (*i.e.* $\tau_c \gg T_{oc}$).

Equation (3.17) allows one to determine which pulse attributes will accentuate the differences between models I and II. For example, a strongly chirped pulse ($\dot{\phi} \sim \pm\omega_0$) will make contributions to the spatio-temporal phase (the third term on the RHS of Eq. (3.17b)) equal in magnitude to that of the zeroth temporal order (first term on the RHS of Eq. (3.17b). However, in the case where $\tau_c = \omega_0^{-1}$ this entire contribution is eliminated in model II because $\beta = 0$ under that description. The same is true for the plasma generation and pulse steepening term of Eq. (3.17a), the second term on the RHS. If instead collision times greater than one optical cycle are adopted, then $\beta \approx 1$ for models I and II while their respective values for the constant η differ by a factor of two. Here strongly chirped pulses will make contributions to plasma absorption (Eq. (3.17a)) of similar magnitude to the zeroth temporal order, but the chirp contribution of model II will be twice as strong as the model I

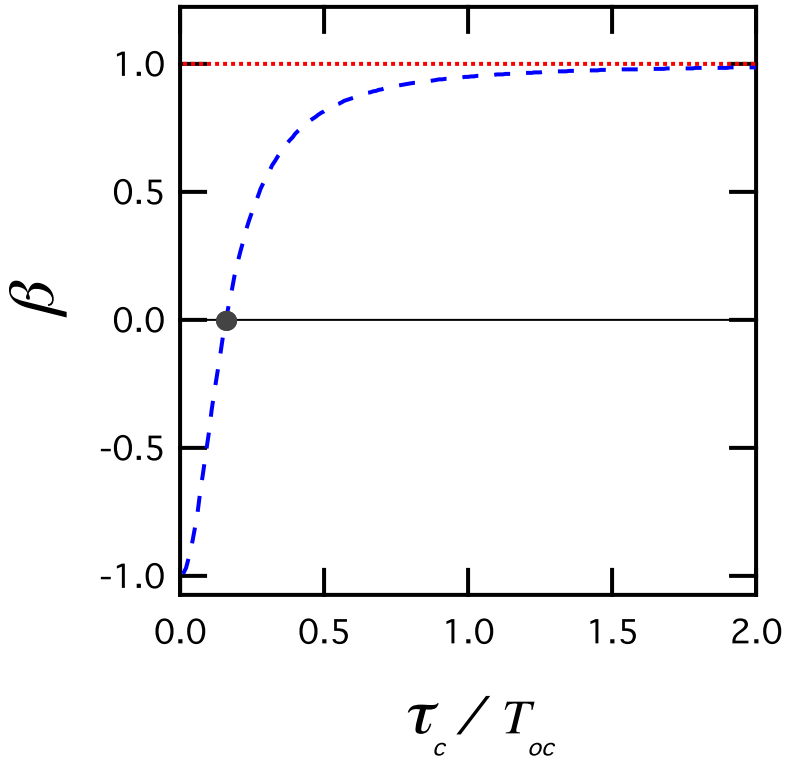

Figure 3.2: The dimensionless constant β as a function of the collision time scaled by the optical cycle of the applied field. The dotted red line represents model I, the dashed blue line represents model II, and the solid black line represents model III shown for comparison. The grey dot indicates the collision time at which model II and model III are in exact agreement for the value of $\beta = 0$.

contribution. Analogously, the same is true for the plasma generation and pulse steepening terms of Eq. (3.17b).

It should be emphasized that any dissimilarities between the models of free-carrier effects will be comparatively stronger on the trailing edge of the pulse, because the plasma density ρ has had more time to accumulate. Note that on the trailing edge of the pulse, $\dot{I}$ will be negative by definition, while the sign of the plasma generation rate $\dot{\rho}$ will depend on the description one uses to calculate ρ as a function of time. Also, it will often be the case that $\dot{\phi}$ will be negative on the trailing edge of the pulse due to self phase modulation ($\dot{\phi} \sim n_2 \dot{I}$) and plasma induced blue shifting [52; 79]. Under such conditions Eq. (3.17) predicts that model I will significantly mischaracterize the effects of plasma absorption and defocusing on the trailing edge of the pulse. It is notable that the value of the collision time has been interpreted as a measure to characterize the balance between plasma absorption and plasma defocusing [64]. This being the case, model I will significantly mischaracterize the balance of plasma absorption and defocusing for a large range of collision times currently used in the literature. These effects are detectable by examining phase accumulation and energy absorption during ultrashort pulse propagation, which is addressed using numerical simulation as described in the next section.

3.4 Description of Simulations

In order to explore how the different models of free-carrier effects compare with other ultrashort optical processes, simulations have been performed solving Eq. (3.16) in fused silica at a peak laser wavelength of 800 nm. This material and wavelength were chosen because the optical properties of fused silica are comparatively well characterized in the literature for 800 nm light. Additionally, Table 3.1 shows that the values of the collision time for fused silica used in the literature span more than three orders of magnitude, encompassing collision times much less than, on the order of, and much greater than a single optical cycle for an 800

Table 3.3: A list of the optical and material parameters used for all the simulations reported in this chapter. Material parameters are those for fused silica.

Symbol	*Description*	*Value*	*Units*
λ	Initial wavelength	800	nm
w_r	Initial beam waist	75	μm
I_0	Initial peak intensity	5.3×10^{13}	W cm^{-2}
L_z	Sample length	100	μm
n_0	Linear refractive index	1.45	
k_2	GVD coefficient	361	fs^{2}cm^{-1}
n_2	Nonlinear refractive index	2.48×10^{-16}	cm^{2}W^{-1}
f_r	Raman response fraction	0.18	
τ_1	Raman sinusoidal time	12.2	fs
τ_2	Raman decay time	32	fs
U	Material band gap	9	eV
m	Reduced electron-hole mass	0.5	m_e
e_0	free-carrier charge	1.602×10^{-19}	C

nm field, making it an ideal material for this study. Table 3.3 lists the optical and material parameters that are used for every simulation reported in this chapter.

Discrepancies between models I and II are examined by simulating the propagation of ultrashort pulses through 100 μm of fused silica. These simulations have been organized to search for such differences over a variety of pulsewidths and collision times. Differences in the results predicted by models I and II should scale inversely with the pulsewidth. Therefore simulations are performed for pulses with FWHM pulsewidths of τ_{fwhm} = 10, 20, and 40 fs. For each value of the pulsewidth, simulations are performed at 15 free-carrier collision times ranging from $0.2 - 16.0$ fs (*i.e.* $0.075 - 6$ optical cycles), thus encompassing most of the collision times found in Table 3.1. Finally, for each pulsewidth and collision time catagory, three simulations are performed using models I , II, and III, respectively, to describe free-carrier effects, making a total of 135 simulations. The initial energy for each pulse was appropriately selected to obtain an incident peak intensity of 5.3×10^{13} W cm^{-2}. Under

the assumption of a flat spatio-temporal phase and cylindrical beam symmetry, the initial electric field envelope is then assigned the form:

$$\xi(r,\tau,z=0)=\xi_0\exp\left(-\frac{r^2}{w_r^2}-\frac{2\ln(2)\tau^2}{\tau_{fwhm}^2}\right), \tag{3.18}$$

where $\xi_0=\sqrt{2I_0/n_0\epsilon_0 c}$.

In solving Eq. (3.16) it is necessary to simultaneously solve a rate equation for the free-carrier plasma density ρ as a function of space and time [12]:

$$\frac{\partial\rho}{\partial t}=W_{PI}(|\xi|). \tag{3.19}$$

In this chapter photoionization is considered as the only generator of free carriers, noting a recent work that found avalanching (impact ionization) to be negligible in fused silica for pulses as short as 90 fs at the intensities under consideration [19]. In principle, however, impact ionization can also be added. Additionally, the generated free-electron densities are at least two orders of magnitude below the molecular density of fused silica, 2.2×10^{22} cm^{-3},[14]. Therefore a full valence band is assumed throughout.

The photoionization rate $W_{PI}(|\xi|)$ is given by the Keldysh formula for photoionization in a solid [80]:

$$W_{PI}(|\xi|)=\frac{2\omega_0}{9\pi}\left(\frac{m\omega_0}{\sqrt{\gamma_1}\,\hbar}\right)^{3/2}Q(\gamma,x)\exp\left(-\varpi\left\langle x+1\right\rangle\right). \tag{3.20}$$

Here the Keldysh parameter $\gamma=\omega_0\sqrt{mU/e_0\,|\xi|}$, $\gamma_1=\gamma^2/(1+\gamma^2)$, $\gamma_2=1-\gamma_1$, $\varpi=\pi\left(K(\gamma_1)-E(\gamma_2)\right)/E(\gamma_2)$, and $x=(2U/\pi\omega_0)(\sqrt{1-\gamma^2}/\gamma)E(\gamma_2)$. The notation $\langle\cdot\rangle$ denotes the integer part, and the functions K and E are complete elliptical integrals of the first and second, respectively, kind as defined in Ref. [81]. The function $Q(\gamma,x)$ is given by

$$Q(\gamma,x)=\sqrt{\frac{\pi}{2K(\gamma_2)}}\sum_{n=0}^{\infty}\exp\left(-n\varpi\right)\Phi\left(\sqrt{\vartheta(n+2\nu)}\right),$$

where $\vartheta=\pi^2/4K(\gamma_2)E(\gamma_2)$, $\nu=\langle x+1\rangle-x$, and $\Phi(z)=\int_0^z\exp(y^2-z^2)dy$ is the Dawson function.

The solid line in Fig. (3.3) shows the Keldysh photoionization rate as a function of the optical intensity in fused silica for the parameters listed in Table 3.3. Note that the Keldysh

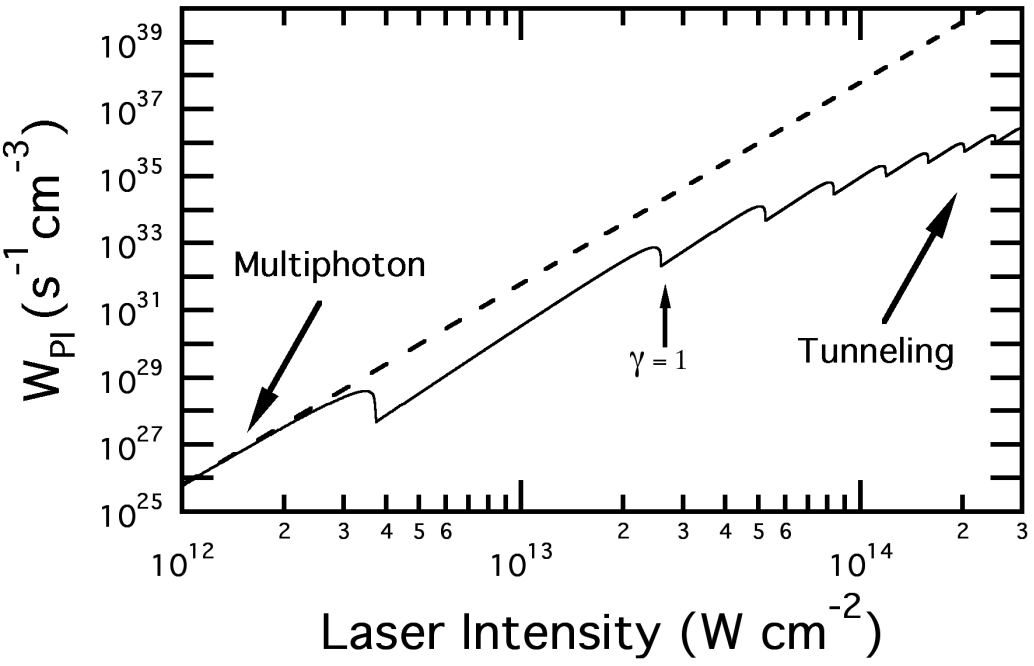

Figure 3.3: Photoionization rate as a function of optical intensity in fused silica according to the theory of Keldysh. The solid line shows the full Keldysh expression, while the dashed line shows the common multiphoton ionization approximation valid at low intensities. Optical and material parameters used to calculate this rate are those from Table 3.3.

parameter γ is used to distinguish between the domains of multiphoton ionization (MPI) ($\gamma \gg 1$) and tunneling ionization ($\gamma \ll 1$). In the presented simulations the condition $\gamma = 1$ is satisfied at an intensity of 2.7×10^{13} W cm^{-2}. The dashed line in Fig. (3.3) shows the Keldysh MPI rate; $W_{PI} = \sigma_6 I^6$, where $\sigma_6 = 6.04 \times 10^{-47}(\text{cm}^2\ \text{W}^{-1})^6\text{s}^{-1}\text{cm}^{-3}$ for the chosen parameters in this chapter. Because the simulations in this chapter never exceed their initial peak intensity of 5.3×10^{13} W cm^{-2}, most of the pulses lay in the domain of multiphoton ionization. However, the peak intensities in these simulations are too high to be accurately modeled by the MPI rate and yet too weak to be in the tunneling regime. Therefore the full Keldysh photoionization formula is used throughout.

For the simulations in this chapter, it was sufficient to set the bound charge dispersion operator to $\hat{D}_b = -i(k_2/2)\partial_\tau^2$, as no linear absorption from bound charges is assumed ($\alpha_m = 0$), and higher linear dispersion terms were found to have no significant effect when included. In fact, even group velocity dispersion had only small effects, because the propagation distance of 100 μm is very small compared to the group velocity dispersion (GVD) length $L_{\text{GVD}} = \tau_{fwhm}^2/|k_2| \sim 1$ cm for the shortest pulse (the 10 fs pulse). Additionally, a relatively large beam waist of 75 μm was chosen for a peak intensity of 5.3×10^{13} W cm^{-2}. This was done in an effort to reduce the influence of spatial diffraction and allow one to concentrate on how ultrashort free-carrier effects compare with other nonlinear optical processes. Eq. (3.16) is solved using a split step method, with the first two terms of the right-hand side constituting a "linear" step and the rest of the terms constituting a "nonlinear" step. Eq. (3.16) is solved simultaneously with Eq. (3.19), which is in turn solved using a fourth order Runge-Kutta method.

3.5 Results

Figure (3.4) shows the total energy transmission (transmittivity) as a function of the free-carrier collision time after propagating through a 100 μm sample of fused silica. For $\lambda = 800$ nm, one optical cycle is ≈ 2.67 fs; the values of τ_c in the plots of Fig. (3.4) range from 0.075 to

6 optical cycles (0.2 - 16 fs), covering three orders of magnitude in order to sample the wide range of collision times listed for fused silica in Table 3.1. The transmittivity plots are shown for each of the three initial pulses with FWHM pulsewidths of 10, 20, and 40 fs. Each plot in the figure shows results from the free-carrier descriptions of model I (dotted line) model II (dashed line) and model III (the zeroth temporal order approximation of models I and II, shown for comparison as a solid line). These are further distinguished by a color scheme of red, blue, and black, respectively; *i.e.* the convention introduced in Table 3.2. Note the discrepancies in transmittivity on the order of 1% that occur between models I and II for a 10 fs pulse. Equally notable is the fact that this difference in transmittivity can be seen over the large range of collision times ranging from approximately 1 fs and finally converging at about 16 fs. This range of discrepancy extends over 5.5 optical cycles of collision time and is the direct result of the pulse chirp term in Eq. (3.17a), which demonstrates that only instantaneous frequency shifts can cause discrepancies of this kind for collision times greater than one optical cycle. These differences also occur for the 20 and 40 fs pulse transmittivity plots. As expected, pulses with the same initial intensity but a longer pulsewidth will ultimately decrease the magnitude of all field time derivative corrections.

To show specific discrepancies arising in intensity and phase at the trailing edges of the pulses, results from some of the most instructive simulations are examined. Figs. (3.5−3.8) show selected intensity and phase profiles comparing the three aforementioned models of free-carrier effects. The figures use the same graphing and color convention introduced in Table (3.2). These figures are organized in an identical manner to display the spatial intensity at the trailing edge of the pulse, $I(r, \tau = +\tau_{fwhm})$; the temporal intensity at the spatial center, $I(r = 0, \tau)$; the spectral intensity at the spatial center, $S(r = 0, \omega) = (1/2)n_0\epsilon_0 c \left|\tilde{\xi}(r = 0, \omega - \omega_0)\right|^2$; and the corresponding phase for each intensity. Also shown is the maximum plasma density as a function of the propagation distance. Note that all maximum plasma densities are at least an order of magnitude below the threshold of permanent

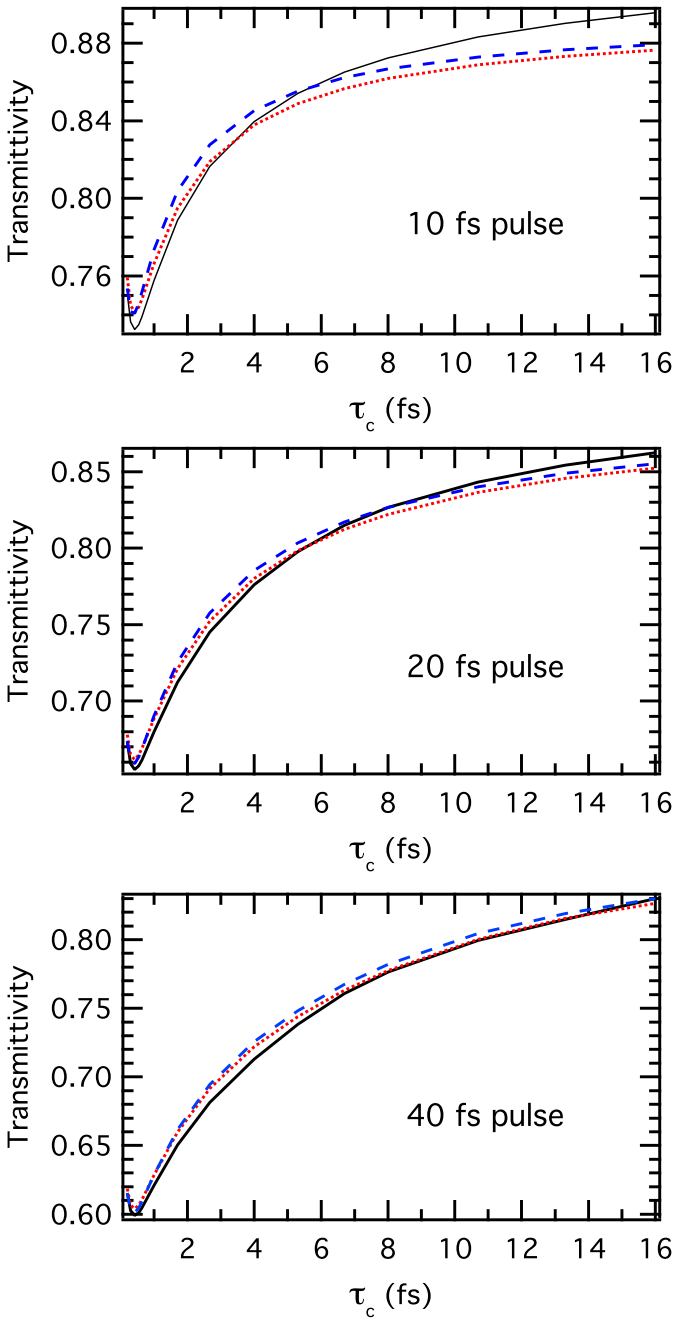

Figure 3.4: Transmittivity after propagating through 100 μm of fused silica shown for 10, 20 and 40 fs pulses. Transmittivity is shown as a function of the free-carrier collision time. The dotted red line represents model I, the dashed blue line represents model II, and the solid black line represents model III shown for comparison.

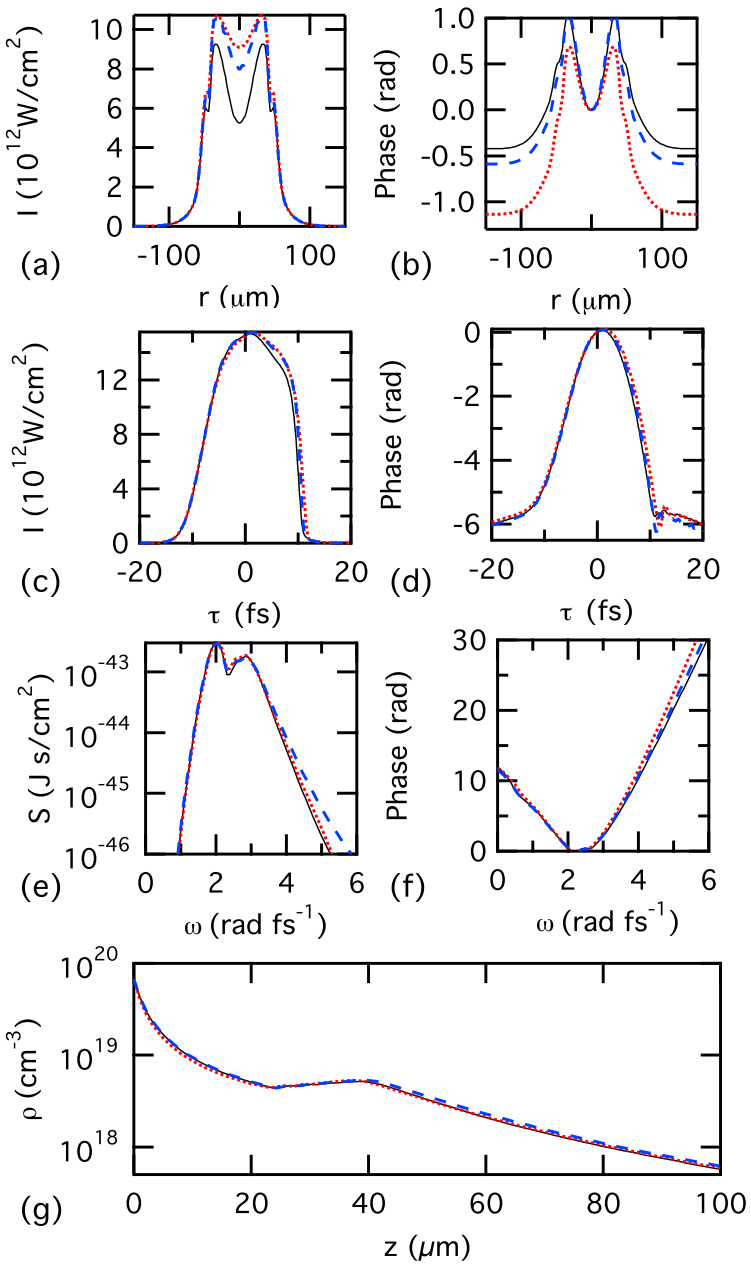

Figure 3.5: Selected results of a 10 fs pulse after propagating through 100 μm of fused silica with a free-carrier collision time of 0.42 fs. The dotted red line represents model I, the dashed blue line represents model II, and the solid black line represents model III. (a) and (b) show the spatial intensity and phase at the trailing edge of the pulse ($\tau = 10$ fs), (c) and (d) show the temporal intensity and phase at the spatial center ($r = 0$), (e) and (f) show the spectral intensity and phase at the spatial center ($r = 0$), and (g) shows the peak plasma density as a function of the propagation distance.

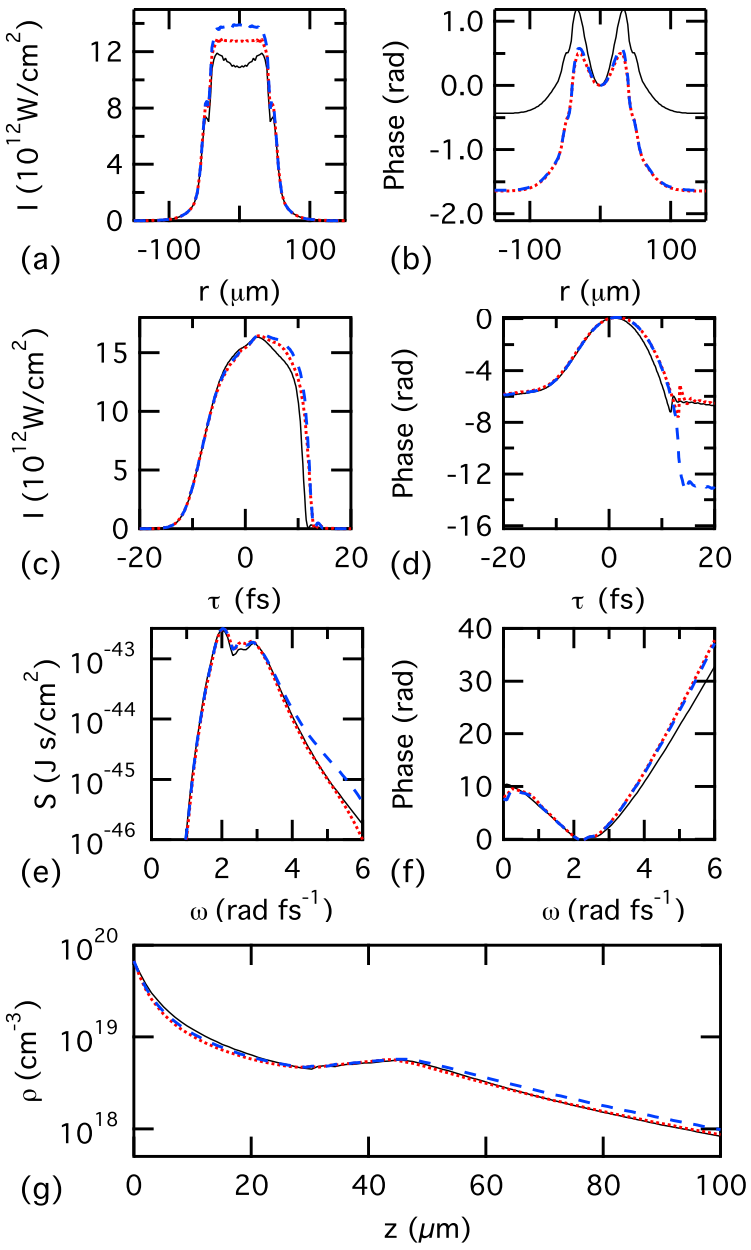

Figure 3.6: Selected results of a 10 fs pulse after propagating through 100 μm of fused silica with a free-carrier collision time of 1.0 fs. The dotted red line represents model I, the dashed blue line represents model II, and the solid black line represents model III. (a) and (b) show the spatial intensity and phase at the trailing edge of the pulse ($\tau = 10$ fs), (c) and (d) show the temporal intensity and phase at the spatial center ($r = 0$), (e) and (f) show the spectral intensity and phase at the spatial center ($r = 0$), and (g) shows the peak plasma density as a function of the propagation distance.

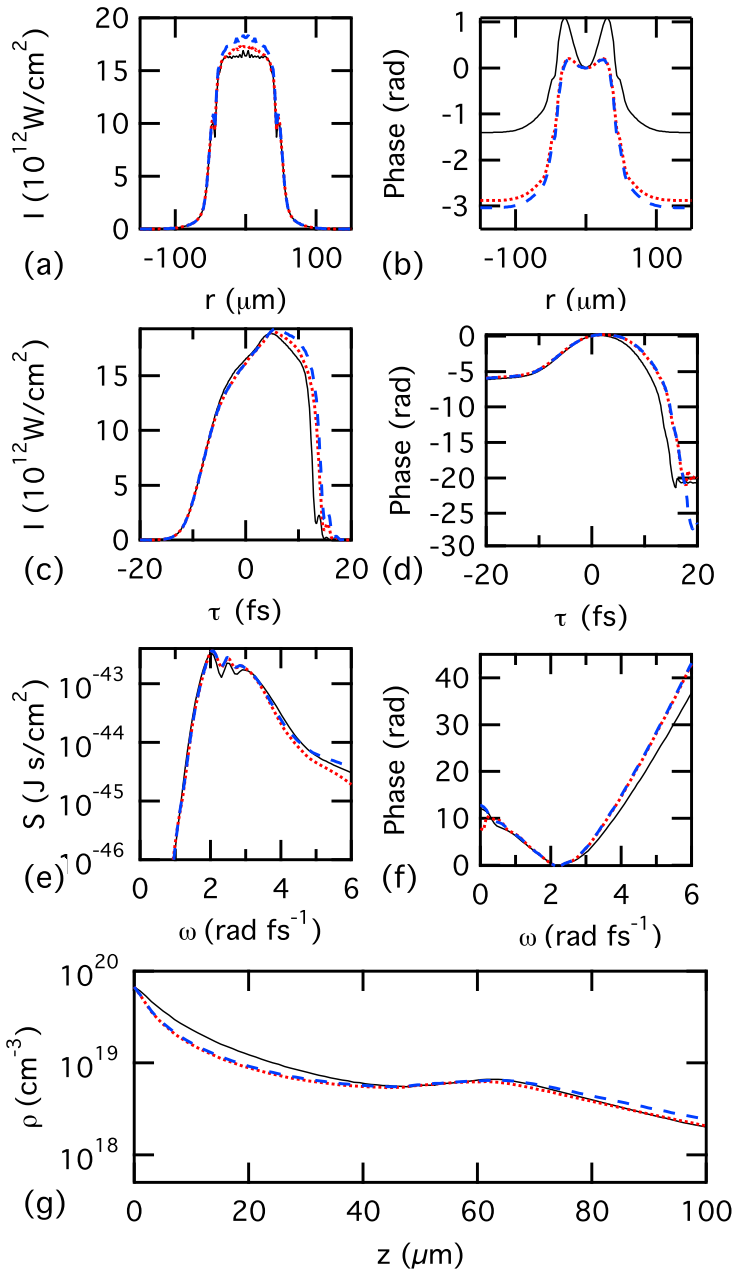

Figure 3.7: Selected results of a 10 fs pulse after propagating through 100 μm of fused silica with a free-carrier collision time of 2.6 fs. The dotted red line represents model I, the dashed blue line represents model II, and the solid black line represents model III. (a) and (b) show the spatial intensity and phase at the trailing edge of the pulse ($\tau = 10$ fs), (c) and (d) show the temporal intensity and phase at the spatial center ($r = 0$), (e) and (f) show the spectral intensity and phase at the spatial center ($r = 0$), and (g) shows the peak plasma density as a function of the propagation distance.

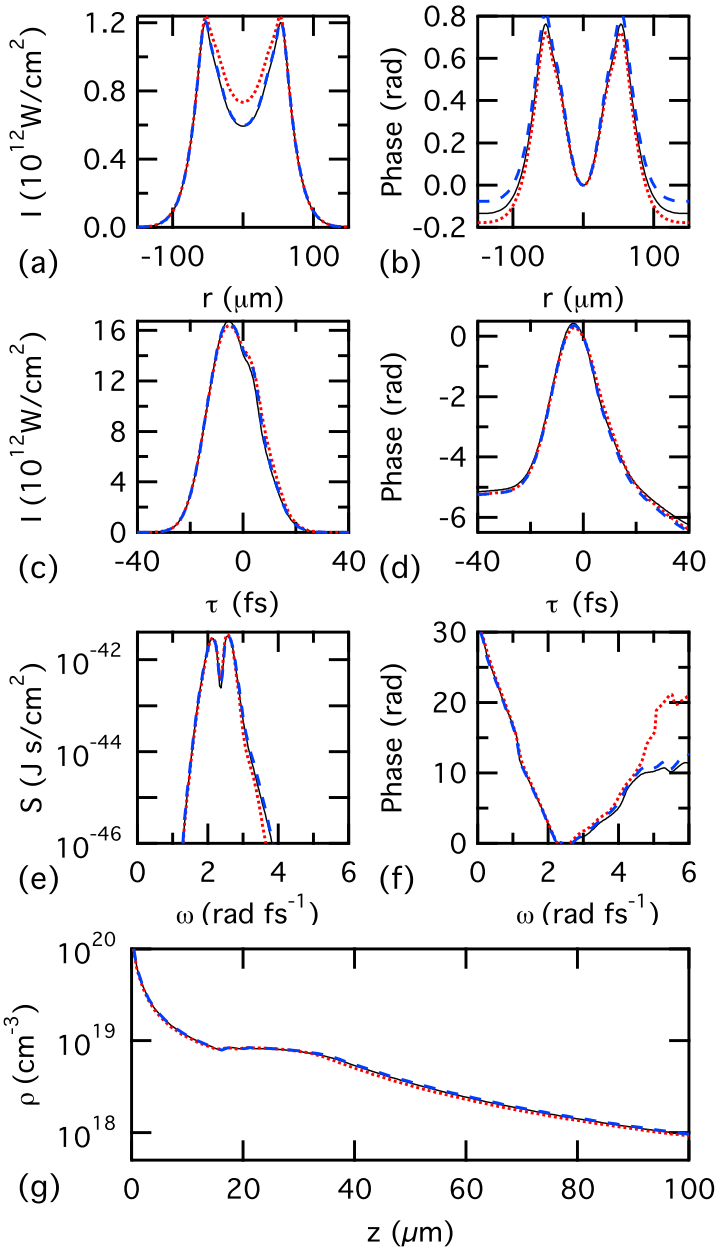

Figure 3.8: Selected results of a 20 fs pulse after 100 μm of propagation in fused silica with a free-carrier collision time of 0.42 fs. The dotted red line represents model I, the dashed blue line represents model II, and the solid black line represents model III. (a) and (b) show the spatial intensity and phase at the trailing edge of the pulse ($\tau = 20$ fs), (c) and (d) show the temporal intensity and phase at the spatial center ($r = 0$), (e) and (f) show the spectral intensity and phase at the spatial center ($r = 0$), and (g) shows the peak plasma density as a function of the propagation distance.

structural damage in fused silica, and yet frequently above a recently established value for reversable refractive index modification [64].

Figure (3.5) shows results from 10 fs pulse propagation for a collision time of 0.42 fs. The collision time of 0.42 fs ($\tau_c = \omega_0^{-1}$) is of special significance, as this results in the constant β in Eq. (3.17) equals zero for model II. As discussed in Sec. (3.3), this collision time results in a significant disagreement between the two free-carrier dispersion descriptions on the contribution from plasma generation and pulse steepening to energy absorption, as well as the contribution of instantaneous frequency shift (pulse chirp) to the spatio-temporal phase at this collision time. Plots (a) and (b) in Fig. (3.5) show how strong this disagreement becomes at the trailing edge of the pulse, where the plasma density is highest. Although the differences in the spatial intensity are indeed noticeable, it is the spatial phase that displays the largest discrepancy between the descriptions of free-carrier effects in Fig. (3.5). It is evident from the temporal phase in Fig. (3.5d) (due largely to self phase modulation) that there is an average temporal chirp of $\dot{\phi} \approx -\omega_0/4$ on the trailing edge of the pulse. The last term in Eq. (3.17b) explains how the presence of such a strong temporal chirp at the trailing edge of the pulse leads to better agreement between model II and model III than with model I in spatial phase; because $\beta = 0$ for models II and III, whereas $\beta = 1$ for model I.

Figs. (3.6) and (3.7) show results from 10 fs pulse propagation in a material with electron collision times of 1.0 and 2.67 fs, respectively. Figures (3.6b) and (3.7b) show little or no difference in the spatial phase at the trailing edge of the pulse. However, these figures do reveal very subtle differences between the free-carrier descriptions in the plots of temporal intensity, temporal phase, spectra and maximum plasma densities. Figure (3.8) shows selected profiles for 20 fs pulse propagation with a collision time of 0.42 fs. Comparison of Figs. (3.5b) and (3.8b) demonstrates how doubling the pulsewidth dramatically reduces the discrepancies between the three free-carrier descriptions. Although a small difference in spatial intensity is retained in Fig. (3.8a), all other intensity and phase profiles, as well as the maximum plasma densities, of models I and II are in very good agreement with the

zeroth temporal order approximation description of model III. This makes the discrepancies between the free-carrier descriptions at higher pulsewidths and collision times in Fig. (3.4) most interesting, because such differences, though difficult to detect in an individual profile will, upon integration over the entire pulse intensity, yield noticeable changes in the total pulse energy. At longer pulsewidths or higher intensities, plasma densities sufficient to cause permanent optical damage will occur, increasing the magnitude of these discrepancies. A study of such effects, however, would likely necessitate the inclusion of avalanching in the temporal evolution of the free-carrier plasma. The process of impact ionization depends sensitively on the description of free-carrier absorption [11; 55; 56], which in turn can be significantly influenced by ultrashort effects, as demonstrated by Eq. (3.17a). The resulting significance of temporal corrections to the avalanching has yet to be addressed in the literature, to the author's knowledge. Such an investigation is currently planned as a future study.

3.6 Conclusion

A modified nonlinear Schrödinger equation has been derived that includes a free-carrier contribution calculated from the Drude model. Intrinsic to this calculation is an inverse free charge dispersion operator whose expansion converges for all values of the free-carrier collision time, as well as for laser pulses as short as a single optical cycle. It therefore retains all of the specified information about free-charge dispersion contributions without resorting to a limiting case, and provides an accurate description of a Drude free-carrier current density wherever the modified NLSE is valid. The free-carrier current density derived in this chapter and the dispersion relations contained therein are shown to converge to other descriptions of ultrashort free-carrier current densities currently in use in the literature for the limiting case in which the collision time is much greater than an optical cycle. If, however, the free-carrier collision time is on the order of one optical cycle or less, then significant differences in plasma absorption and defocusing may arise for pulses that are strongly chirped or steepened.

Collision times in the range of one optical cycle or less are frequently cited or measured in the literature, while the use of ultrashort pulses with steep edges and large frequency shifts are ubiquitous. Simulations presented in this chapter suggest that strongly chirped ultrashort pulses, with an instantaneous frequency shift comparable to the carrier frequency, may effect changes to energy absorption and phase accumulation that only the free-carrier dispersion relations derived in this chapter are adequate to explain. As research into laser-induced damage and laser-plasma interactions further engages the use of ultrashort pulses that approach a single optical cycle, this chapter should provide a more general and complete method for describing free-carrier dispersion relations in the context of a nonlinear envelope propagation equation.

Chapter 4

Simulations of Pulse Propagation and Plasma Generation using Asymmetrical Beams and Pulses

Recent experiments on optical damage by ultrashort laser pulses have demonstrated that the temporal pulse shape can dramatically influence plasma generation in fused silica [14]. In this chapter a modified 3+1D nonlinear Schrödinger equation for the pulse propagation, coupled to a rate equation for the plasma density in the dielectric material, is used to simulate pulse propagation and plasma formation in fused silica. Results are presented from simulations performed to analyze the influence of pulse shape and beam geometry on the formation of the electron plasma and hence modification in the bulk material. In particular, the effect of pulses reconstructed from experimental data is simulated. It is expected that a better understanding of the dynamics of laser-induced plasma generation will enable the accurate simulation of optical damage in a variety of dielectrics, ultimately leading to an enhanced control of optical damage to real materials and optical devices. The work presented in this chapter closely follow publications by the J. R. Gulley, S. W. Winkler, and W. M. Dennis in Refs. [8; 9].

4.1 Motivation

Over the past decade there has been a significant increase in the demand for methodologies for accurate and reproducible modification of materials on both the micrometer and nanometer length scales [14; 15; 17; 61–63]. In particular, it is desirable to effect modifications to a given material's optical properties, *e.g.* the creation of waveguide [18] or grating structures[5], while avoiding the onset of irreversible damage [61]. High-intensity, ultrashort laser pulses

are now finding use in micro-machining and nanostructuring applications because of the ability to make precise material modifications both on the surface and in the bulk, without causing permanent damage to the material [64]. The widespread use of ultrashort pulses for this purpose necessitates developing a more detailed and fundamental understanding of the physical processes leading to such modification and damage on the sub-picosecond time scale [65; 66]. Ultimately, this must involve a systematic investigation of the interplay between high-intensity ultrashort pulse propagation and the generation of free-carrier plasmas within the material [5; 11].

The development of general and widely applicable models for ultrafast laser pulse induced plasma generation has been addressed by numerous authors [5; 9–12; 19; 46; 63; 65; 66; 80; 82–88]. To date, many authors have used cylindrically symmetric, single pulse (2+1D) simulations of laser pulse propagation both for comparison with experimental results and to develop a more general understanding of ultrafast optical damage [5]. The ubiquity of 2+1D simulations is understandable considering the computational, memory, and storage requirements necessary to simulate the propagation of complex, three-dimensional fields that can undergo significant phase and structural distortions due to nonlinear effects. However, the case for running simulations with more complicated beam structures and pulse shapes has already been made by other authors [89; 90]. With continuing advances in computational hardware, there is good reason to expect that fully three-dimensional pulse (3+1D) simulations will play an increasingly important role in providing a more realistic comparison with experimental results, particularly in cases where it is important to accurately determine damage thresholds for asymmetrical beams and pulses. In this chapter, 3+1D pulse propagation simulations have been used to explore the effects of double-pulse sequences and asymmetrical beam profiles on plasma generation in fused silica. These simulations were performed over a range of pulse energies, with particular emphasis on determining the effect of both the spatial beam profile and the temporal pulse shape on laser pulse induced plasma, as suggested by recent work in the literature [63; 87; 91].

4.2 Simulations of Ultrashort Pulse Propagation and Plasma Generation in Fused Silica

In this chapter, the electric field of a linearly polarized laser pulse can be expressed in terms of a slowly varying, complex envelope function as described by Eq. (3.5a) [3]. The evolution of ultrashort pulses along the propagation axis may be described by the modified nonlinear Schrödinger equation (NLSE) derived in Chapter 3.16. The description of plasma generation in this chapter is based on a modified version of the single-rate equation model proposed by Stuart [12] and is briefly introduced below.

Attempts to derive a comprehensive model of plasma generation have been made by many authors [5; 10–12; 19; 46; 63; 65; 66; 80; 82–88]. The simulations in this chapter use the model developed by Stuart *et al.* [12; 83] which has been modified to account for saturation of the plasma density and conservation of momentum during impact ionization [14; 19]. Electrons in the valence band are excited to the conduction band either by photoionization or by impact ionization (avalanche) processes; relaxation to the valence band occurs through electron-hole recombination. In the single-rate equation model, the time evolution of the plasma density is described by [14]

$$\frac{d\rho}{dt} = \left(W_{\mathrm{PI}} + \frac{\sigma I \rho}{(1 + m/m_e) U_{\mathrm{eff}}} \right) \left(1 - \frac{\rho}{\rho_{\max}} \right) - \frac{\rho}{\tau_r}, \tag{4.1}$$

where $U_{\mathrm{eff}} = (U_0 + e^2 |\xi|^2 / 4m\omega_0^2)$ [40] is the effective band gap taking into account the "wiggle energy" of the electron in an applied field, m_e is the electron rest mass, and τ_r is the electron recombination time. In this chapter the Keldysh theory of photoionization of solids [80] is used to calculate the photoionization rate W_{PI} as given by Eq. (3.20). The Keldysh theory has been widely used to describe photoionization in fused silica and other optical glasses [5; 14; 19; 64; 65; 91].

In general terms the behavior predicted by Eq. (3.16) and Eq. (4.1) is as follows: seed electrons are initially generated by a highly nonlinear photoionization process; these electrons can then absorb sufficient energy from the laser pulse to undergo impact ionization [14]. At

the leading edge of the pulse (provided the plasma density is still far below saturation), the instantaneous intensity can reach a threshold value ($\sim$1 TWcm^{-2} in fused silica) where the avalanche rate will balance the decay rate due to electron recombination. The plasma density will then experience a net gain so long as the instantaneous intensity remains above this threshold, perhaps far into the tail of the pulse. Thus plasma densities can be achieved that may cause either reversible or permanent modifications to the material. The work presented in this chapter is concerned with exploring the details of plasma generation in the intensity regime where photoionization, avalanche, and electron recombination processes all contribute significantly to the plasma evolution.

Computer simulations based upon the numerical integration of Eq. (3.16) and Eq. (4.1) for the pulse envelope and plasma density, respectively, were performed to investigate pulse propagation and plasma generation in fused silica. Fused silica was chosen because it is very well characterized at a wavelength of 800 nm, which is easily accessed by Ti:sapphire laser systems. The material parameters for fused silica that are used in the simulations of this chapter are summarized in Table 4.2 [14].

Table 4.1: Simulation parameters for fused silica.

Parameter	*Description*	*Value*	*Units*
n_0	Linear refractive index	1.45	
k_2	GVD coefficient	361	fs^{2}cm^{-1}
n_2	Nonlinear refractive index	2.48×10^{-16}	cm^{2}W^{-1}
U_0	Material band gap	9	eV
τ_c	Electron collision time	1.27	fs
m	Reduced electron-hole mass	0.5	m_e
ρ_{max}	Maximum plasma density	6.6×10^{22}	cm^{-3}
τ_r	Electron recombination time	150	fs

Eq. (3.16) is integrated in this chapter using a split step method with the linear diffraction and dispersion terms constituting the linear step and the remaining terms constituting the nonlinear step. The linear step is solved using a Crank-Nicholson finite-difference algorithm, while the nonlinear step is solved in the time domain using a fourth-order Runge-Kutta

method [59]. Eq. (4.1) is solved purely in the time domain using a fourth-order Runge-Kutta method.

All simulations were performed using a 256×256 spatial grid; however convergence was tested using a 512×512 spatial grid. The spatial resolution is taken to be $10w_0/256$, where w_0 is a measure of the beam width. The temporal grids used in these simulations contained either 512 or 1024 points, depending on whether one or two pulses were propagated; again, convergence was tested using higher resolution. For single pulse simulations, the temporal resolution was $10\tau_0/512$, where τ_0 is the $1/e^2$ width of a Gaussian pulse.

The pulse parameters used in the simulations of this chapter were based upon the following considerations: peak powers were chosen to approach and exceed the critical power for catastrophic self-focusing ($\sim$2.6 MW in fused silica); peak intensities were chosen to exceed the threshold above which impact ionization dominates electron recombination ($\sim$1 TW cm^{-2}); however the average fluence was chosen to remain below the theoretical single pulse threshold for permanent surface damage ($\sim$1.6 J cm^{-2}) [14]. Within these criteria, twelve experiments were simulated. All simulations began at the surface of the material and are numerically constructed according to the formulas:

$$\xi(x, y, \tau, z = 0) = \xi_0 \, F(x, y) \, P(\tau), \tag{4.2}$$

$$P(\tau) = \frac{B_1}{\sqrt{2\pi}\tau_0} \exp\left(-\frac{(\tau + \tau_s)^2}{\tau_0^2}\right) + \frac{B_2}{\sqrt{2\pi}\tau_0} \exp\left(-\frac{(\tau - \tau_s)^2}{\tau_0^2}\right). \tag{4.3}$$

Eq. (4.2) allows one to numerically construct pulses with any spatial beam profile, $F(x, y)$, and pulse shape, $P(\tau)$, of the author's chosing. Once a beam profile and pulse shape is chosen the entire system is assigned a total energy, which is used to determine the amplitude constant ξ_0. The formula for the pulse shape in Eq. (4.3) allows one to simulate the propagation of double-pulse trains, where two Gaussian pulses are separated in time by $2\tau_s$ and have relative strengths given by the dimensionless scaling constants B_1 and B_2. Note that if $B_1 = B_2 = 1$ and $\tau_s = 0$ the single Gaussian pulse profile is recovered.

Simulations for the single 1 μJ symmetric pulse (described in detail below) were repeated using a hyperbolic-secant temporal pulse shape. The space-time profiles and peak plasma density plots for both Gaussian and sech^2 pulses are very similar, indicating that the results presented in this chapter would also be applicable if a sech^2 initial pulse shape was assumed. In this chapter $\tau_0 = 150$ fs for all simulations (corresponding to a FWHM pulsewidth of 176 fs). The pulse separation $2\tau_s$ will be taken as either 500 fs or zero.

The beam profile $F(x, y)$ is taken to be either a cylindrically symmetric Gaussian beam profile or an experimentally measured slightly asymmetrical beam profile. When assigned a cylindrical Gaussian beam profile, $F(x, y)$ has a $1/e^2$ width of 5.8 μm. In order to obtain the experimental spatial profile, pulses from a Clark MXR CPA-2010 Ti:sapphire laser system were imaged with a magnification of 2.7 on a Dalsa 1M15 digital camera. A synchronized chopper/shutter combination was used to ensure that single-pulse beam profiles were acquired. The pulse intensity on the camera was reduced to ensure detector linearity by using a a CVI TLM-1-800 laser mirror at normal incidence combined with neutral density filters which were inserted in an expanded section of the beam. Multiple beam profiles were acquired and a representative profile chosen. The Gaussian symmetric and asymmetric beam profiles used in this chapter are shown in Fig. (4.1). The differences between the two profiles of Fig. (4.1) are minor, with the asymmetrical profile containing occasional off-center intensity maxima, though no strong "hot spots". The asymmetric spatial profile includes significantly higher spatial frequencies ($f_{\rm sp}$), in the range $1.7 \times 10^5\,{\rm m}^{-1} < f_{\rm sp} < 8 \times 10^5\,{\rm m}^{-1}$. Both profiles represent pulses of the same average fluence and beam width.

Six of the twelve simulations presented in this chapter use the symmetric Gaussian beam profile while the other six use the asymmetric beam profile. Within each beam profile group of six, two are assigned a total pulse energy of 1 μJ, two a total energy of 0.75 μJ, and two a total energy of 0.5 μJ. The 1 μJ and 0.5 μJ energy groups of two are further divided into single pulse and double-pulse train simulations. The 0.75 μJ simulations in each group of six are temporally asymmetric double-pulse train simulations in which the leading (trailing)

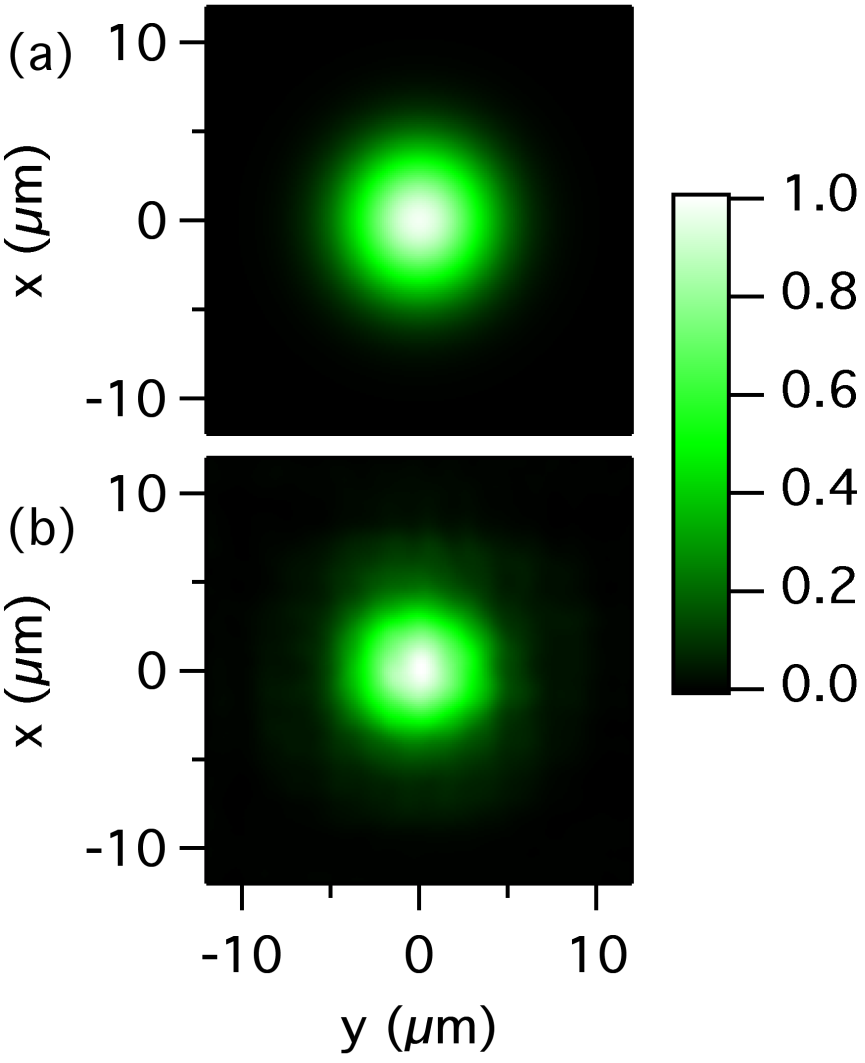

Figure 4.1: Normalized beam profiles, $F(x, y)$, for (a) a cylindrically symmetric Gaussian profile and (b) an experimentally measured beam profile from an amplified Ti:Sapphire laser.

pulse is twice as energetic as the trailing (leading) pulse, respectively. This yields a total of twelve simulations intended to provide insight into the importance of beam geometry, energy and pulse shape in the propagation of ultrashort laser pulses accompanied by plasma formation. All of the above pulses were propagated through 100 μm of fused silica, and the spatial and temporal evolution of both the pulse envelope and the plasma density was recorded.

4.3 Results for Pulse Propagation

4.3.1 Propagation of single pulses and temporally symmetric double pulse trains with a Gaussian spatial beam profile

Space-time (x-τ) intensity profiles at $y = 0$ for a set of four single pulses are shown at four points (0 μm, 10 μm, 50 μm, and 100 μm) along the propagation axis in Fig. (4.2). Figure (4.2a) shows the x-τ profile for a 0.5 μJ pulse. In this case there is some evidence of plasma effects as exemplified by slight absorption and defocusing on the trailing edge of the pulse after propagation through 100 μm of fused silica. By comparison, in Fig. (4.2b) one can observe that for a 1 μJ pulse, absorption in the trailing edge of the pulse is clearly evident after only 10 μm and that by 50 μm there is considerable self-focusing on the leading edge of the pulse as well as significant plasma-induced distortion on the trailing edge.

In Fig. (4.3) the space-time intensity profiles for a set of four double-pulse trains (pulses separated by 500 fs) are shown at two points (0 μm and 100 μm). Figure (4.3a) shows profiles for a double-pulse train with a total energy of 0.5 μJ. As can be seen from the lack of either focusing or defocusing in this figure, self-focusing and diffraction are approximately balanced after propagation through 100 μm of fused silica. This indicates that plasma generation has not produced a free-electron density that is high enough to cause observable optical effects. The space-time intensity profiles for the 1 μJ double-pulse train are shown in Fig. (4.3b). Note that the initial energy of *each* pulse in this figure is the same as the pulse shown in Fig. (4.2a); *i.e.* the first pulse in Fig. (4.3b) at 100 μm is identical to the single-pulse at

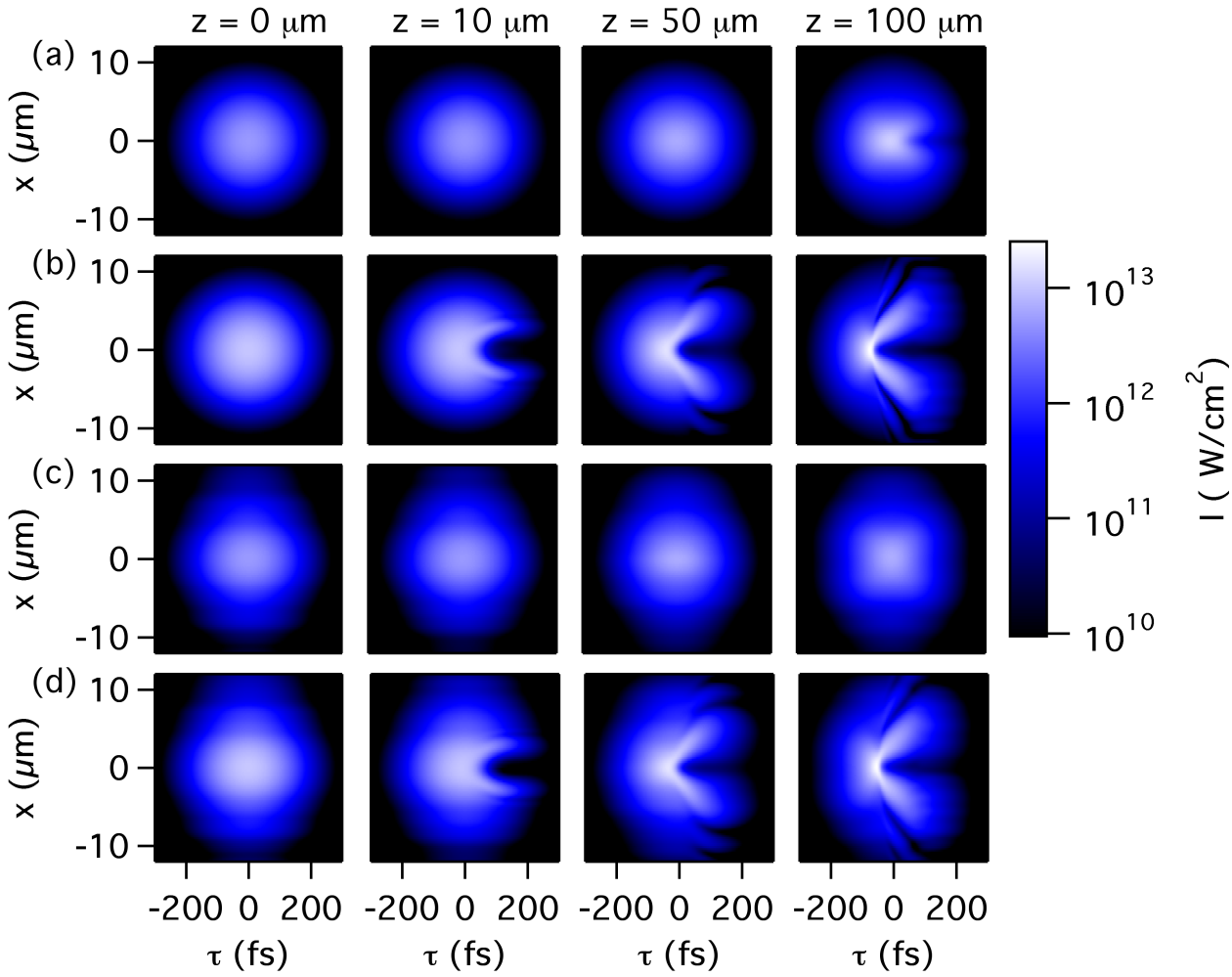

Figure 4.2: Single pulse space-time profiles after propagating 0 μm, 10 μm, 50 μm, and 100 μm through fused silica for a (a) 0.5 μJ symmetric pulse; (b) 1 μJ symmetric pulse; (c) 0.5 μJ noisy asymmetric pulse; (d) 1 μJ noisy asymmetric pulse.

100 μm in Fig. (4.2a). In this case however, the laser-induced plasma now leads to a local intensity minimum at the spatial center of the trailing pulse.

We conclude this section by noting that for all of the simulations presented in this chapter, the full propagation distance (100 μm) corresponds to approximately half the diffraction length for the corresponding Gaussian beam in fused silica. Therefore the effects of linear diffraction in the case of Gaussian beam symmetry are small but observable in the simulations of this chapter.

4.3.2 Propagation of single pulses and temporally symmetric double pulse trains with a spatially asymmetric noisy beam profile

Every symmetric pulse in Fig. (4.2) (a) and (b) and Fig. (4.3) (a) and (b) is compared with its asymmetrical analog Fig. (4.2) (c) and (d) and Fig. (4.3) (c) and (d), respectively. This will begin by contrasting the spatially symmetric 0.5 μJ pulse in Fig. (4.2a) with its spatially noisy asymmetric analog shown in Fig. (4.2c). After 100 μm of propagation, the spatially symmetric pulse shows significant absorption at the trailing edge compared to the assymmetric pulse, while the asymmetric pulse shows increased diffraction. Similarly, comparison of Fig. (4.3a) and Fig. (4.3c) shows clearly that while the symmetric double-pulse train experiences predictably little diffraction, the spatially asymmetric double-pulse train has diffracted significantly after 100 μm of propagation while showing no strong evidence of self-focusing.

For the cases of both symmetric and asymmetric pulses it is interesting to compare propagation of the low energy single pulse cases with the high energy double-pulse cases since the initial energy in each individual pulse is identical, *i.e.* the first pulses in Fig. (4.3) (b) and (d) are identical with pulses shown in Fig. (4.2) (a) and (c). However for the trailing pulses in Fig. (4.3) (b) and (d) there is significant absorption, particularly in the case of the symmetric pulse where there has been absorption at the spatial center of the pulse. These effects are a consequence of the finite lifetime of the free-electron density.

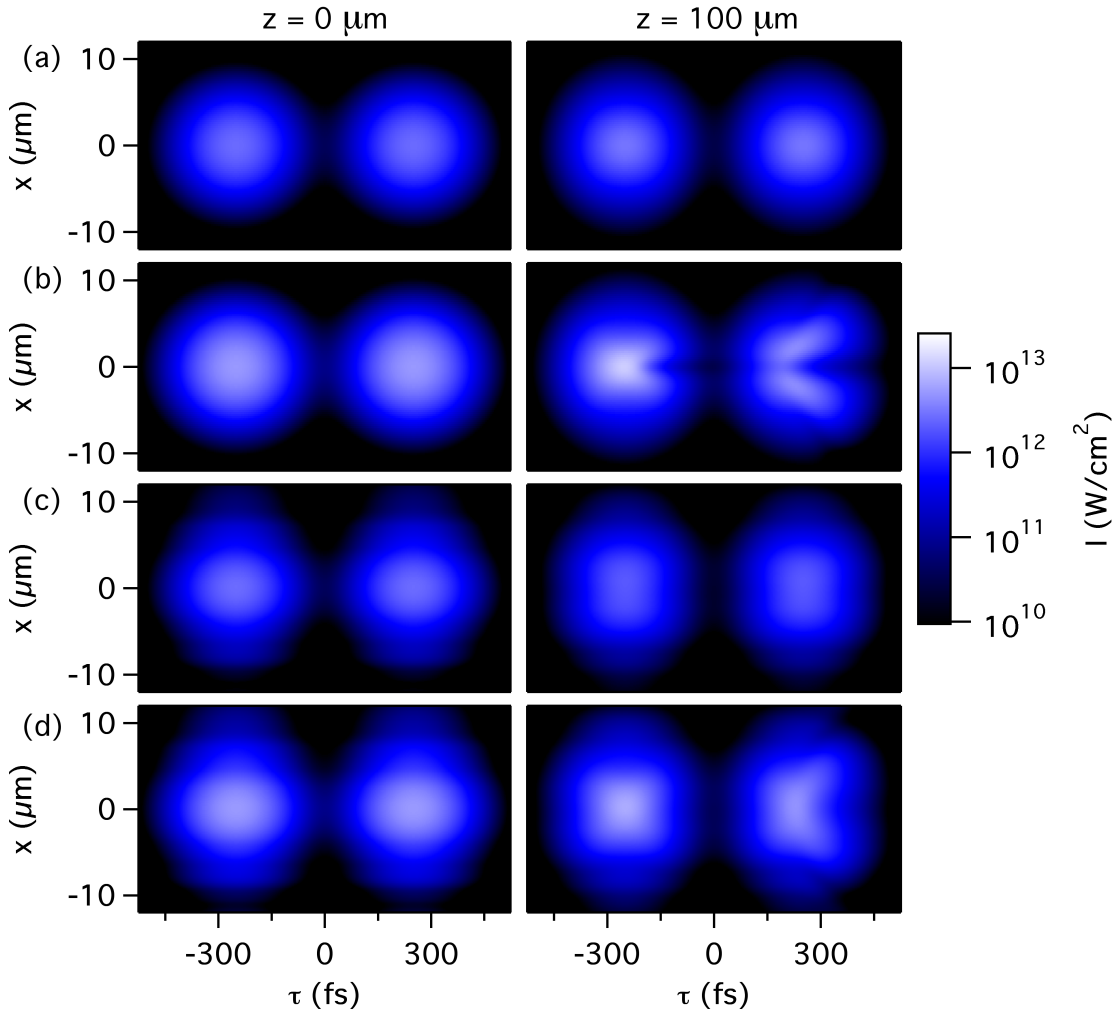

Figure 4.3: Double-pulse train space-time profiles after propagating 0 μm and 100 μm through fused silica for a (a) 0.5 μJ symmetric double-pulse train; (b) 1 μJ symmetric double-pulse train; (c) 0.5 μJ noisy asymmetric double-pulse train; (d) 1 μJ noisy asymmetric double-pulse train.

By comparing the profiles of the two most intense single pulses, Fig. (4.2) (b) and (d), one observes that the mild beam asymmetries, in this case, do not lead to strong differences as these pulses propagate. It is worth noting that for these two simulations the nonlinear effects are (at least initially) the strongest and appear to offset the additional diffraction that results from a noisy beam profile. Furthermore, the interaction of the optical pulse with the free-electron plasma through absorption and defocusing is most clearly seen on the trailing edges of these pulses. Finally, note that for the highest intensity pulses studied in this chapter, the effect of diffraction (even for pulses with high-spatial frequency components) is dominated by nonlinear and plasma effects.

4.3.3 Propagation of temporally asymmetric double pulse trains

The double-pulse trains in Fig. (4.4) are designed to examine the importance of temporal asymmetries in ultrashort pulse propagation. Figure (4.4a) shows a 0.75 μJ cylindrically symmetric train in which the leading pulse has half the energy of the trailing pulse (0.25 μJ and 0.5 μJ, respectively). This temporal configuration will be referred to as a "back-heavy" pulse train. Figure (4.4b) then shows a 0.75 μJ cylindrically symmetric train where the leading pulse has twice the energy of the trailing pulse (0.5 μJ and 0.25 μJ, respectively), and this temporal configuration will be referred to as a "front-heavy" pulse train. Figure (4.4) (c) and (d) have identical temporal configurations to Fig. (4.4) (a) and (b), but have the spatially noisy beam profile of Fig. (4.1b).

Fig. (4.4) (a) and (b) both show evidence of plasma effects on the trailing pulses after 100 μm of propagation. Most notably, the 0.5 μJ trailing pulse in Fig. (4.4a) is nearly identical to the 0.5 μJ leading pulse in Fig. (4.4b) at 100 μm, showing little dependance on the relative temporal position for the high energy pulse. The profiles of the 0.25 μJ pulses at 100 μm in Fig. (4.4) (a) and (b), however, clearly depend on their relative temporal position in the pulse train. Figure (4.4) (c) and (d) show that both the 0.5 μJ and 0.25 μJ pulses in each simulation appear identical to those in the other simulation regardless of their temporal

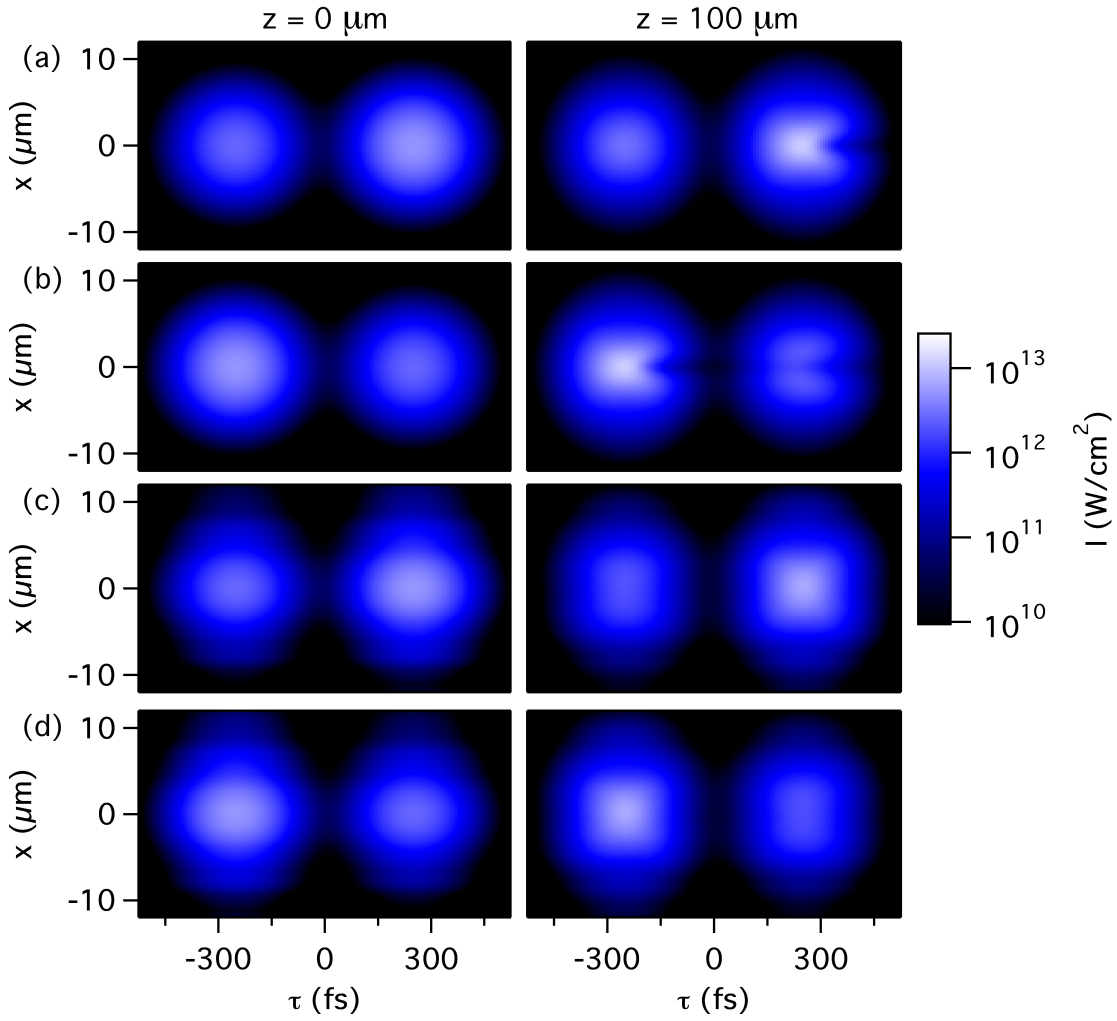

Figure 4.4: Double-pulse train (0.75 μJ) space-time profiles after propagating 0 μm and 100 μm through fused silica for a (a) spatially symmetric "back-heavy" double-pulse train; (b) spatially symmetric "front-heavy" double-pulse train; (c) spatially noisy "back-heavy" double-pulse train; (d) spatially noisy "front-heavy" double-pulse train.

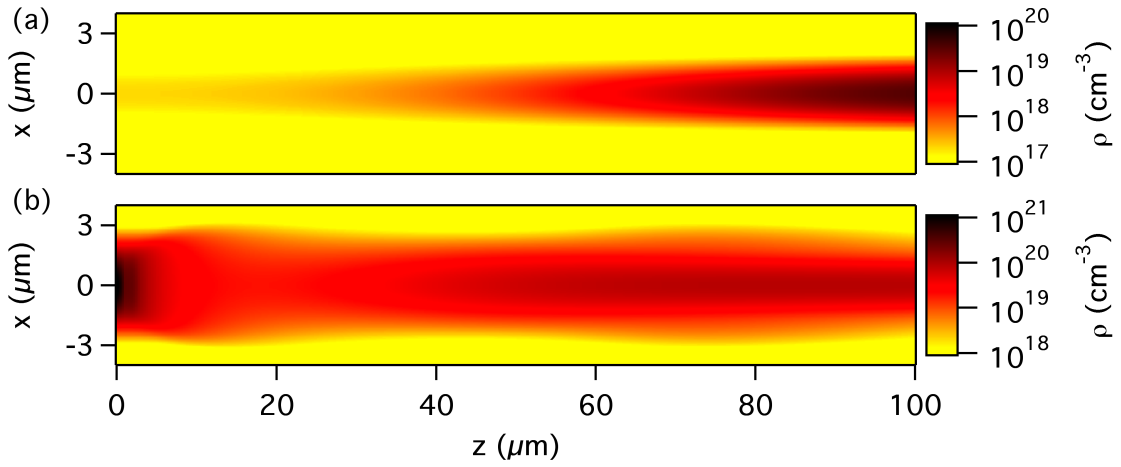

Figure 4.5: Peak plasma densities as a function of position, z, in fused silica in the $y = 0$ plane for a single symmetric pulse with energy (a) 0.5 μJ and (b) 1 μJ.

position in the pulse train. In fact, the pulses in Fig. (4.4) (c) and (d) at 100 μm are quite well predicted by comparison with the leading pulses in Fig. (4.3) (c) and (d). This suggests that noise in the spatial beam profile has a greater influence on ultrashort pulse propagation than the temporal configuration of the double pulse train for the cases under study.

4.4 Results for Plasma Generation

4.4.1 Plasma generation induced by single pulses and temporally symmetric double pulse trains with a Gaussian spatial beam profile

The maximum plasma densities (in the $y = 0$ plane) that are generated in fused silica during the propagation of symmetric single and double-pulse trains are plotted as a function of the propagation distance, z, in Fig. (4.5) and Fig. (4.6), respectively. Note that there is a difference of three orders of magnitude in the peak plasma density between Fig. (4.6) (a)

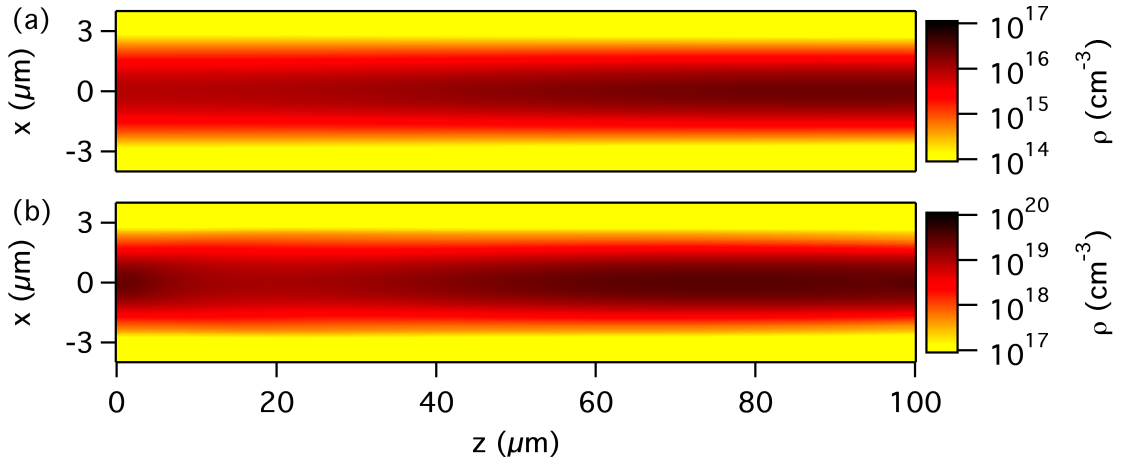

Figure 4.6: Peak plasma densities as a function of position, z, in fused silica in the $y = 0$ plane for a symmetric double-pulse train with total energy (a) 0.5 μJ and (b) 1 μJ.

and (b), despite there being only a factor of two difference in pulse energy, thus exemplifying the importance of the highly nonlinear photoionization process.

It is also interesting to compare the peak plasma densities that result from the propagation of a single 0.5 μJ pulse with that of a pulse train comprising two 0.5 μJ pulses as shown in Fig. (4.5a) and Fig. (4.6b), respectively. In the case of the double-pulse train, the effect of impact ionization is manifested by a peak plasma density that is approximately two orders of magnitude higher than that for a single 0.5 μJ pulse for the first 50 μm of propagation. By comparison, if photoionization were the sole mechanism of plasma generation, the peak plasma densities for these two cases would differ by a factor of approximately two.

Finally, note the significant differences in the structure of the plasma channels generated by single and double-pulse trains; in particular the relative homogeneity of the plasma channel generated by the symmetric double-pulse trains.

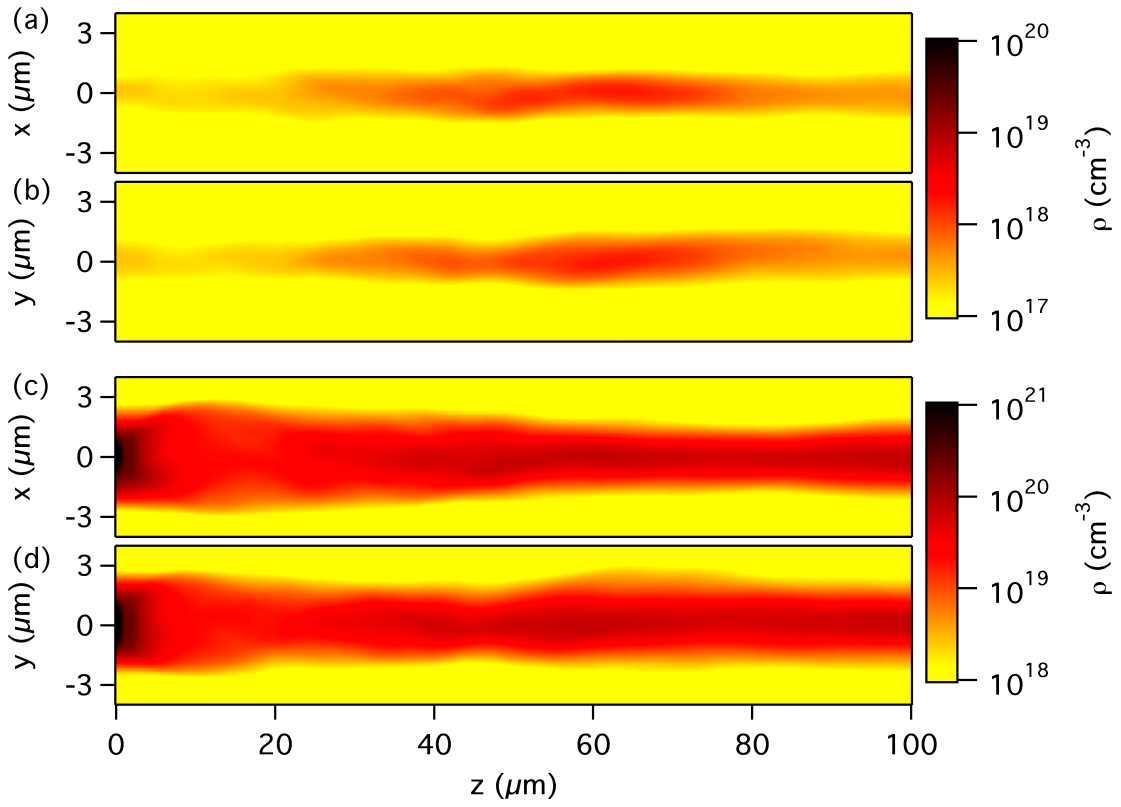

Figure 4.7: Peak plasma density as a function of position, z, in fused silica in the (a) $y = 0$ and (b) $x = 0$ plane for a single noisy asymmetric pulse with energy 0.5 μJ and in the (c) $y = 0$ and (d) $x = 0$ plane for a single noisy asymmetric pulse with energy 1 μJ.

4.4.2 Plasma generation induced by single pulses and temporally symmetric double pulse trains with a spatially asymmetric noisy beam profile

Figure (4.7) and Fig. (4.8) show the peak plasma density plots for the single and double asymmetric pulses, respectively. In these figures, density plots in both the y-z and x-z planes are shown in order to illustrate the asymmetry in the plasma density. Note that all of the peak plasma density plots resulting from asymmetric pulse propagation differ considerably from their cylindrically symmetric analogs, much more than might be expected from the intensity

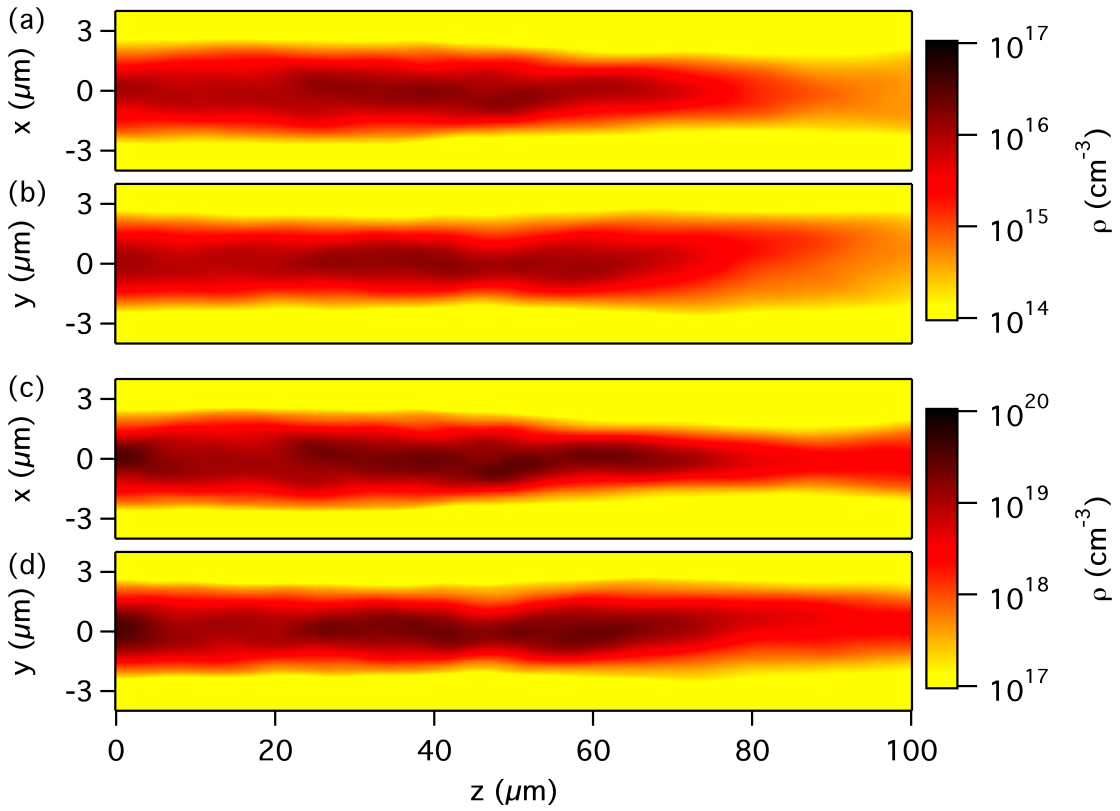

Figure 4.8: Peak plasma density as a function of position, z, in fused silica in the (a) $y = 0$ and (b) $x = 0$ plane for an asymmetric double-pulse train with energy 0.5 μJ and in the (c) $y = 0$ and (d) $x = 0$ plane for an asymmetric double-pulse train with energy 1 μJ.

plots shown in Fig. (4.2) and Fig. (4.3). The author posits that this is results from small intensity variations present in the asymmetrical pulses having a major influence on plasma generation due to the highly nonlinear photoionization step; this combined with enhanced diffraction due to high spatial frequency components causes the noisy asymmetric pulses to create plasma channels with a more complex structure than their cylindrically symmetric counterparts.

It is notable that the peak plasma densities resulting from propagation of the most intense symmetric pulse (Fig. (4.5 b)) and asymmetric pulse (Fig. (4.7) (c) and (d)) exhibit the smallest structural differences as a result of differences in beam symmetries than their lower intensity analogs, as was also the case with the intensity profiles depicted in Fig. (4.2) (c) and (d). This behavior is likely a consequence of the geometry of the simulations, *i.e.* the laser pulse is focused directly on the material surface. In this case nonlinear and plasma effects excise the diffraction for the 1 μJ asymmetric single pulse. In contrast, for the case of pulses that are intentionally focused within the bulk of the material rather than at the surface, the author expects that mild beam asymmetries may lead to increased diffraction prior to plasma generation, causing the pulse evolution to deviate significantly from that of its cylindrically symmetric analog even for pulses with peak power well above the critical power. A detailed investigation of this case will be the subject of a future study.

4.4.3 Plasma generation induced by temporally asymmetric double pulse trains

The maximum plasma densities (in the $y = 0$ plane) that are generated in fused silica during the propagation of spatially symmetric but temporally asymmetric double-pulse trains are plotted as a function of the propagation distance, z, in Fig. (4.9). The results from the "back-heavy" pulse train configuration shown in Fig. (4.9a) are strongly similar to the "front-heavy" results in Fig. (4.9b). However, a careful comparison between the two reveals that the "back-heavy" configuration yields slightly higher peak plasma densities throughout the

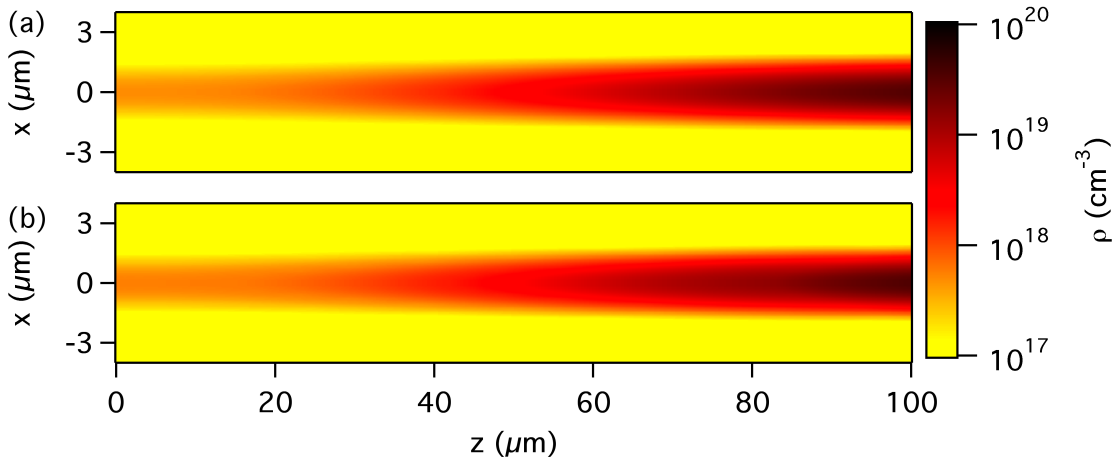

Figure 4.9: Peak plasma densities as a function of position, z, in fused silica in the $y = 0$ plane for a 0.75 μJ double-pulse train with a (a) "back-heavy" pulse and (b) "front-heavy" pulse.

propagation. This is likely due to the fact that impact ionization resulting from the high energy pulses will be greater in the case of a trailing high energy pulse, as it will inherit previously generated seed electrons from the leading lower energy pulse.

The maximum plasma densities generated by propagation of spatially noisy, temporally asymmetric double-pulse trains in Fig. (4.10) show, again, only minor differences between the temporal symmetry configurations. A comparison of the peak plasma densities in Fig. (4.10) with those of Fig. (4.9) reveals that the differences resulting from the chosen temporal asymmetries are almost negligible when compared to those resulting from noisy beam symmetry. In fact, during the last 30 μm of propagation, the peak densities in Fig. (4.9) are an entire order of magnitude greater than those of Fig. (4.10). Again this suggests that noise in the spatial beam profile has a greater influence on plasma generation than the temporal configuration of the double pulse train for the cases under study.

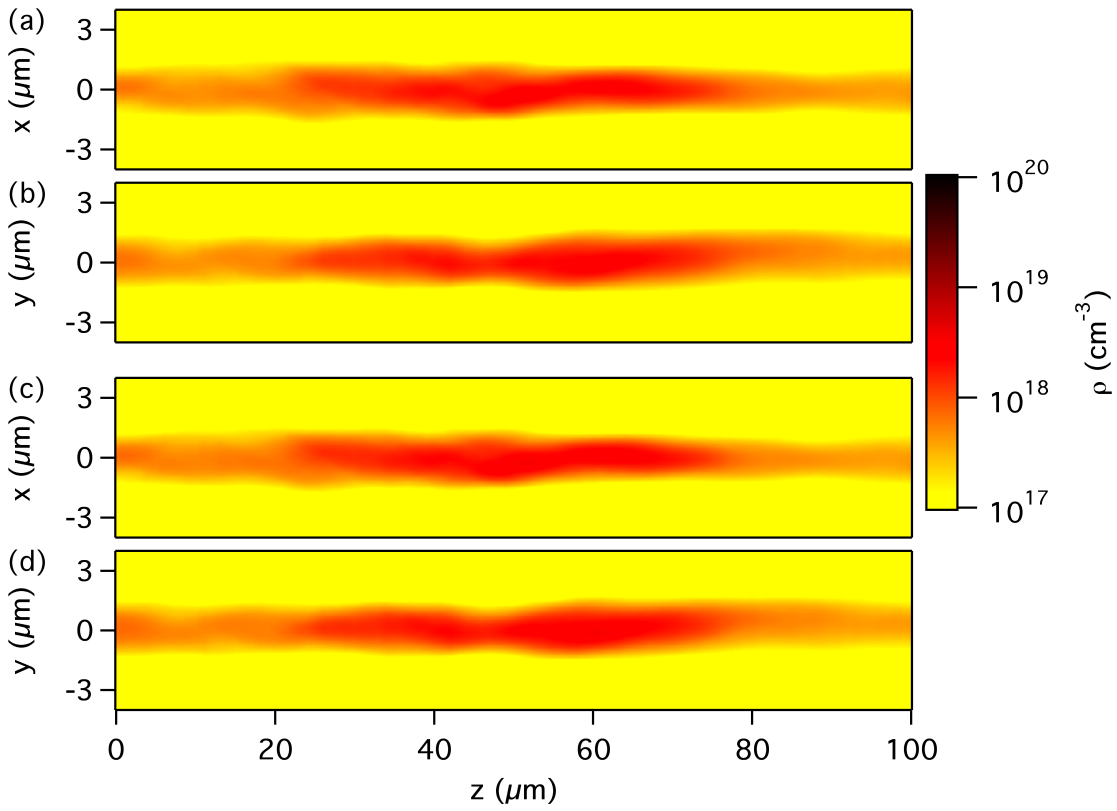

Figure 4.10: Peak plasma density as a function of position, z, in fused silica for spatially asymmetric 0.75 μJ double-pulse trains in the (a) $y = 0$ and (b) $x = 0$ plane for a "back-heavy" train and in the (c) $y = 0$ and (d) $x = 0$ plane for a "front-heavy" train.

4.5 Discussion

Many of the results of this chapter are summarized in Fig. (4.11) and Fig. (4.12), which allow for a direct comparison of peak pulse intensity with the peak plasma density for each simulation as a function of the propagation distance. In both of these figures, results from simulations with single pulses and temporally symmetric pulse trains are shown in black while results from simulations with temporally asymmetric pulse trains are shown in gray. Figure (4.11a) and Fig. (4.12a) show results from spatially symmetric simulations while Fig. (4.11b) and Fig. (4.12b) show the results of spatially noisy simulations.

We note that in every simulation with an asymmetric spatial beam profile, Fig. (4.12) shows considerable variability in the peak density values when compared to their relatively smooth symmetric counterparts. As indicated previously, this variability results from small spatial fluctuations in intensity present in the noisy spatially asymmetric pulses. Also, for every simulation with an asymmetric spatial beam profile there appears to be a drop in the peak intensity in the range $50-65$ μm. This drop is again caused by enhanced diffraction due to high spatial frequency components overcoming nonlinear processes and spreading the spatial profile. This comparatively sudden drop in intensity lowers the production of free electrons and is mirrored by a corresponding decline in peak plasma density as shown in Fig. (4.12).

Figure (4.11) reveals that the 0.75 μJ and 1 μJ double-pulse trains have the same peak intensities as the single 0.5 μJ pulses, *i.e.* for the 1 μJ double-pulse case the intensity peaks in the leading pulse. This is significant in that, for spatially symmetric pulses, Fig. (4.12) shows that propagation of a single 0.5 μJ pulse and the 1 μJ double-pulse train lead to the same peak plasma density after 100 μm of propagation in fused silica indicating that at these pulse energies, plasma generation predominantly occurs during the first pulse at 100 μm. By contrast for the asymmetric 1 μJ double-pulse train the peak plasma density occurs during the trailing pulse. Meanwhile, both the intensities and peak plasma densities of the spatially noisy, temporally asymmetric pulse trains, track with those of the single 0.5 μJ pulse after

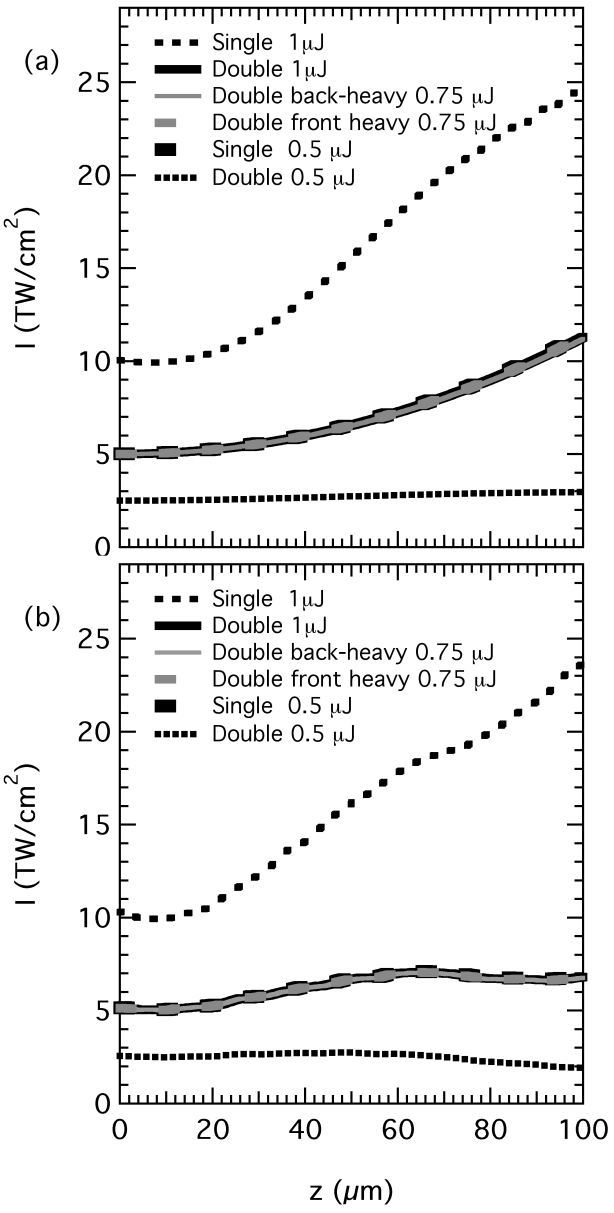

Figure 4.11: Peak intensity as a function of position, z, in fused silica for (a) each spatially symmetric simulation and (b) each spatially noisy asymmetric simulation reported in this chapter. Results from temporally symmetric simulations are shown in black; results from temporally asymmetric simulations are in gray.

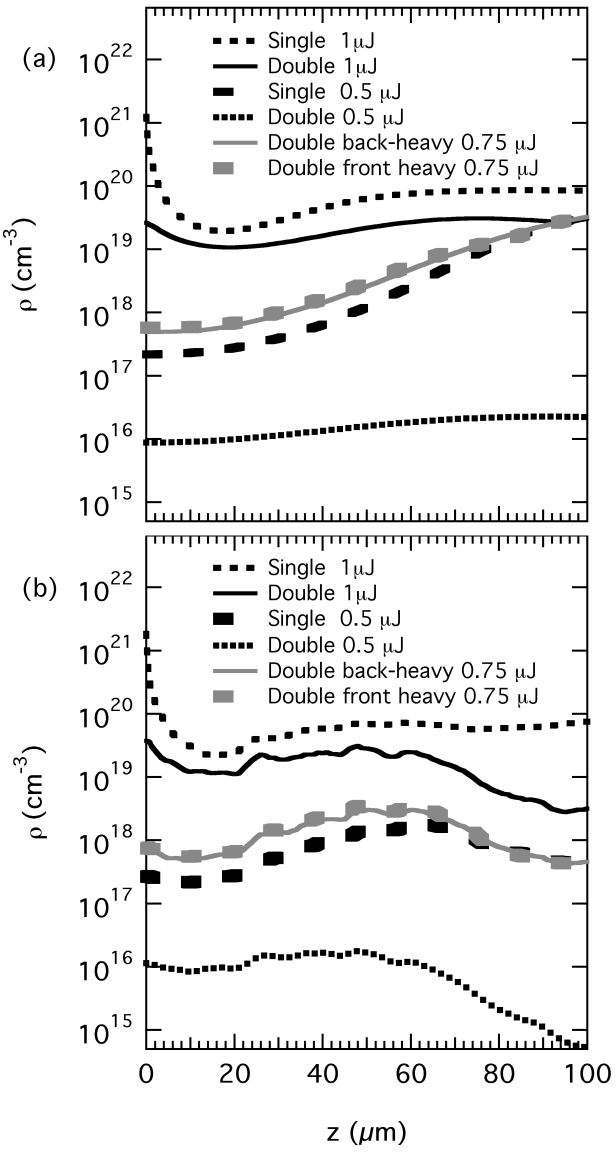

Figure 4.12: Peak plasma density as a function of position, z, in fused silica for (a) each spatially symmetric simulation and (b) each spatially noisy asymmetric simulation reported in this chapter. Results from temporally symmetric simulations are shown in black; results from temporally asymmetric simulations are in gray.

~ 75 μm. This indicates that the companion 0.25 μJ pulse has ceased to play a significant role regardless of the temporal configuration.

4.6 Concluding Remarks

Simulations of ultrashort pulse propagation and plasma generation near to the damage threshold have been performed for 100 μm of fused silica. In particular, fully 3+1D simulations were performed for the cases of single pulses and (both temporally symmetric and asymmetric) double pulse trains with both Gaussian and noisy spatially asymmetric beam profiles. For the cases of overlapping validity, the results from these simulations are in good agreement with 2+1D simulations of other authors [14; 19]. Temporal asymmetries in double pulse trains were found to play a much smaller role than spatial asymmetries for the cases under study. It is notable that a comparison of the single symmetric and noisy asymmetric pulse propagation results often reveals only small differences in the space-time intensity and spatial fluence profiles. However for the cases of spatially noisy asymmetric pulses, the plasma density in the material exhibits a significantly different structure than their spatially symmetric counterparts. The author attributes this behavior to the transformation of small spatial variations in the intensity into large variations in the plasma density due to (i) the highly nonlinear photoionization step and (ii) to increased diffraction. Such variations in plasma density may present a problem for researchers who wish to use ultrashort pulses to precisely modify the optical properties of dielectric materials; as a consequence, future simulations will focus on a more detailed exploration of plasma generation and laser damage caused by "realistic" ultrashort pulses.

Chapter 5

Models of Free-Carrier Dynamics and the Modified Nonlinear Schrödinger Equation

In Chapters 3 and 4, simulations of ultrashort pulse propagation in fused silica were performed while modeling the material dynamics with classical rate equations for the plasma density of free electrons. In this chapter, results from fully 3+1D pulse propagation simulations using pulses constructed from experimental data are presented and compared with corresponding experimental results. This study is the first of its kind in that it uses experimental data as a template for both the beam structure and pulse shape of the laser field in the simulations. It is also the first study, to the author's knowledge, to interface the multi-rate equation model for plasma dynamics (developed by Rethfeld) with a fully 3+1D modified NLSE simulation. Several successes of this study include an improved prediction of the laser-induced damage threshold for the conditions under consideration as well as the correct prediction of post-experimental beam structure in many cases.

However, some discrepancies between the experimental and computational data suggest that plasma dynamics in the material are not being modeled properly for laser pulse energies near the threshold of optical damage. Therefore, in this chapter the multi-rate equation model of Rethfeld [11] is compared to the Fokker-Planck equation (FPE) description of plasma dynamics [41] in a continuous energy space. Results solving the multi-rate equation model are compared to the solutions of the more detailed FPE model for illustrative 1D pulse-material interactions. It is noted that the FPE must be modified, just as the NLSE was modified, to account for ultrashort dispersion corrections to free-carrier absorption predicted by the modified NLSE derived in Chapter 3. This issue has not been addressed in the published

literature for any model of plasma dynamics, FPE or otherwise. It is further noted that in order to account for shifts in the instantaneous optical frequency of an ultrashort laser pulse, *i.e.* shifts in the average energy per photon as a function of space and time, the calculation of the photoionization rate must be evaluated with this non-constant value both for pulse propagation and plasma evolution models. Finally, the benefits and challenges of performing fully 3+1D pulse propagation simulations by simultaneously solving the modified NLSE with a modified FPE are discussed.

5.1 A Computational Dilemma

The modeling of free-electron behavior in semiconductors and wide band gap dielectrics is fundamentally a problem of non-equilibrium statistical mechanics [35]. In materials science, free-carrier dynamics are commonly modeled by a Boltzmann transport equation [40], a Fokker-Planck equation [36; 41], or energy and momentum balance equations [37; 38]. These methods use a mix of classical, quantum mechanical, and solid state physics, with varying degrees of phenomenological approximations [35; 44]. They also present formidable computational challenges inherent to solving systems of partial differential equations and integro-partial differential equations [59]. For this reason, simulations in computational optics (such as those in Chapters 3 and 4) usually model this behavior with a phenomenological rate equation for a particular population of free carriers [12], or a discrete set of particle populations [55]. However, recent collaborative work by Winkler [60] and the author suggests that a more detailed, partial differential equation (PDE) description of plasma dynamics may be required to accurately describe fully 3+1D pulse propagation through dielectric materials.

5.1.1 Comparing Experiment with Simulation

Due to the ubiquitous approximation of cylindrical beam symmetry and the use of a single phenomenological rate equation for the modeling of plasma dynamics, simulations in nonlinear optics and laser-induced damage are frequently used for qualitative, rather than quan-

titative comparisons with experimental data. For example, modified NLSE simulations that use the single-rate equation approach for calculating plasma dynamics often underestimate laser-induced damage threshold pulse energies by a factor of two or greater [14; 92]. In subsequent simulations reported in the literature, this considerable discrepancy is usually removed with one of two methods. The first method is to tune laser pulse parameters in the simulation (such as pulse energy or beam width) away from their experimentally measured values so that optical damage is predicted (see for example Ref. [14]), and using the results to make qualitative comparisons with experiment. The second method is to tune material parameters in the simulation (such as the Drude collision time or the effective electron mass) away from experimentally measured values so that the simulation results (such as an optical damage threshold or energy transmission measurement) match best with experiment. In Refs. [46] and [52], Drude collision times of 20 fs and 23 fs are chosen for simulations in fused silica so as to match the experimental results reported in these papers, despite the fact that most laboratory measurements of the Drude collision time for fused silica are on the order of 1 fs or less [75–77]. Ideally, if one forgoes the approximation of cylindrical beam symmetry (and that of an analytic pulse shape) in favor of a fully 3+1D laser pulse numerically constructed from laboratory measured data, then the method of tuning pulse parameters in the simulation should become unnecessary. Concurrently, if one uses a more accurate model of plasma dynamics (such as Rethfeld's multi-rate equation model [11] instead of Stuart's single-rate equation model [12] for electrons in the conduction band), then the method of tuning material parameters in the simulation away from experimentally measured values should become unnecessary. A structured test of these hypotheses formed the basis of a collaborative work between Winkler and the author [60].

A full description of this collaborative work is found in the Ph.D. dissertation of Winkler [60], but the experimental aspects can be summarized as follows. A 1 μJ ultrashort laser pulse from an amplified Ti:Sapphire laser system, with center wavelength of 800 nm, is characterized in the laboratory with a measurement of the beam profile and a FROG

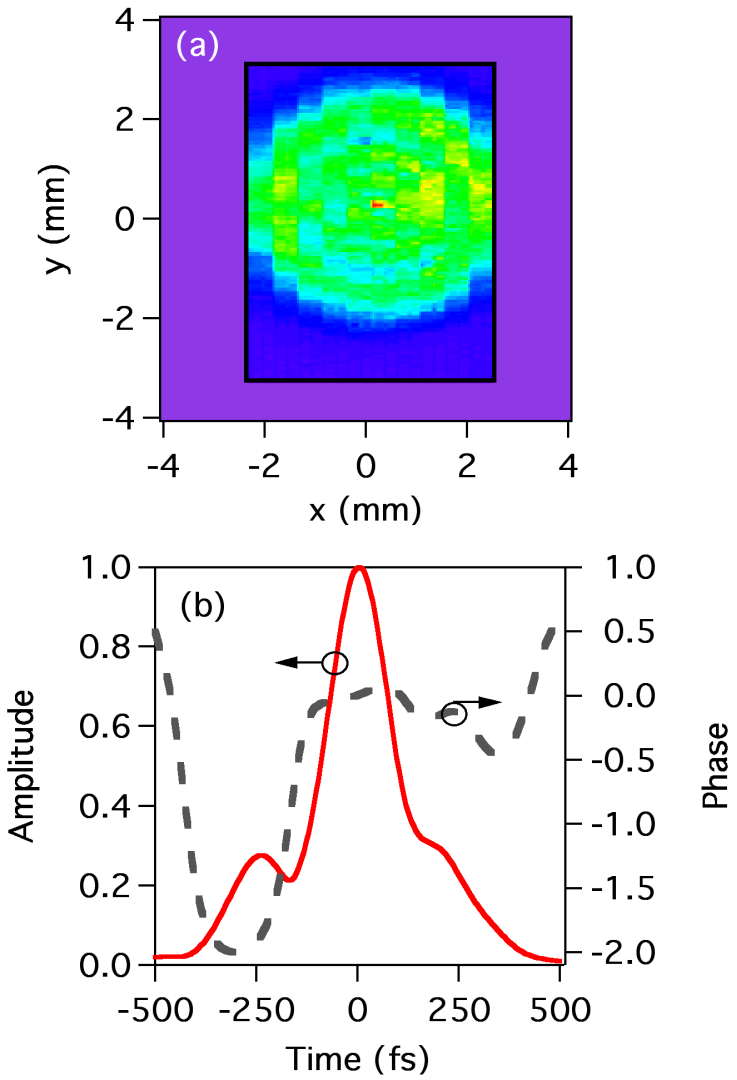

Figure 5.1: Initial spatio-temporal characterization of the laser pulse in Winkler's experiment: (a) the normalized beam profile, and (b) the normalized amplitude (solid) and temporal phase (dashed) retrieved from a FROG trace. Taken from Ref. [60].

(Frequency-Resolved Optical Gating [13]) trace, from which the pulse shape and temporal phase information is retrieved, see Fig. (5.1). Laser pulses of incrementally increasing energies were then propagated through a 25 cm focal length lens and focused onto a 200 μm thick sample of fused silica glass. The energy of these pulses ranged from 1 μJ to 80 μJ, with pulsewidths of 135 fs and a focused FWHM beam width of 25 μm. Laser-induced damage to the fused silica sample was observed at pulse energies of 60 μJ and higher. After exiting the sample the pulses propagated 25 cm in air and were recollimated with another 25 cm focal length lens. Final beam profiles were then measured and final FROG traces were taken. However, the pulse shape and temporal phase information for the pulses near or above the damage threshold of 60 μJ was not retrievable from the final FROG traces due to large spatio-temporal dependencies in the pulse (see Sec. 3.4 in [60] for a detailed discussion of this issue).

For the purpose of comparison with the experimental results, simulations developed by the author were performed using the initial laser pulse conditions shown in Fig. (5.1). Note that the beam profile in Fig. (5.1a) has been clipped (*i.e.* not measured) on the edges. To compensate for this lack of information in the experimental measurement, the beam profile in Fig. (5.1a) was numerically extrapolated on the wings and the edges were smoothed by application of a fourth-order "super-Gaussian" soft aperture with a diameter equal to the width of the laboratory beam profiler. This smoothed beam profile was numerically focused using a Fourier transform method [23; 60] to account for a 25 cm focal length lens. The resulting beam profile at the geometric focus was combined with the retrieved temporal field amplitude and phase information from Fig. (5.1b) to numerically construct a laser pulse electric field envelope for each of the given laboratory pulse energies.

Pulse propagation through the fused silica sample was simulated by solving Eq. (3.16) simultaneously with the multi-rate equation model for plasma generation developed by Rethfeld [11]. The material parameters used for this simulation are found in Table 4.2, with the exception of the collision time which was varied from 1 fs to 15 fs. After exiting the fused

silica sample, pulse propagation through 25 cm of air to the second 25 cm focal length lens was simulated, again using a Fourier transform technique [23; 60], where the beam was recollimated and the final beam profiles were numerically calculated. Figure (5.2) shows a comparison of the experimentally measured (left column) and numerically predicted (right column) final beam profiles for pulses with initial energies of 1 μJ, 10 μJ, 50 μJ, and 80 μJ.

The simulations correctly predict the experimentally measured damage threshold pulse energy of 60 μJ only when using a Drude collision time of 4 fs, a significant improvement when compared to the much longer collision times chosen in the other authors' simulations [46; 64; 69; 70] so as to match their experiments. However, 4 fs is still significantly larger than the experimentally measured collision times on the order of 1 fs or less [75–77]. Simulations performed by Winkler and the author, using a collision time of 1 fs, predicted a reduced optical damage threshold energy of 30 μJ, contradicting the laboratory measurement of this value by a factor of two. Comparison of the final beam profiles from experiment and simulation in Fig. (5.2) similarly reveal minor improvements in prediction of beam structure, but also display irreconcilable discrepancies for energies near and above the damage threshold.

For the pulse energies of 1 μJ and 10 μJ, Fig. (5.2) shows good agreement between the beam profiles of experiment and simulation. For these pulse energies, spatially localized "hot spots" on the wings and offset from the center of the beam are predicted by the simulations, information that would not be available from calculations assuming cylindrical beam symmetry. For the 50 μJ and 80 μJ pulses, localized "hot spots" on the wings of the beam are predicted with comparatively good accuracy. However, these higher energy pulse simulations predict the presence of intensity maxima in the center of the beams which are wholly absent from the corresponding experimental measurements. Further, these discrepancies in the beam centers were predicted by the simulations using a Drude collision time of 4 fs (the collision time that predicted the laboratory measured damage threshold pulse energy) as well as for those that used the collision time of 10 fs, the results of which are shown in Fig. (5.2). Thus, for the results presented in this section, the two standard methods of reconciling simulation

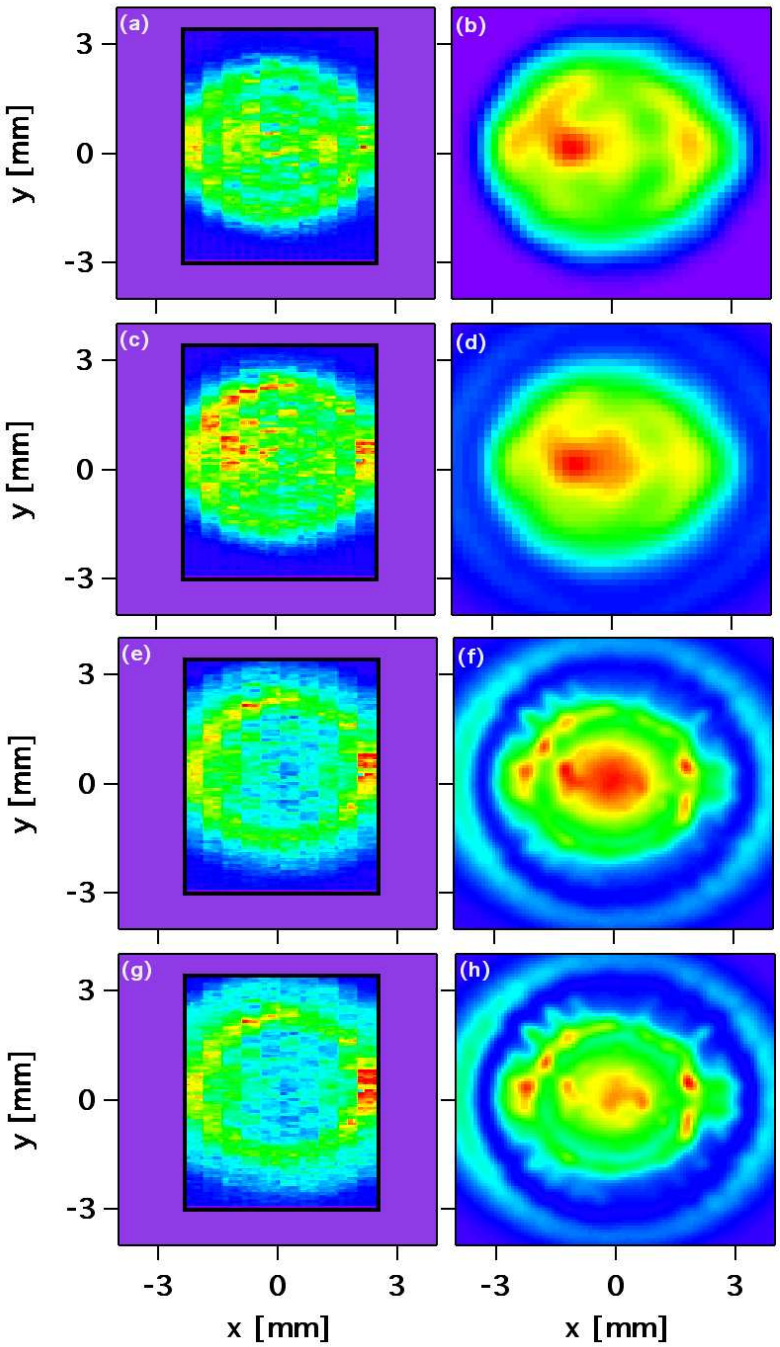

Figure 5.2: Final normalized beam profiles for the 1 μJ experiment (a) and simulation (b), the 10 μJ experiment (c) and simulation (d), the 50 μJ experiment (e) and simulation (f), and the 80 μJ experiment (g) and simulation (h). The color scale, from zero to the peak, ranges blue-green-yellow-red, respectively. The black outlined boxes that appear in the left column indicate the edges of the laboratory beam-profiler device. Simulations used a collision time of 10 fs. Taken from Ref. [60].

with experiment (adjusting pulse parameters or adjusting the Drude collision time) becomes superfluous in the first case and unhelpful in the second.

5.1.2 Interpretation of Results

Assuming the correctness of both experimental and computational procedures (the author recognizes that this is not a trivial assumption), the results of this study suggest, at a minimum, one of several troubling possibilities: 1) the modified NLSE does not correctly model the pulse evolution under the assumed conditions, 2) the numerically constructed form of the electric field was not representative of the true electric field, or 3) the multi-rate equation model of plasma dynamics did not adequately describe the behavior of the material. The first of these possibilities appears, to the author, to be the least probable. The fundamental limitations of the modified NLSE derived in Chapter 3 were laid out in precise detail in 1997 by Brabec and Krausz [31]. During the study presented in this section, Winkler and the author took care to ensure that the limitations imposed by this equation were not exceeded in the simulations or in the experiments.

The second of these possibilities, that the electric field was not properly represented in the simulations, must be considered as less probable an explanation than it otherwise would have been if a cylindrical beam symmetry or an analytic pulse shape had been assumed, which is currently the standard in the field of computational nonlinear optics. Nevertheless, there remain several possible sources of error in numerically constructing the electric field envelope. The initial beam profile in Fig. (5.1a), having been clipped on the edges during the experimental measurement, may not have been adequately represented by extrapolating and smoothing process as formerly described. Additionally, the assignment of the retrieved pulse shape and temporal phase from Fig. (5.1b) assumes that the temporal dependence of the initial complex field envelope does not change as a function of its relative position in the laser beam. The likelihood of either of these possibilities is considerably diminished by the fact that the low energy beam profiles in Figs. (5.2a,b) and Figs. (5.2c,d) are in comparatively

good agreement. In fact, to the author's knowledge, no study has been published to date where a fully 3+1D laser pulse is constructed from the combined information of a laboratory measured beam profile and a FROG trace, making the results presented in this section among the most of accurate of their kind with regard to the characterization of the initial electric field.

The most probable source of error is therefore the chosen model for the plasma dynamics, for which several more detailed models exists. This conclusion is further supported by the fact that the low energy beam profiles in Figs. (5.2a,b) and Figs. (5.2c,d) agree relatively well, as comparatively little plasma generation occurs at the lower pulse energies. The higher energy pulses in Figs. (5.2e,f) and Figs. (5.2g,h) approach or exceed the damage threshold, where plasma dynamics most strongly influence the pulse propagation, and it is in this regime where major discrepancies are found in the final beam profiles. If discrepancies between experiment and simulation presented in this section are in any way attributable to misrepresenting the form of the electric field in the simulations, then this error is correctable with more detailed experimental characterizations of the initial laser pulse. However, if the error is attributable to an inadequate model for the plasma dynamics, then the results of this section suggest that many of the simulations of computational nonlinear optics that aspire to model the interactions of laser-induced damage may be misleading. In this case the burden of resolving discrepancies between experiment and simulation lies plainly with the developer (and user) of the simulations.

The simulations presented in this section employed Rethfeld's multi-rate equation [11] to model the plasma dynamics. In short, the model describes a "ladder" of k discrete free-carrier populations, $n_j(\vec{x},t)$ $(j = 0...k)$, in the energy space ϵ of the conduction band, separated by integer multiples of the photon energy $\hbar\omega_0$. The individual populations may be summed to determine the total free-carrier density $\rho(\vec{x},t) = \sum_{j=0}^{k} n_j(\vec{x},t)$. Combined with contributions of the Keldysh photoionization rate W_{PI} given by Eq. (3.20) and the electron-hole

recombination term, the multi-rate equation takes the form:

$$\begin{aligned} \partial_t n_0 &= W_{\mathrm{PI}} + 2\,\alpha_{\mathrm{imp}}\,n_k - W_{1\mathrm{pt}}\,n_0 - n_0/\tau_r \\ \partial_t n_j &= W_{1\mathrm{pt}}\,n_{j-1} - W_{1\mathrm{pt}}\,n_j - n_j/\tau_r \\ \partial_t n_k &= W_{1\mathrm{pt}}\,n_{k-1} - \alpha_{\mathrm{imp}}\,n_k - n_k/\tau_r \end{aligned} \tag{5.1}$$

where n_1 represents the first level on the energy ladder $\epsilon = 0$, n_j represents the j^{th} energy level $j\hbar\omega_0$, n_k represents the final energy level $\epsilon = k\hbar\omega_0$. The integer k is calculated by $k = \langle \epsilon_{\mathrm{crit}}/\hbar\omega_0 + 1 \rangle$, where $\langle\rangle$ denotes the integer part of the enclosed quantity,

$$\epsilon_{\mathrm{crit}} = \frac{m + 2m_v}{m + m_v}\left(U_0 + \frac{e_0^2\,|\xi|^2}{4m\omega_0^2}\right) \tag{5.2}$$

is the critical energy for impact ionization, m is the effective mass of the conduction band electron, and m_v is the effective mass of the valence band electron. The rate of single photon absorption is given by $W_{1\mathrm{pt}} = \sigma I(t)$ in accordance with the Drude theory of conductivity. The impact ionization rate α_{imp} is taken to be instantaneous. A visual description of the plasma evolution predicted by the multi-rate equation is given in Fig. (5.1.2) (taken from Ref. [11]) where *CB* and *VB* stand for conduction band and valence band, respectively. This model was developed so as to provide a significant improvement over Stuart's single-rate equation model for electrons in the conduction band (the model that was used in Chapters 3 and 4). It accounts for the fact that a newly freed electron will not, even at high optical intensities, become immediately capable of impact ionization, but must drift up the ladder to the critical energy.

Although the superiority of the Rethfeld's multi-rate equation model to Stuart's single-rate equation model is not disputed in the literature, the single-rate equation model remains the preference of most computational optics researchers [8; 9; 14; 19; 20; 27; 46; 52–54; 64; 68–72; 74; 78; 89]; perhaps due to the multi-rate equation's increased computational complexity. However, the results presented in this section indicate that even the multi-rate equation model may not provide an adequate description of plasma dynamics for ultrashort laser pulses near the threshold of optical damage. Fortunately, there exist several more detailed

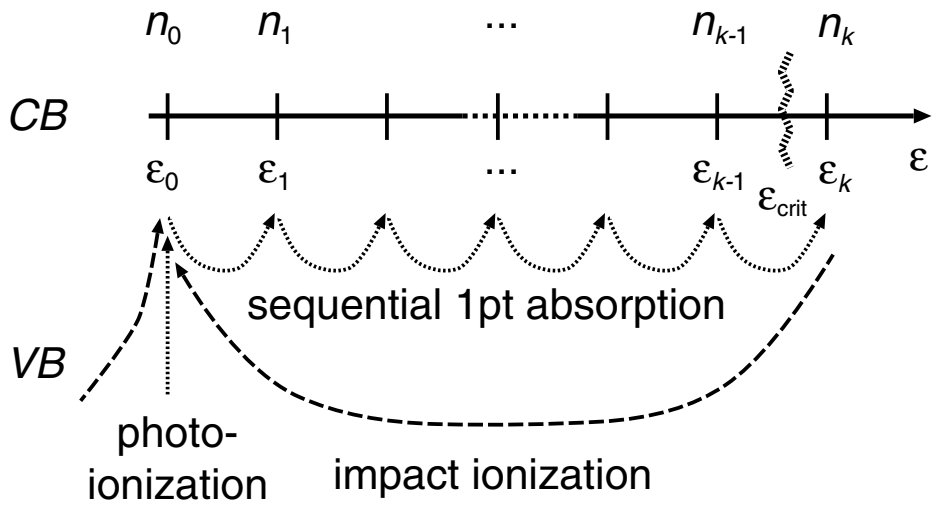

Figure 5.3: A schematic of the avalanching process as modeled by Eq. (5.1). Taken from Ref. [11].

descriptions of this behavior in the form of partial differential equation models, the most common of which are the Boltzmann equation and the Fokker-Planck equation [12; 40]. These PDE descriptions of plasma effects are briefly introduced the next section.

5.2 Partial Differential Equation Models of Plasma Dynamics

5.2.1 The Boltzmann Equation

The Boltzmann transport equation is a semi-classical integro-differential equation which can be used to model the dynamics of condensed matter on the microscopic level [93]. In principle, it describes the time evolution of a distribution function $b(\vec{x}, \vec{k}, t)$ in phase space. In its full form, the Boltzmann equation is expressed [35]:

$$\frac{\partial b}{\partial t} + \frac{\vec{F}_{\text{ext}}}{\hbar} \cdot \vec{\nabla}_k \, b + \frac{\hbar \vec{k}}{m} \cdot \vec{\nabla}_x \, b = \left(\frac{\partial b}{\partial t} \right)_{\text{scattering}} \tag{5.3}$$

where $\vec{F}_{\text{ext}}$ is the total external force, $\vec{k}$ is the wave vector, and the term on the right-hand side consists of quantum mechanical collision integrals describing all the relevant scattering processes. In practice, authors simulating ultrashort pulse-material interactions typically neglect the spatial diffusion term on the right-hand side [37; 40; 93], $\vec{\nabla}_x b = 0$, which is consistent with the assumption of an electrically neutral material. Additionally, authors investigating the material dynamics under the influence of an AC electric field are typically interested in the time-averaged quantities of Eq. (5.3) [37; 40; 93]. Under this condition, if the only external force acting on a particle comes from the A.C. field then the momentum gradient term on the left-hand side of Eq. (5.3) averages to zero [37] and the equation then reads:

$$\frac{\partial b}{\partial t} = \left(\frac{\partial b}{\partial t}\right)_{\text{scattering}} \tag{5.4}$$

and is frequently called "the Boltzmann Equation" in the literature [37; 40; 44; 93].

Although the Eq. (5.4) allows for the inclusion of an arbitrary number of scattering processes, in the case of free-electron dynamics these processes typically include electron-electron interactions (e-e), electron-phonon interactions (e-pn), phonon-assisted photon absorption (e-pn-pt) which is the microscopic analog of laser energy absorption by free carriers, photoionization (pi), and impact ionization (imp). Further, the inclusion of microscopic phonon effects necessitates the solving of additional Boltzmann equations for the various optical and acoustic phonon modes ($s_\beta(\vec{x}, \vec{k}, t)$ where β indicates the phonon mode) that make significant contributions to the plasma dynamics. Phonon-phonon interactions are usually neglected [40]. The resulting set of coupled Boltzmann equations are:

$$\frac{\partial b}{\partial t} = \left(\frac{\partial b}{\partial t}\right)_{\text{e-e}} + \left(\frac{\partial b}{\partial t}\right)_{\text{e-pn}} + \left(\frac{\partial b}{\partial t}\right)_{\text{e-pn-pt}} + \left(\frac{\partial b}{\partial t}\right)_{\text{pi}} + \left(\frac{\partial b}{\partial t}\right)_{\text{imp}} \tag{5.5}$$

$$\frac{\partial s_\beta}{\partial t} = \left(\frac{\partial s_\beta}{\partial t}\right)_{\text{pn-e}} + \left(\frac{\partial s_\beta}{\partial t}\right)_{\text{pn-e-pt}} \tag{5.6}$$

Eq. (5.5) and Eq. (5.6) have two notable advantages over other approaches. First, they require few, if any, phenomenological approximations for the scattering processes [40] and thus provide the most complete description of plasma dynamics in this dissertation. Second,

the quantized nature of pulse-material interactions (such as laser-pulse energy absorption by integer multiples of the photon energy) arise naturally under this formulation. However, solving Eq. (5.5) and Eq. (5.6) simultaneously can be extremely time consuming, as the quantum mechanical collision integrals must be evaluated stochastically [44], often by Monte Carlo integration techniques. To reduce the complexity of these calculations, many authors investigating the interaction of ultrashort pulses with matter consider only one spatial dimension (or sometimes one spatial point), purely isotropic materials, and a parabolic dispersion relation for free electrons, *i.e.* $b(\vec{x},\vec{k},t) \longrightarrow b(\epsilon,t)$, where $\epsilon = \hbar^2 k^2/(2m)$ is the free-electron energy. Even with these simplifications the Boltzmann equation is far more arduous to implement directly than the Fokker-Planck equation, which is why the latter has been selected as the basis for this chapter. For a more detailed discussion of the Boltzmann equation and formulas for the collision integrals above please see Refs. [40; 44; 93].

5.2.2 The Fokker-Planck Equation

The Fokker-Planck equation (FPE) is a classical PDE that can be used to model the free-electron dynamics of condensed matter in energy space [36]. It is derivable directly from, and independently from, the Boltzmann equation [43; 94] under the assumption of an isotropic material with characteristic relaxation times. FPEs have been used since 1930 [57] to phenomenologically model stochastic behavior, such as Brownian motion. In the context of ultrafast plasma dynamics, it describes the time evolution of a distribution function $f(\vec{x},\epsilon,t)$ which gives the number density of free electrons per unit energy such that:

$$\rho(\vec{x},t) = \int_0^\infty f(\vec{x},\epsilon,t)\, d\epsilon, \tag{5.7}$$

where $\rho(\vec{x},t)$ is the free-carrier density and

$$\rho(\vec{x},t)\, \langle \epsilon_e \rangle_\epsilon = \int_0^\infty \epsilon\, f(\vec{x},\epsilon,t)\, d\epsilon, \tag{5.8}$$

gives the total energy of the free-electron gas. Note that $\langle \epsilon_e \rangle_\epsilon$ indicates the average energy per free electron and, for a distribution in thermal equilibrium, is related to the electron gas

temperature by $\langle \epsilon_e \rangle_\epsilon = (3/2)k_B T$. where $\langle \rangle_\epsilon$ indicates the energy average defined to be

$$\langle g \rangle_\epsilon = \frac{\int_0^\infty g(\epsilon) f(\epsilon, t)}{\int_0^\infty f(\epsilon, t)}.$$

The energy distribution function $f(\epsilon, t)$ is also related to the solution of the Boltzmann equation by $b(\epsilon, t) = f(\epsilon, t)D(\epsilon)$, where $D(\epsilon)$ is the density of states in the energy domain.

Suppressing the spatial dependence for notational simplicity, the FPE for plasma dynamics of an absorbing medium is given by [36; 41; 94]:

$$\frac{\partial f}{\partial t} = -\frac{\partial}{\partial \epsilon}\left[D_1(\epsilon) f(\epsilon, t)\right] + \frac{\partial^2}{\partial \epsilon^2}\left[D_2(\epsilon) f(\epsilon, t)\right] + S(\epsilon, t), \tag{5.9}$$

where $D_1(\epsilon)$ and $D_2(\epsilon)$ are energy drift and dispersion coefficients, respectively, and $S(\epsilon, t)$ is a term representing the contributions of sinks and sources of the electron distribution. For the case of an alternating electric field, the drift and dispersion coefficients were first derived by Holway [36; 41; 94] in terms of the root mean square of the electric field amplitude, $E_{\rm rms}$, which is related to the electric field envelope as defined in Eq. (3.5a) by $E_{\rm rms} = |\xi| / \sqrt{2}$. Expressed in terms of the optical intensity $I(t)$, Holway's $D_1(\epsilon)$ and $D_2(\epsilon)$ coefficients are

$$D_1(\epsilon) = \sigma(\epsilon) I(t) + \frac{2}{3}\frac{\partial \sigma}{\partial \epsilon} I(t)\epsilon - U_{\rm pn}\gamma(\epsilon), \tag{5.10}$$

$$D_2(\epsilon) = \frac{2}{3}\sigma(\epsilon) I(t)\epsilon, \tag{5.11}$$

where

$$\sigma(\epsilon) = \frac{e_0^2\, \tau_{\rm c}(\epsilon)}{n_0 \epsilon_0 c m \left[1 + \omega_0^2 \tau_{\rm c}^2(\epsilon)\right]} \tag{5.12}$$

is now the energy dependent cross-section of inverse Bremsstrahlung absorption, since the collision time $\tau_{\rm c}(\epsilon)$ is energy dependent. The last term in Eq. (5.10) is a term that accounts for electron energy dissipation into the lattice, where $U_{\rm pn}$ is the characteristic phonon energy and $\gamma(\epsilon)$ is the characteristic electron-phonon scattering rate.

There are three sources and sinks of plasma electrons [12; 19; 95]:

$$S(\epsilon, t) = R_{\rm pi}(\epsilon, t) + R_{\rm imp}(\epsilon, t) + R_{\rm rec}(\epsilon, t). \tag{5.13}$$

Here the first term on the right-hand side provides the contribution of photoionization:

$$R_{\rm pi}(\epsilon,t) = W_{\rm PI}(\xi)F(\epsilon,\xi), \tag{5.14}$$

where $W_{\rm PI}(\xi)$ is given by Eq. (3.20), and $F(\epsilon,\xi)$ is the distribution function of the photoionized electrons such that $\int_0^\infty F(\epsilon,\xi)d\epsilon = 1$. This dissertation uses the formulation given by Kaiser [40], *et. al.*; $F(\epsilon,\xi) = \delta(\epsilon - \epsilon_{\rm pi})$ where

$$\epsilon_{\rm pi} = \frac{\hbar\omega}{(1+m/m_v)}\left\langle \frac{U_0 + \frac{e_0^2|\xi|^2}{4m\omega^2}}{\hbar\omega} + 1 \right\rangle \tag{5.15}$$

is the initial kinetic energy of the photoionized electron and the $\langle\rangle$ notation denotes the integer part of the enclosed quantity. The second term of the right-hand side of Eq. (5.13) is given by Keldysh's model of impact ionization:

$$R_{\rm imp}(\epsilon,t) = -\nu_i(\epsilon)f(\epsilon,t) + 4\nu_i(2\epsilon+U_0)f(2\epsilon+U_0,t). \tag{5.16}$$

Here $\nu_i(\epsilon)$ is the impact ionization probability rate given by

$$\nu_i(\epsilon) = P_\alpha\left[\frac{\epsilon-\epsilon_{\rm crit}}{\epsilon_{\rm crit}}\right]^2\Theta(\epsilon-\epsilon_{\rm crit}), \tag{5.17}$$

$\epsilon_{\rm crit}$ is the critical energy for impact ionization to occur, $\Theta(x)$ is the Heaviside step function, P_α is a characteristic collision rate, m is the effective mass of the conduction electron and m_v is the effective mass of the valence electron. The factor of 4 on the right-hand side of Eq. (5.16) can be understood by integrating the equation over all energy to find that the total rate of impact ionization is $\int_0^\infty \nu_i(\epsilon)f(\epsilon,t)d\epsilon$. Finally, the third term on the right-hand side of Eq. (5.13) is an electron-hole recombination contribution.

$$R_{\rm rec}(\epsilon,t) = -\frac{f(\epsilon,t)}{\tau_s} \tag{5.18}$$

In the absence of both source terms and the electron-lattice energy dissipation term, Eq. (5.9) can be multiplied by ϵ and integrated over all energy to find the total energy absorbed from the laser field and deposited into the free-electron gas. Note that in this

integration the dispersion term vanishes upon integration by parts, implying that the total energy per unit volume per unit time absorbed from the laser field by the electron gas is

$$\frac{\partial I}{\partial z} = \int_0^\infty \left(\sigma(\epsilon) I(t) f(\epsilon, t) + \frac{2}{3} \frac{\partial \sigma}{\partial \epsilon} I(t) \epsilon f(\epsilon, t) \right) d\epsilon. \tag{5.19}$$

This ensures that all energy absorption from the laser field by the electron gas comes from the drift term of equation Eq. (5.9), whereas the dispersion terms only serves to spread peaks in the electron energy distribution.

The FPE treats plasma dynamics in a continuous way, and Eq. (5.9) is often rewritten in the form of a continuity equation in energy space [12; 36; 41; 95]:

$$\frac{\partial f}{\partial t} = -\frac{\partial}{\partial \epsilon} \left[V_{\text{eff}}(\epsilon, t) f(\epsilon, t) - D_{\text{dif}}(\epsilon, t) \frac{\partial f}{\partial \epsilon} \right] + S(\epsilon, t), \tag{5.20}$$

where

$$V_{\text{eff}}(\epsilon, t) = \frac{1}{3} \sigma(\epsilon) I(t) - U_{\text{pn}} \gamma(\epsilon) \tag{5.21}$$

and

$$D_{\text{eff}}(\epsilon, t) = \frac{2}{3} \sigma(\epsilon) I(t) \epsilon \tag{5.22}$$

are effective drift and diffusion coefficients. This is a mathematically convenient expression (the energy derivative of $\sigma(\epsilon)$ does not appear in this formulation) and is more amenable to solve numerically using standard finite difference techniques. However, the author wishes to reiterate the warning of Holway [94] that while $V_{\text{eff}}(\epsilon, t)$ behaves *like* a drift term, it does not represent the true average change in energy per electron per unit time, nor does the effective diffusion term in Eq. (5.20) conserve energy. Therefore, this formulism no longer allows one to confine laser pulse energy absorption to the drift term of the right-hand side [41].

5.3 Comparing the Rethfeld and Fokker-Planck Descriptions of Plasma Dynamics

This section presents preliminary results of an study comparing the Rethfeld multi-rate equation [11] with the FPE [94] as models of plasma dynamics. For the simulations presented

in Sec. 5.1.1, the multi-rate equation was used and was solved with an adaptive step-size Runge-Kutta method for coupled ordinary differential equations [59]. In this section the FPE is solved for a laser pulse interacting with the fused silica sample surface at the threshold pulse energy for optical damage and the results of which are compared to predictions of the Rethfeld model. The FPE is solved using a split-step method solving the source terms, Eq. (5.13), in one step (a plasma generation step) and the remaining Fokker-Planck transport terms in another step (a PDE step). The PDE step itself is also solved using a split-step method. Here the effective drift term of Eq. 5.20) was solved using a two-step Lax-Wendroff scheme [59] while the effective diffusion term was solved using a foward-time centered-space method [59], both of which are second-order accurate methods. The source terms were again solved using adaptive step-size Runge-Kutta methods of fourth-order accuracy.

Table 5.1: Simulation parameters for the Fokker-Planck equation.

Parameter	*Description*	*Value*	*Units*
U_{pn}	Phonon energy	0.033	eV
γ	Phonon scattering rate	0.1	fs^{-1}
P_α	Keldysh impact parameter	1.5	fs^{-1}
U_0	Material band gap	9	eV
m	Effective electron (conduction) mass	1	m_e
m_v	Effective electron (valence) mass	1	m_e
τ_r	Electron recombination time	150	fs

This study was performed by numerically constructing 1D laser pulses from the experimental information in Fig. (5.1), for pulse energies ranging from 30 μJ to 60 μJ, thus using the energies near the laboratory measured damage threshold for the fused silica sample. More specifically, this study takes the focused laser beam from Sec. 5.1.1, extracts a 1D laser pulse from the center of the focused beam, and allows this pulse to interact with the material surface while monitoring the plasma dynamics using the Rethfeld and FPE models. This laser pulse has the temporal shape given in Fig. (5.1b) and, in the case of the 60 μJ pulse, has a peak intensity of 3.08×10^{13} W cm^{-2}. Required parameters used in solving the FPE

are listed in Table 5.3. Throughout the interaction of the laser pulse with the material, a constant collision time of 5 fs was assumed for both models. The FPE model also used standard values for the characteristic phonon energy $U_{\text{pn}} = 0.033$ eV [12] and phonon collision rate $\gamma = 10^{14}$ s^{-1} [96].

Figure (5.3) shows the resulting distribution of electrons in energy space for the 60 μJ laser pulse at three separate times as measured in the retarded time frame of the pulse ($f(\epsilon, \tau = -100$ fs), $f(\epsilon, \tau = 0$ fs), and $f(\epsilon, \tau = -100$ fs)) as well as the total plasma density as a function of time for both models. Note that the results for the Rethfeld model appear as a series of bars representing discrete populations (the energy ladder) while the FPE distribution is continuous. The three vertical dotted lines on in Fig. (5.3d) indicate the three temporal positions at which the distributions of Fig. (5.3a), Fig. (5.3b), and Fig. (5.3c) were measured. The evolution of these distributions may be described as follows. Figure (5.3a) shows the initial stages of the evolution where photoionization is the primary generator of plasma electrons. At this stage there has been noticeable energy absorption by free carriers, occupying higher energy levels in the conduction band, but photoionization remains dominant. Figure (5.3b) shows the free-carrier energy distributions at the temporal center of the laser pulse. Here the optical intensity is at its highest (see Fig. (5.1)) and the critical energy for impact ionization is increased according to the manner of Eq. (5.2). Thus, both distributions are temporarily allowed to drift further up in energy space without impact ionization occuring. As the intensity lowers on the trailing edge of the pulse, the critical energy for impact ionization is also lowered, and many of the higher energy electrons in the distributions are suddenly "caught" in a region with a very high probability of impact ionization. These electrons avalanche and form the final distributions seen in Fig. (5.3c).

Fig. (5.3d) demonstrates that the FPE model actually predicts permanent laser-induced damage on the sample surface for this collision time whereas the Rethfeld model does not (using the common ultrafast optics definition of $\rho > 10^{21}$cm^{-3} as an indicator of damage). This is due to the fact that the Rethfeld model explicitly assumes that newly freed electrons

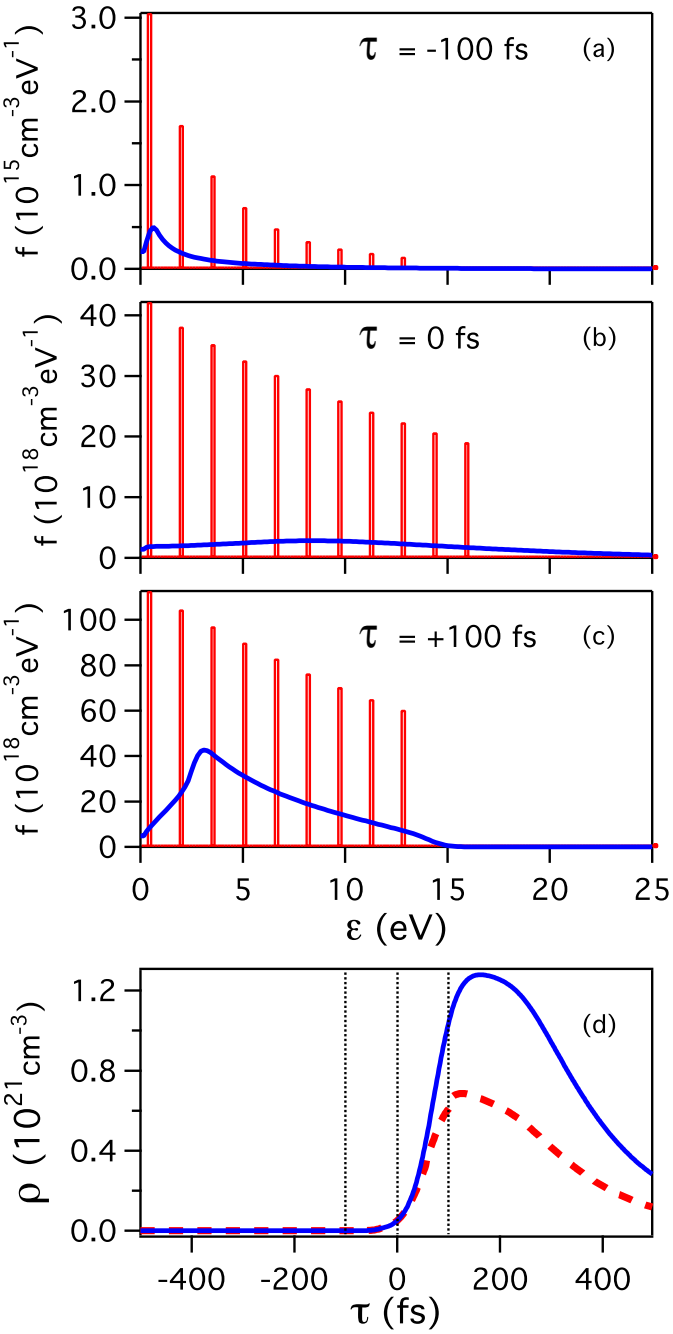

Figure 5.4: Results from solving the multi-rate equation (red, bars and dashed line) and the Fokker-Planck equation (blue, solid line). Plots (a), (b), and (c) show the plasma density distribution $f(\epsilon)$ at the retarded times $\tau = -100$ fs, $\tau = 0$ fs, and $\tau = 100$ fs, respectively. These three times are further denoted with the dashed black lines in plot (d) which shows the total plasma density $\rho(\tau)$ as a function of the retarded time.

(whether by photoionization or avalanching) first appear at the bottom of the conduction band. This is not generally true, and the FPE model accounts for the fact that photoionized electrons have some residual kinetic energy when they first appear in the conduction band. It also accounts for the fact that impact ionization does not generally start electrons off at the bottom of the conduction band either, but splits the residual kinetic energy of the impacting conduction electron, $\epsilon_{\text{crit}} - U_0$, evenly between the two resulting low energy electrons. All of this poses another significant problem. The more detailed FPE model was implemented and tested against the Rethfeld model in hopes of achieving a result closer to the experimentally measured damage threshold for a 60 μJ pulse under the conditions of Sec. 5.1.1. However, Fig. (5.3d) clearly demonstrates that the FPE model, such as it is, predicts results even further removed from experimentally measured values than the Rethfeld model. This same simulation was repeated with pulse energies ranging from 30 μJ to 55 μJ, using collision times from ranging from 5 fs to 10 fs. Although these simulations were below the damage threshold, the same qualitative behavior displayed throughout Fig. (5.3) appeared in all cases.

5.4 Discussion

Here is presented a list of possible explanations for the results presented in this chapter. If still better material models are needed to accurately model the pulse propagation through the sample, there are several promising possibilities. The first option is to include the explicit energy dependence of the electronic collision time and the phonon scattering rate in the FPE. The second option is to implement the fifth-order nonlinear polarization contribution [3]. This may have the effect of counter acting the effects of self-focusing somewhat [1], but detailed studies on this subject are limited [21]. It is also still possible that the laser pulse was not properly represented at the sample surface. If the sample were displaced even a half of a millimeter away from the geometric beam focus, then the peak intensities of the simulations could be lowered considerably, thereby raising the damage threshold pulse energy.

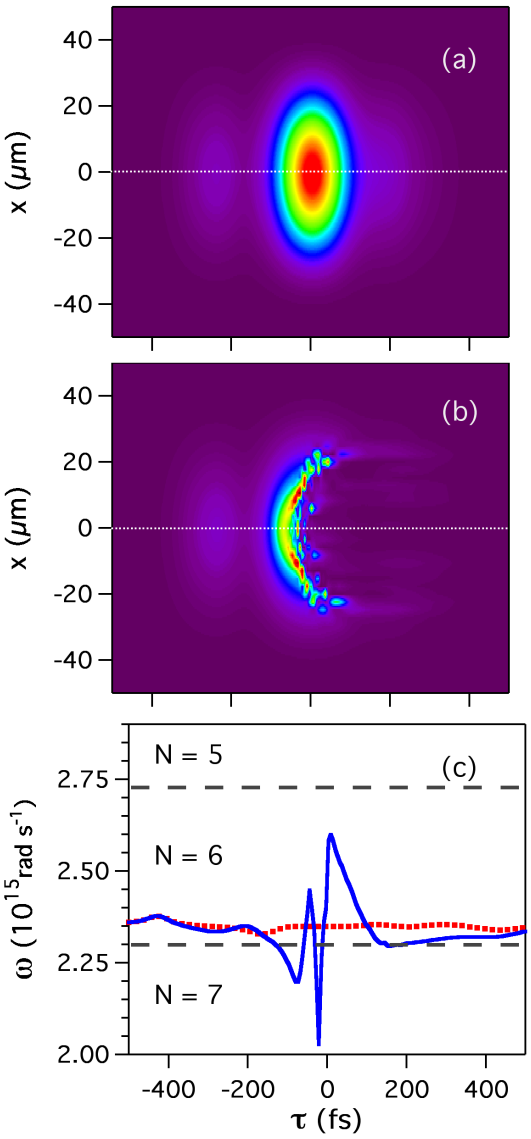

Figure 5.5: The normalized intensity in the x-τ plane for (a) the initial 60 μJ laser pulse and (b) the 60 μJ pulse after 200 μm of propagation through fused silica with a collision time of 5 fs. The instantaneous frequency as a function of time through the respective spatial centers of these pulses (see the dotted white lines in (a) and (b)) is shown by (c). The frequency of the pulse in (a) is shown by the red (dotted) line and that of the final pulse is shown by the blue (solid) line. The grey (dashed) lines in (c) marks the multi-photon ionization transition between a 7-photon process (the lowest region), a 6-photon required process (the middle region), and a 5-photon process (the top region).

Another striking possibility is that, to the author's knowledge, no model of plasma dynamics to date account for ultrashort pulse effects. One plain example of this is the frequency dependence of photoionization. At lower optical intensities the dominate photoionization process is multi-photon ionization where the simultaneous absorption of N photons of energy $\hbar\omega$ are required to cross the band gap U_0 [80] ($N = 6$ in fused silica for 800 nm light). Shifts in the instantaneous frequency of a laser pulse can therefore lead to a drastically altered photoionization rate if, for example, 7 photons of a particular instantaneous frequency are suddenly required to cross the band gap instead of 6. The real question then becomes, do the pulses presented in this chapter contain such frequency shifts? Figure (5.4c) displays the instantaneous frequency as a function of the retarded time at the spatial center the initial pulse given in Fig. (5.1b) and for the 60 μJ laser pulse after having propagated through the 200 μm fused silica sample (a collision time of 5 fs with the multi-rate equation model was used to obtain this result). Note that the grey (dashed) line in Fig. (5.4c) gives the transition frequency from a 6-photon photoionization process to a 7-photon process. Note further that significant portions of the final pulse, shown in Fig. (5.4b), lie within the 7-photon region, particularly the red-shifted front of the pulse where photoionization is required to initiate the plasma generation process. This could have the result of delaying the onset of plasma generation and possibly avoiding laser-pulse induced material modification.

The absorption of photons of arbitrary instantaneous frequencies (*i.e.* arbitrary photon energies) also introduces a problem into the Rethfeld description of avalanching by breaking the evenly spaced "ladder" model of electron populations. One could in principle simply extend the Rethfeld model into a continuous energy space, treating each discrete energy bin as an individual population capable of advancing an electron up the conduction band by arbitrary intervals of $\hbar\omega$. This extended Rethfeld model could also account for the more detailed placements of electrons in the conduction band as given by the source terms of the FPE. However, by creating a continuous distribution in energy space, one is essentially approximating the solution to the FPE, but without the physically relevant dispersion terms.

Rather than take this approach, one may as well just solve the FPE. Unfortunately, interfacing the FPE with the modified NLSE for pulse propagation is not straightforward and no attempt of this kind has been reported in the literature to the author's knowledge.

5.5 Interfacing PDE Models of Plasma Dynamics with the Modified NLSE

All models of plasma dynamics to date are, to the author's knowledge, inconsistent with the predictions of the modified NLSE for ultrashort pulse propagation. In the FPE model, for example, laser energy absorption by free carriers is given by Eq. (5.19), whereas the modified NLSE derived in Chapter 3 predicts, to a first-order temporal correction, a free-carrier absorption given by Eq. (3.17). If one assumes for simplicity that the collision time, and therefore the absorption cross-section σ, are independent of the conduction band energy, then the FPE model cannot account for temporal corrections inherent to ultrashort pulse propagation as demonstrated in Chapter 3, nor can any other model of plasma dynamics in the literature. This is probably due to the fact that these models were derived before the ultrashort corrections to the Drude free current density were necessary (*i.e.* before the advent of ultrashort pulses). However, for the sake of consistency, a modified Fokker-Planck equation should be derived. Such an investigation should begin by deriving a rate equation for the free current-density distribution in energy space $\vec{\Upsilon}(\vec{x},\epsilon,t)$ [42] from the Boltzmann equation [35]. The integral of this quantity over all energy would then yield the total free-carrier density;

$$\vec{J}_f(\vec{x},t) = \int_0^\infty \vec{\Upsilon}(\vec{x},\epsilon,t)d\epsilon, \tag{5.23}$$

or, in complex envelope notation

$$j_f(\vec{x},t) = \int_0^\infty \upsilon(\vec{x},\epsilon,t)d\epsilon, \tag{5.24}$$

where $\upsilon(\vec{x},\epsilon,t)$ is the complex envelope of $\vec{\Upsilon}(\vec{x},\epsilon,t)$. The modified Fokker-Planck equation must then be given by a continuity equation in energy space [42];

$$\frac{\partial f}{\partial t} = -\frac{\partial}{\partial \epsilon}\left(\frac{1}{2}\Re\left[\xi^*(\vec{x},t)\upsilon(\vec{x},\epsilon,t)\right]\right) + S(\epsilon,t), \tag{5.25}$$

where ξ is the electric field envelope. This derivation is the subject of ongoing research by the author. Due to the complicated energy dependence of parameters in the FPE model, deriving an analytic form for the free current density envelope, as presented in Chapter 3, may not be possible. Generally, when calculating the plasma dynamics, $\upsilon(\vec{x}, \epsilon, t)$ and $f(\vec{x}, \epsilon, t)$ will have to be solved simultaneously. The function $\upsilon(\vec{x}, \epsilon, t)$ can then be integrated over all energy and the resulting current density envelope can be inserted directly into Eq. (3.10).

Once a modified FPE is interfaced in a consistent manner with the modified NLSE, one is then faced with the equally significant problem of much slower simulations. For the results presented in this chapter, the FPE simulations ran nearly two orders of magnitude longer to run than the corresponding multi-rate equation simulations. A modified FPE is likely to be even more computationally illusive, requiring the additional calculation of field and current-density time derivatives. Parallelization and additional optimization would play an important role in minimizing this problem in the future.

5.6 Concluding Remarks

Recent experimental work, in collaboration with simulations written by the author, have demonstrated that more detailed PDE models of plasma dynamics may be necessary to accurately model high-intensity ultrashort pulse propagation through dielectric materials. Simulations of ultrashort pulse propagation utilizing fully 3+1D laser pulses numerically constructed according to laboratory measured beam profiles and pulse shape information were interfaced with the multi-rate equation description of plasma dynamics in fused silica. The final results were compared directly to those of experiment, and represent, to the author's knowledge, the most detailed study of its kind to date. Discrepancies between the results of simulation and experiment appeared near the optical damage threshold, and suggest that more detailed material models are in order. A Fokker-Planck equation describing a continuous energy space for the free-electron gas was used for this purpose and compared with Rethfeld's multi-rate equation description. Preliminary results were presented and possibilities for

future investigations with still more detailed material models were proposed. In particular, a modified Fokker-Planck equation is needed to account for instantaneous frequency shifts and the ultrashort free-carrier dispersion corrections predicted by the Eq. (3.16). The benefits of interfacing this modified Fokker-Planck equation with the modified NLSE are that all ultrashort pulse effects will appear explicitly in evolution of the electron plasma, which to date has not been addressed in the literature for any model of plasma dynamics. It also has the advantage of including plasma energy diffusive effects and lattice effects in a phenomenological manner so that a more laborious Boltzmann equation approach is not required. However, a comprehensive derivation should be performed starting from the Boltzmann equation, and is currently planned as a future research project.

Chapter 6

Conclusions

Simulations in computational optics have proven to be very effective tools for gaining insight into ultrafast laser pulse-induced damage in optical materials. Such studies in principle require the accurate modeling not only of ultrashort pulse propagation through nonlinear media, but also the dynamics of the free-electron plasma. For practical considerations, many simulations in the field of computational optics employ simplified models for pulse propagation such as analytical beam geometries and pulse shapes, as well as simplified models for plasma evolution, such as a single-rate equation. The work presented in this dissertation was a deliberate attempt by the author to test the validity of these simplifications, which in many cases were found wanting.

A modified nonlinear Schrödinger equation (NLSE) for ultrashort pulse propagation was derived in Chapter 3. This equation included ultrashort temporal corrections to the free current density envelope as described by the Drude model. In the same chapter this free-carrier contribution to the modified NLSE was analyzed and compared to other models currently used in the literature. Results from simulations solving the modified NLSE for the material of fused silica were then presented to demonstrate how differences between such models might arise in experiment. Simulations solving the modified NLSE were again used in Chapter 4 to examine the influence of laser beam geometry and pulse shape on plasma generation and laser pulse induced modification in fused silica using the single-rate equation description of Stuart [12] to model the excitation of a free-electron plasma in the conduction band. It was found that minor asymmetries in the beam shape, such as those found in the typical laboratory laser beam, can significantly affect the generation of the

free-electron plasma in dielectric materials. This work thus demonstrates the need for more detailed descriptions of pulse and beam structure if one intends to accurately predict laser pulse-induced modifications to a material or perform spectrographic analysis on the predicted outgoing laser pulse to provide insight into the field-material interactions.

In Chapter 5, simulations solving the modified NLSE for ultrashort pulse propagation were performed using laser pulses numerically constructed according to experimentally measured beam profiles and pulse shape data, all the while using the multi-rate equation description developed by Rethfeld [11] to model the plasma dynamics in the conduction band. To the author's knowledge, these simulations are the first of their kind using pulses both spatially and temporally constructed according to laboratory data, as well as interfacing the multi-rate equation model of plasma dynamics with the modified NLSE for pulse propagation. Direct comparison with experimental results revealed unique successes in the prediction of pulse evolution, but also suggest that more detailed material models should be employed in future simulations for an improved, direct comparison with experiment. Chapter 5 the case for using more detailed models of plasma dynamics in computational optics, and several possible options of such models, including a Fokker-Planck equation [41] modified to account for ultrashort optical effects, are proposed.

However, more advanced models of plasma dynamics, such as the Fokker-Planck equation, can only be interfaced with the modified NLSE derived in Chapter 3 once a comprehensive formalism has been developed for the distribution of the free current density in energy space. This step is necessary to ensure that the energy absorption from the laser field by the free carriers, as predicted by the model of plasma dynamics, is consistent with the ultrashort temporal corrections to the free-carrier energy absorption predicted in modified NLSE of Chapter 3. Such a study has not been addressed in the published literature, to the author's knowledge. Additionally, all of the simulations presented in this dissertation were performed on a single-processor platform, taking a maximum time of two weeks to complete 300 steps along the propagation axis. Using the same single-processor platform, it

would take approximately two weeks to complete a single step along the propagation axis if the pulse propagation equation were to be solved simultaneously with the Fokker-Planck equation (depending on the intensity of the field). Therefore, for practical considerations, the author's code will need to be parallelized in the future to reduce the total computation time.

If the interfacing of a modified Fokker-Planck equation with the modified NLSE still does not produce results that match with experiment, as evidenced by a study similar to that presented in Sec. 5.1.1, then one might try employing the still more detailed Boltzmann equation description of material dynamics [40; 93]. This would require an even longer computational time period to model the plasma dynamics, but for most simulations it would still be more efficient than replacing the pulse propagation equation with an FDTD technique. Once an adequate technique for predicting fully 3+1D pulse pulse propagation through a plasma generating medium is established, secure knowledge about the pulse intensity through all space and time can be used to test new models such as Gruzdev's [82; 97; 98] prediction of a laser-induced damage threshold intensity of 10^{13} W cm^{-2} that is completely independent of impact ionization processes. It is expected that the better understanding provided from such studies will enable the accurate simulation of optical damage in a variety of materials, ultimately leading to an enhanced control of laser-induced modification to dielectrics and semiconductors.

Appendix A

On the Fourier Transform, Optical Intensity, and Spectrum

In this dissertation, any quantity in frequency space which can be usefully defined as the Fourier transform of a real time physical quantity is indicated by a tilde symbol overhead. Additionally, the symmetric definition of the Fourier transform is used throughout this dissertation such that a forward Fourier transform into frequency space and the inverse transform back into the time domain are expressed as [99]:

$$\tilde{f}(\omega) = \frac{1}{\sqrt{2\pi}} \int_{-\infty}^{\infty} f(t)\, e^{i\omega t}\, dt, \tag{A.1}$$

$$f(t) = \frac{1}{\sqrt{2\pi}} \int_{-\infty}^{\infty} \tilde{f}(\omega)\, e^{-i\omega t}\, d\omega. \tag{A.2}$$

Having used the symmetric form of the Fourier transform, the time and frequency expressions for the function f are also related by Parseval's Theorem [99]:

$$\int_{-\infty}^{\infty} |f(t)|^2\, dt = \int_{-\infty}^{\infty} \left|\tilde{f}(\omega)\right|^2 d\omega. \tag{A.3}$$

The Fourier transform of the electric field (or any real time quantity) expressed in the complex envelope notation of Eq. (2.6) will thus take the form:

$$\begin{aligned} \tilde{E}(\omega) &= \frac{1}{\sqrt{2\pi}} \int_{-\infty}^{\infty} \frac{1}{2} \left(\xi(t) e^{-i\omega_0 t + i\phi_0} + \text{c.c})\right) e^{i\omega t}\, dt, \\ \tilde{E}(\omega) &= \tilde{\xi}(\omega - \omega_0)\frac{e^{i\phi_0}}{2} + \tilde{\xi}^*(\omega + \omega_0)\frac{e^{-i\phi_0}}{2}. \end{aligned} \tag{A.4}$$

where the first term represents the forward propagating field component and the second term represents the backwards propagating field component [3]. It is now possible to define time-averaged and frequency-averaged intensities $I(t)$ and $S(\omega)$, respectively. A straightforward

time average of $|E(t)|^2$ yields $(1/2)\xi(t)\xi^*(t)$, but the frequency average of $\left|\tilde{E}(\omega)\right|^2$ requires careful consideration. Initially, the frequency average of $\left|\tilde{E}(\omega)\right|^2$ is

$$\left|\tilde{E}(\omega)\right|^2 = \frac{1}{4}\left|\tilde{\xi}(\omega-\omega_0)\right|^2 + \frac{1}{4}\left|\tilde{\xi}(\omega+\omega_0)\right|^2. \tag{A.5}$$

However, since $E(t)$ must be real the well known condition $\tilde{E}^*(\omega) = \tilde{E}(-\omega)$ applies [81]. This further implies that the envelope function in frequency space must be symmetric, *i.e.* $\tilde{\xi}(\omega) = \tilde{\xi}(-\omega)$. Also, note that Eq. (A.5) is itself symmetric about $\omega = 0$. Therefore, if the associated spectral width $\Delta\omega$, defined to be the full width at half maximum of $\left|\tilde{\xi}(\omega)\right|^2$, is much smaller than the carrier frequency ($\Delta\omega \ll \omega_0$) then for positive values of ω the right-hand side of Eq. (A.5) reduces to the first term only. Likewise, for negative frequencies the right-hand side reduces to the second term only. Thus, the total contribution of both forward and backward components to the frequency averaged spectrum can be expressed as $\left|\tilde{E}(\omega')\right|^2 = (1/2)\left|\tilde{\xi}(\omega'-\omega_0)\right|^2$, where ω' is nonnegative. The optical intensity and the spectrum may now be defined as [30]:

$$I(t) = \frac{1}{2}n\epsilon_0 c\,|\xi(t)|^2 \tag{A.6}$$

$$S(\omega) = \frac{1}{2}n\epsilon_0 c\left|\tilde{\xi}(\omega-\omega_0)\right|^2 \tag{A.7}$$

where n is the index of refraction, ϵ_0 is the permittivity of free space, and c is the speed of light in a vacuum. Note that although the spectrum $S(\omega)$ is a function of frequency, it is not written with a tilde because it is not the Fourier transform of a useful function of time. Finally, note these two quantities are also related by Parseval's theorem:

$$\int_{-\infty}^{\infty} I(t)\,dt = \int_0^{\infty} S(\omega)\,d\omega. \tag{A.8}$$

Appendix B

The Nonlinear Polarization

Although Eq. (2.1) is widely used in the literature, it can be deceiving. The polarization $\vec{P}$ in Eq. (2.1) is not the Fourier transform of the real time polarization into frequency space. Rather, all functions in this expression are the real time Fourier components which propagate with the specified frequency.

Strictly speaking, the n^{th}-order polarization terms in real time and frequency space are given by the following expressions [22]:

$$\vec{P}^{(n)}(t) = \int_{-\infty}^{\infty}\int_{-\infty}^{\infty}\cdots\int_{-\infty}^{\infty} dt_1 dt_2 \cdots dt_n \overleftrightarrow{\chi}^{(n)}(t_1, t_2, ..., t_n)\vec{E}(t-t_1)\vec{E}(t-t_2)\cdots\vec{E}(t-t_n), \tag{B.1}$$

$$\tilde{\vec{P}}^{(n)}(\omega) = \int_{-\infty}^{\infty}\int_{-\infty}^{\infty}\cdots\int_{-\infty}^{\infty} d\omega_1 d\omega_2 \cdots d\omega_n \tilde{\overleftrightarrow{\chi}}^{(n)}(\omega_1, \omega_2, ..., \omega_n)\tilde{\vec{E}}(\omega_1)\tilde{\vec{E}}(\omega_2)\cdots\tilde{\vec{E}}(\omega_n). \tag{B.2}$$

However, the summation condition of the frequencies must still be satisfied in frequency space such that for any polarization term $\omega = \omega_1 + \omega_2 + \cdots + \omega_n$; thus eliminating one of the integrals in frequency to give

$$\tilde{\vec{P}}^{(n)}(\omega) = \int_{-\infty}^{\infty}\cdots\int_{-\infty}^{\infty} d\omega_1 \cdots d\omega_{n-1} \tilde{\overleftrightarrow{\chi}}^{(n)}(\omega_1, \omega_2, ..., \omega_n)\tilde{\vec{E}}(\omega_1)\tilde{\vec{E}}(\omega_2)\cdots\tilde{\vec{E}}(\omega_n). \tag{B.3}$$

where $\omega_n = \omega - (\omega_1 + \cdots + \omega_{n-1})$. Eq. (B.1) and Eq. (B.3) are the generally correct expressions for the n^{th}-order polarization. Eq. (2.1) is best interpreted as the real time contribution to the polarization of multiple monochromatic fields and thus provides a good qualitative description of nonlinear optical behavior in many cases. For ultrashort pulses which are not monochromatic, the complete descriptions of Eq. (B.1) or Eq. (B.3) should be used [22].

Appendix C

Derivation of the Wave Propagation Equation

The spatially-averaged macroscopic Maxwell equations in matter are [23]:

$$\vec{\nabla}\cdot\vec{D} = \rho_f \tag{C.1a}$$

$$\vec{\nabla}\times\vec{E} = -\frac{\partial\vec{B}}{\partial t} \tag{C.1b}$$

$$\vec{\nabla}\cdot\vec{B} = 0 \tag{C.1c}$$

$$\vec{\nabla}\times\vec{H} = \vec{J}_f + \frac{\partial\vec{D}}{\partial t}, \tag{C.1d}$$

Where $\vec{E}$ is the electric field, $\vec{B}$ is the magnetic field, $\vec{D} = \epsilon_0\vec{E}+\vec{P}$ is the electric displacement field, $\vec{H} = \vec{B}/\mu_0 - \vec{M}$ is the auxiliary field, $\vec{P}$ is the material polarization, $\vec{M}$ is the material magnetization, and the two source terms ρ_f and $\vec{J}_f$ are the free charge density and free current density, respectively. The initial assumptions for deriving the wave propagation equation are that the material is nonmagnetic, $\vec{M} = 0$, and that the free charge density $\rho_f = 0$. Note that the condition $\rho_f = 0$ does not imply that $\vec{J}_f = 0$, it only states that no part of the bulk material is allowed to have a nonzero electric monopole moment.

With the above assumptions, the cross product of Eq. (C.1b) is taken and the double cross product vector identity is applied to the right-hand side,

$$\vec{\nabla}(\vec{\nabla}\cdot\vec{E}) - \nabla^2\vec{E} = -\frac{\partial}{\partial t}\vec{\nabla}\times\vec{B}. \tag{C.2}$$

Eqs. (C.1a) and (C.1d) are inserted into the first term on the left-hand side, and the right-hand side, respectively:

$$-\frac{\vec{\nabla}(\vec{\nabla}\cdot\vec{P})}{\epsilon_0} - \nabla^2\vec{E} = -\frac{\partial}{\partial t}\left(\mu_0\vec{J}_f + \epsilon_0\mu_0\frac{\partial\vec{E}}{\partial t} + \mu_0\frac{\partial\vec{P}}{\partial t}\right).$$

The resulting expression can be rewritten as a wave equation with source terms appearing on the right-hand side.

$$\nabla^2\vec{E} - \frac{1}{c^2}\frac{\partial^2\vec{E}}{\partial t^2} = \mu_0\frac{\partial^2\vec{P}}{\partial t^2} + \mu_0\frac{\partial\vec{J}_f}{\partial t} - \frac{\vec{\nabla}(\vec{\nabla}\cdot\vec{P})}{\epsilon_0} \tag{C.3}$$

The $\vec{\nabla}(\vec{\nabla}\cdot\vec{P})$ term in Eq. (C.3) is a polarization diffraction contribution which can sometimes be reduced [100] or eliminated [46], depending on the form of the polarization. In isotropic materials the polarization $\vec{P}$ must be aligned with the electric field and may be expressed in frequency space as given in Appendix B:

$$\tilde{\vec{P}}(\tilde{\vec{E}},\omega) = \epsilon_0\tilde{\chi}^{(1)}(\omega)\tilde{\vec{E}}(\omega) + \tilde{\vec{P}}_{NL}(\tilde{\vec{E}},\omega), \tag{C.4}$$

where $\tilde{\chi}^{(1)}$ is the linear susceptibility and $\tilde{\vec{P}}_{NL}$ represents all of the nonlinear contributions to the total polarization. Note that the time-frequency Fourier transform of Eq. (C.1a) yields $\vec{\nabla}\cdot\tilde{\vec{P}} = -\epsilon_0\vec{\nabla}\cdot\tilde{\vec{E}}$ if $\rho_f = 0$. Substituting Eq. (C.4) into this expression yields

$$\epsilon_0\tilde{\chi}^{(1)}\vec{\nabla}\cdot\tilde{\vec{E}} + \vec{\nabla}\cdot\tilde{\vec{P}}_{NL}(\tilde{\vec{E}}) = \epsilon_0\vec{\nabla}\cdot\tilde{\vec{E}}. \tag{C.5}$$

Examining Eq. (C.5) in the absence of nonlinear effects (assuming an isotropic, uniform medium) reveals that both sides of this equation must vanish for the case of linear optics. This approximation is also valid for the entire perturbative regime of nonlinear optics [26], see Fig. (2.1), and thus the last term of Eq. (C.3) will not make appreciable contributions at those intensities. At higher intensities in the intermediate regime of nonlinear optics, it is generally the case that ionization and plasma effects become much stronger than any polarization diffraction effects [46]. Therefore, the approximation $\nabla\cdot\vec{P} \approx 0$ is assumed for all descriptions of pulse propagation in this dissertation. Eq.(C.3) can then be expressed as:

$$\nabla^2\vec{E} - \frac{1}{c^2}\frac{\partial^2\vec{E}}{\partial t^2} = \mu_0\frac{\partial^2\vec{P}}{\partial t^2} + \mu_0\frac{\partial\vec{J}_f}{\partial t}, \tag{C.6}$$

where the electric field propagates through an electrically neutral, nonmagnetic, isotropic medium at intensities in the linear, perturbative, and intermediate regimes of Fig. (2.1).

Appendix D

Optical quantities derived from a known complex dielectric response

This section derives analytical expressions for common optical quantities as a function of the complex electric permittivity (and complex optical susceptibility). All expressions herein exist not in real time but in frequency space and will carry a tilde overhead to indicate that they are Fourier transforms of real time functions. It is assumed that the field in question is linearly polarized and the materials are isotropic, so an effective dielectric response function may be expressed in terms of an effective susceptibility [3].

$$\tilde{\epsilon}_{\text{eff}}(\omega) = 1 + \tilde{\chi}_{\text{eff}}(\omega) \tag{D.1}$$

Here the term effective means that the susceptibility may include nonlinear effects and plasma contributions in addition to the traditional linear optical terms.

D.1 Real Index of Refraction and Intensity-Based Absorption Function

The complex index of refraction is defined by

$$\tilde{n}(\omega) = \sqrt{\tilde{\epsilon}_{\text{eff}}}. \tag{D.2}$$

The complex refractive index can also be written in terms of real and imaginary parts;

$$\tilde{n} = \tilde{n}_r + i\frac{\tilde{\alpha}\, c}{2\,\omega}, \tag{D.3}$$

where $\tilde{n}_r$ is the real index of refraction, $\tilde{\alpha}$ is the intensity-based absorption function, c is the speed of light in a vacuum, and ω is the frequency of the electric field. The effective electric permittivity is also written is terms of real and imaginary parts: $\tilde{\epsilon}_{\text{eff}} = \tilde{\epsilon}_r + i\tilde{\epsilon}_i$, the

index of refraction is squared and the real and imaginary parts of the resulting expression are equated.

$$\tilde{n}^2 = \tilde{n}_r^2 - \left(\frac{\tilde{\alpha}\, c}{2\,\omega}\right)^2 + i\,\frac{\tilde{\alpha}\, c}{\omega}\tilde{n}_r = \tilde{\epsilon}_r + i\tilde{\epsilon}_i$$

$$\tilde{n}_r^2 - \left(\frac{\tilde{\alpha}\, c}{2\,\omega}\right)^2 = \tilde{\epsilon}_r \tag{D.4}$$

$$\frac{\tilde{\alpha}\, c}{\omega}\,\tilde{n}_r = \tilde{\epsilon}_i \tag{D.5}$$

Equation (D.4) is multiplied by $\tilde{n}_r^2$, Eq. D.5 is substituted into the second term, and the resulting expression is solved for $\tilde{n}_r$.

$$\tilde{n}_r^4 - \left(\frac{\tilde{\alpha}\, c}{2\,\omega}\right)^2 \tilde{n}_r^2 = \tilde{\epsilon}_r\,\tilde{n}_r^2 \tag{D.6}$$

$$\tilde{n}_r^4 - \left(\frac{\tilde{\epsilon}_i}{2}\right)^2 = \tilde{\epsilon}_r\,\tilde{n}_r^2$$

$$\left(\tilde{n}_r^2\right)^2 - \tilde{\epsilon}_r\,\left(\tilde{n}_r^2\right) - \left(\frac{\tilde{\epsilon}_i}{2}\right)^2 = 0$$

$$\tilde{n}_r^2 = \frac{\tilde{\epsilon}_r \pm \sqrt{\tilde{\epsilon}_r^2 - 4\left(-\tilde{\epsilon}_i/2\right)^2}}{2}$$

$$\tilde{n}_r = \pm\sqrt{\frac{\tilde{\epsilon}_r \pm \sqrt{\tilde{\epsilon}_r^2 + \tilde{\epsilon}_i^2}}{2}} \tag{D.7}$$

Eq. (D.6) is quartic in $\tilde{n}_r$ and therefore Eq. (D.7) yields four analytical solutions. However, by definition the only physically realizable solution must be real and positive for all nonzero frequencies (excluding the possibility of metamaterials). The real index and the absorption function are therefore:

$$\tilde{n}_r = \sqrt{\frac{\tilde{\epsilon}_r + \sqrt{\tilde{\epsilon}_r^{\,2} + \tilde{\epsilon}_i^{\,2}}}{2}} \tag{D.8}$$

$$\tilde{\alpha} = \frac{\tilde{\epsilon}_i\ \omega}{\tilde{n}_r\ c} = \frac{\sqrt{2}\,\omega}{c}\sqrt{-\,\tilde{\epsilon}_r + \sqrt{(\tilde{\epsilon}_r)^2 + (\tilde{\epsilon}_i)^2}}. \tag{D.9}$$

D.2 Reflection and Transmission Coefficients of Absorbing Media

The above functions of $\tilde{n}_r(\omega)$ and $\tilde{\alpha}(\omega)$ will be used to determine energy reflection and transmission coefficients for light at normal incidence, $\tilde{R}$ and $\tilde{T}$, respectively. Let the respective functions for medium one, $\tilde{n}_{1r}(\omega)$ and $\tilde{\alpha}_{1r}(\omega)$, and medium two, $\tilde{n}_{2r}(\omega)$ and $\tilde{\alpha}_{2r}(\omega)$, be given by the Equations (D.8) and (D.9). The energy reflection and transmission coefficients for absorbing media at normal incidence are defined to be [23]:

$$\tilde{R} = \left|\frac{\tilde{n}_1 - \tilde{n}_2}{\tilde{n}_1 + \tilde{n}_2}\right|^2 \qquad , \qquad \tilde{T} = 1 - \tilde{R}. \tag{D.10}$$

Collecting the real and imaginary parts for the complex indices, the respective expressions for $\tilde{R}$ and $\tilde{T}$ are:

$$\tilde{R} = \frac{(\tilde{n}_{1r} - \tilde{n}_{2r})^2 + (\tilde{\alpha}_{1r} - \tilde{\alpha}_{2r})^2 \frac{c^2}{4\omega^2}}{(\tilde{n}_{1r} + \tilde{n}_{2r})^2 + (\tilde{\alpha}_{1r} + \tilde{\alpha}_{2r})^2 \frac{c^2}{4\omega^2}} \tag{D.11}$$

$$\tilde{T} = \frac{4\left(\tilde{n}_{1r}\tilde{n}_{2r} + \tilde{\alpha}_{1r}\tilde{\alpha}_{2r}\frac{c^2}{4\omega^2}\right)}{(\tilde{n}_{1r} + \tilde{n}_{2r})^2 + (\tilde{\alpha}_{1r} + \tilde{\alpha}_{2r})^2 \frac{c^2}{4\omega^2}}. \tag{D.12}$$

Note that if both absorption constants are zero, then the well-known linear coefficients are recovered [23]. Also, because of the c^2/ω^2 factors, at least one absorption function must be on the order of $10^4\,\mathrm{cm}^{-1}$ to make appreciable contributions to $\tilde{R}$ and $\tilde{T}$ in the visible/near-IR frequency range, assuming $\tilde{n}_{1r}$ and $\tilde{n}_{2r}$ are of order unity.

Bibliography

[1] R. L. Sutherland, *Handbook of Nonlinear Optics*, Dekker, New York, 2nd ed. (2003).

[2] M. Wegener, *Extreme Nonlinear Optics*, Springer-Verlag (2005).

[3] R. W. Boyd, *Nonlinear Optics*, Academic Press, 2nd ed. (2002).

[4] Y. R. Shen, *The Priciples of Nonlinear Optics*, John Wiley and Sons, Inc. (1984).

[5] C. B. Schaffer, A. Brodeur, and E. Mazur, "Laser-induced breakdown and damage in bulk transparent materials induced by tightly focused femtosecond laser pulses," *Meas. Sci. Technol.* **12**, 1784–1794 (2001).

[6] A. Taflove and S. C. Hagness, *Computational Electrodynamics: The Finite-Difference Time-Domain Method*, Artech House, Inc., 3rd ed. (2000).

[7] P. Gibbon, *Short Pulse Laser Interactions with Matter: An Introduction*, Imperial College Press (2005).

[8] J. R. Gulley, S. W. Winkler, and W. M. Dennis, "Simulation and analysis of ultrafast-laser-pulse-induced plasma generation in fused silica," *Opt. Eng.* **47**(5), 054302 (2008).

[9] J. R. Gulley, S. W. Winkler, and W. M. Dennis, "Simulation and analysis of ultrafast laser pulse induced plasma generation in dielectric materials," *Enabling Photonics Technologies for Defense, Security, and Aerospace Applications III* **6572**(1), 65720R (2007).

[10] C. B. Schaffer, *Interaction of femtosecond laser pulses with transparent materials*. PhD thesis, Harvard University, Cambridge, Massachusetts (2001).

[11] B. Rethfeld, "Unified model for the free-electron avalanche in laser-irradiated dielectrics," *Phys. Rev. Lett.* **92**(18), 187401 (2004).

[12] B. C. Stuart, M. D. Feit, S. Herman, A. M. Rubenchik, B. W. Shore, and M. D. Perry, "Nanosecond-to-femtosecond laser-induced breakdown in dielectrics," *Phys. Rev. B* **53**, 1749–1761 (1996).

[13] R. Trebino, *Frequency-Resolved Optical Gating: The Measurement of Ultrashort Pulses*, Springer (2002).

[14] S. W. Winkler, I. M. Burakov, R. Stoian, N. M. Bulgakova, A. Husakou, A. Mermillod-Blondin, A. Rosenfeld, D. Ashkenasi, and I. V. Hertel, "Transient response of dielectric materials exposed to ultrafast laser radiation," *Appl. Phys. A* **V84**(4), 413–422 (2006).

[15] C. B. Schaffer, A. Brodeur, J. F. Garcia, and E. Mazur, "Micromachining bulk glass by use of femtosecond laser pulses with nanojoule energy," *Opt. Lett.* **26**, 93–95 (2001).

[16] C. B. Schaffer, A. O. Jamison, and E. Mazur, "Morphology of femtosecond laser-induced structural changes in bulk transparent materials," *Appl. Phys. Lett.* **84**, 1441–1443 (2004).

[17] C. B. Schaffer and E. Mazur, "Micromachining using ultrashort pulses from a laser oscillator," *Opt. and Phot. News* **12**, 20–23 (2001).

[18] A. Q. Wu, I. H. Chowdhury, and X. Xu, "Plasma formation in fused silica induced by loosely focused femtosecond laser pulse," *Appl. Phys. Lett.* **88**(11), 111502 (2006).

[19] A. Q. Wu, I. H. Chowdhury, and X. Xu, "Femtosecond laser absorption in fused silica: Numerical and experimental investigation," *Phys. Rev. B* **72**(8), 085128 (2005).

[20] A. Couairon, S. Tzortzakis, L. Bergé, M. Franco, B. Prade, and A. Mysyrowicz, "Infrared femtosecond light filaments in air: simulations and experiments," *J. Opt. Soc. Am. B* **19**(5), 1117–1131 (2002).

[21] A. Vinçotte and L. Bergé, "$\chi(5)$ susceptibility stabilizes the propagation of ultrashort laser pulses in air," *Phys. Rev. A* **70**, 061802 (2004).

[22] G. S. He and S. H. Liu, *Physics of Nonlinear Optics*, World Scientific Publishing Co. Pte. Ltd. (1999).

[23] J. D. Jackson, *Classical Electrodynamics*, John Wiley and Sons, Inc., 3rd ed. (1998).

[24] J. H. Marburger, "Self-focusing: Theory," *Prog. in Qaunt. Electr.* **4**, 35–110 (1975).

[25] G. P. Agrawal, *Nonlinear Fiber Optics*, Academic Press (2001).

[26] T. Brabec and F. Krausz, "Intense few-cycle laser fields: Frontiers of nonlinear optics," *Rev. Mod. Phys.* **72**, 545–591 (2000).

[27] A. Couairon and L. Berge, "Modeling the filamentation of ultra-short pulses in ionizing media," *Phys. Plasmas* **7**(1), 193–209 (2000).

[28] K. W. DeLong, C. L. Ladera, R. Trebino, B. Kohler, and K. R. Wilson, "Ultrashort-pulse measurement using noninstantaneous nonlinearities: Raman effects in frequency-resolved optical gating," *Opt. Lett.* **20**(5), 486–488 (1995).

[29] K. J. Blow and D. Wood, "Theoretical description of transient stimulated raman scattering in optical fibers," *J. Quant. Electr.* **25**, 2665–2673 (1989).

[30] J.-C. Diels and W. Rudolf, *Ultrashort Laser Pulse Phenomenon: Fundamentals, Techniques, and Applications on a Femtosecond Time Scale*, Academic Press, 2nd ed. (2006).

[31] T. Brabec and F. Krausz, "Nonlinear optical pulse propagation in the single-cycle regime," *Phys. Rev. Lett.* **78**, 3282–3285 (1997).

[32] J. K. Ranka and A. L. Gaeta, "Breakdown of the slowly varying envelope approximation in the self-focusing of ultrashort pulses," *Opt. Lett.* **23**, 534–536 (1998).

[33] S. T. Cundiff, "Phase stabilization of ultrashort optical pulses," *J. of Phys. D* **35**(8), R43–R59 (2002).

[34] D. M. Sullivan, *Electromagnetic Simulation Using the FDTD Method*, IEEE Computer Society Press, 1st ed. (2000).

[35] K. F. Brennan, *The Physics of Semiconductors: with applications to optoelectronic devices*, Cambridge University Press (1999).

[36] L. H. Holway, "Temporal behavior of electron distributions in an electric field," *Phys. Rev. Lett.* **28**, 280–283 (1972).

[37] D. Huang, T. Apostolova, P. M. Alsing, and D. A. Cardimona, "High-field transport of electrons and radiative effects using coupled force-balance and fokker-planck equations beyond the relaxation-time approximation," *Phys. Rev. B* **69**, 075214 (2004).

[38] D. Huang, P. M. Alsing, T. Apostolova, and D. A. Cardimona, "Coupled energy-drift and force-balance equations for high-field hot-carrier transport," *Phys. Rev. B* **71**, 195205 (2005).

[39] D. Huang, P. M. Alsing, T. Apostolova, and D. A. Cardimona, "Effect of photon-assisted absorption on the thermodynamics of hot electrons interacting with an intense optical field in bulk gaas," *Phys. Rev. B* **71**, 045204 (2005).

[40] A. Kaiser, B. Rethfeld, M. Vicanek, and G. Simon, "Microscopic processes in dielectrics under irradiation by subpicosecond laser pulses," *Phys. Rev. B* **61**, 11437–11450 (2000).

[41] L. H. Holway and D. W. Fradin, "Electron avalanche breakdown by laser radiation in insulating crystals," *J. Appl. Phys.* **46**(1), 279–291 (1975).

[42] W. R. McKinnon, "Fokker–planck approach to extending the one-flux method of carrier transport in semiconductors to variable energies," *J. Appl. Phys.* **94**(8), 4986–4994 (2003).

[43] B. Jacob, P. N. Robson, J. P. R. David, and G. J. Rees, "Fokker–planck approach to impact ionization distributions in space and time," *J. Appl. Phys.* **91**(8), 5438–5441 (2002).

[44] C. Jacoboni and P. Lugli, *The Monte Carlo Method for Semiconductor Device Simulation*, Springer-Verlag/Wien (1998).

[45] H. Risken, *The Fokker-Planck Equation: Methods of Solutions and Applications*, Springer-Verlag (1984).

[46] S. Skupin and L. Berge, "Self-guiding of femtosecond light pulses in condensed media: Plasma generation versus chromatic dispersion," *Physica D* **220**, 14–30 (2006).

[47] G.-W. Chern, J.-F. Chang, and L. A. Wang, "Modeling of nonlinear pulse propagation in periodic and quasi-periodic binary long-period fiber gratings," *J. Opt. Soc. Am. B* **19**(7), 1497–1508 (2002).

[48] S. Longhi, "Extended matrix method for gaussian pulse propagation and generalized mode-locking master equation," *Opt. Comm.* **188**(1-4), 239 – 253 (2001).

[49] M. Geissler, G. Tempea, A. Scrinzi, M. Schnürer, F. Krausz, and T. Brabec, "Light propagation in field-ionizing media: Extreme nonlinear optics," *Phys. Rev. Lett.* **83**, 2930–2933 (1999).

[50] C. M. Liebig and W. M. Dennis, "Simulation of interactions of high-intensity ultrashort pulses with dielectric filters," *Opt. Eng.* **46**(2), 023801 (2007).

[51] Y. R. Shen, "Self-focusing: Experimental," *Prog. in Qaunt. Electr.* **4**, 1–34 (1975).

[52] A. Couairon, G. Mechain, S. Tzortzakis, M. Franco, B. Lamouroux, B. Prade, and A. Mysyrowicz, "Propagation of twin laser pulses in air and concatenation of plasma strings produced by femtosecond infrared filaments," *Opt. Comm.* **225**, 177–192 (2003).

[53] A. Couairon and L. Bergé, "Light filaments in air for ultraviolet and infrared wavelengths," *Phys. Rev. Lett.* **88**, 135003 (2002).

[54] S. Skupin, G. Stibenz, L. Berge, F. Lederer, T. Sokollik, M. Schnurer, N. Zhavoronkov, and G. Steinmeyer, "Self-compression by femtosecond pulse filamentation: Experiments versus numerical simulations," *Phys. Rev. E* **74**, 056604 (2006).

[55] B. Rethfeld, "Free-electron generation in laser-irradiated dielectrics," *Phys. Rev. B* **73**(3), 035101 (2006).

[56] L. Jiang and H.-L. Tsai, "Energy transport and nanostructuring of dielectrics by femtosecond laser pulse trains," *J. Heat Transfer* **128**(9), 926–933 (2006).

[57] G. E. Uhlenbeck and L. S. Ornstein, "On the theory of the brownian motion," *Phys. Rev.* **36**, 823–841 (1930).

[58] F. A. Lyman, "Expansion of the fokker-planck equation in spherical harmonics," tech. rep., Lewis Research Center, NASA (1965).

[59] W. H. Press, S. A. Teukolsky, W. T. Vetterling, and B. P. Flannery, *Numerical Recipes in Fortran 77*, vol. 1, Cambridge University Press, second ed. (1986).

[60] S. W. Winkler, *Nondestructive Interaction of Ultrafast Laser Pulses with Transparent Dielectrics*. PhD thesis, The University of Georgia, Athens, GA 30602 (2009).

[61] A. Vogel, J. Noack, G. Huttman, and G. Paltauf, "Mechanisms of femtosecond laser nanosurgery of cells and tissues," *Appl. Phys. B* **81**, 1015–1047 (2005).

[62] Y. Shimotsuma, P. G. Kazansky, J. Qiu, and K. Hirao, "Self-organized nanogratings in glass irradiated by ultrashort light pulses," *Phys. Rev. Lett.* **91**, 247405 (2003).

[63] X. Zhu, A. Y. Naumov, D. M. Villeneuve, and P. B. Corkum, "Influence of laser parameters and material properties on micro drilling with femtosecond laser pulses," *Appl. Phys. A* **V69**(0), S367–S371 (1999).

[64] A. Couairon, L. Sudrie, M. Franco, B. Prade, and A. Mysyrowicz, "Filamentation and damage in fused silica induced by tightly focused femtosecond laser pulses," *Phys. Rev. B* **71**(12), 125435 (2005).

[65] T. Q. Jia, H. Y. Sun, X. X. Li, D. H. Feng, C. B. Li, S. Z. Xu, R. X. Li, Z. Z. Xu, and H. Kuroda, "The ultrafast excitation processes in femtosecond laser-induced damage in dielectric omnidirectional reflectors," *J. Appl. Phys.* **100**, 023103 (2006).

[66] A. Rosenfeld, M. Lorenz, R. Stoian, and D. Ashkenasi, "Ultrashort-laser-pulse damage threshold of transparent materials and the role of incubation," *Appl. Phys. A* **V69**(0), S373–S376 (1999).

[67] J. Satsuma and N. Yajima, "Initial value problems of one dimentional self-modulation of nonlinear waves in dispersive media," *Prog. Theoret. Phys. Supp.* **55**, 284–306 (1974).

[68] A. Couairon, E. Gaizauskas, D. Faccio, A. Dubietis, and P. D. Trapani, "Nonlinear x-wave formation by femtosecond filamentation in kerr media," *Phys. Rev. E* **73**(1), 016608 (2006).

[69] S. Tzortzakis, L. Sudrie, M. Franco, B. Prade, A. Mysyrowicz, A. Couairon, and L. Bergé, "Self-guided propagation of ultrashort ir laser pulses in fused silica," *Phys. Rev. Lett.* **87**, 213902 (2001).

[70] L. Sudrie, A. Couairon, M. Franco, B. Lamouroux, B. Prade, S. Tzortzakis, and A. Mysyrowicz, "Femtosecond laser-induced damage and filamentary propagation in fused silica," *Phys. Rev. Lett.* **89**, 186601 (2002).

[71] P. Polesana, M. Franco, A. Couairon, D. Faccio, and P. D. Trapani, "Filamentation in kerr media from pulsed bessel beams," *Phys. Rev. A* **77**(4), 043814 (2008).

[72] P. Polesana, A. Dubietis, M. A. Porras, E. Kucinskas, D. Faccio, A. Couairon, and P. D. Trapani, "Near-field dynamics of ultrashort pulsed bessel beams in media with kerr nonlinearity," *Phys. Rev. E* **73**(5), 056612 (2006).

[73] S. Akturk, C. D'Amico, M. Franco, A. Couairon, and A. Mysyrowicz, "Pulse shortening, spatial mode cleaning, and intense terahertz generation by filamentation in xenon," *Phys. Rev. A* **76**(6), 063819 (2007).

[74] A. L. Gaeta, "Catastrophic collapse of ultrashort pulses," *Phys. Rev. Lett.* **84**, 3582–3585 (2000).

[75] X. Mao, S. S. Mao, and R. E. Russo, "Imaging femtosecond laser-induced electronic excitation in glass," *Appl. Phys. Lett.* **82**(5), 697–699 (2003).

[76] D. Giguère, G. Olivié, F. Vidal, S. Toetsch, G. Girard, T. Ozaki, J.-C. Kieffer, O. Nada, and I. Brunette, "Laser ablation threshold dependence on pulse duration for fused silica and corneal tissues: experiments and modeling," *J. Opt. Soc. Am. A* **24**(6), 1562–1568 (2007).

[77] Q. Sun, H. Jiang, Y. Liu, Z. Wu, H. Yang, and Q. Gong, "Measurement of the collision time of dense electronic plasma inducedby a femtosecond laser in fused silica," *Opt. Lett.* **30**(3), 320–322 (2005).

[78] C. Courtois, A. Couairon, B. Cros, J. R. Marques, and G. Matthieussent, "Propagation of intense ultrashort laser pulses in a plasma filled capillary tube: Simulations and experiments," *Phys. Plasmas* **8**(7), 3445–3456 (2001).

[79] S. S. Mao, F. Quere, S. Guizard, X. Mao, R. E. Russo, G. Petite, and P. Martin, "Dynamics of femtosecond laser interactions with dielectrics," *Appl. Phys. A* **V79**(7), 1695–1709 (2004).

[80] L. V. Keldysh, "Ionization in the field of a strong electromagnetic wave," *Sov. Phys. JETP* **20**(5), 1307 (1965).

[81] M. Abramowitz and I. A. Stegun, *Handbook of Mathematical Functions*, Dover, New York, tenth ed. (1964).

[82] V. E. Gruzdev, "Analysis of the transparent-crystal ionization model developed by L. V. Keldysh*," *J. Opt. Technol.* **71**, 504–508 (2004).

[83] B. C. Stuart, M. D. Feit, A. M. Rubenchik, B. W. Shore, and M. D. Perry, "Laser-induced damage in dielectrics with nanosecond to subpicosecond pulses," *Phys. Rev. Lett.* **74**, 2248–2251 (1995).

[84] J. K. Chen, D. Y. Tzou, and J. E. Beraun, "Numerical investigation of ultrashort laser damage in semiconductors," *Intern. J. Heat Mass Trans.* **48**, 501–509 (2005).

[85] H. R. Reiss, "Mixed quantum and classical processes in strong fields," *Phys. Rev. A* **75**, 013413 (2007).

[86] B. Rethfeld, V. V. Temnov, K. Sokolowski-Tinten, P. Tsu, D. von der Linde, S. I. Anisimov, S. I. Ashitkov, and M. B. Agranat, "Superfast thermal melting of solids under the action of femtosecond laser pulses," *J. Opt. Technol.* **71**, 348–352 (2004).

[87] R. E. Samad and N. D. Vieira, "Geometrical method for determining the surface damage threshold for femtosecond laser pulses," *Laser Physics* **V16**(2), 336–339 (2006).

[88] D. vonderLinde and H. Schuler, "Breakdown threshold and plasma formation in femtosecond laser-solid interaction," *J. Opt. Soc. Am. B* **13**, 216–222 (1996).

[89] D. E. Roskey, M. Kolesik, J. V. Moloney, and E. M. Wright, "The role of linear power partitioning in beam filamentation," *Appl. Phys. B* **V86**(2), 249–258 (2007).

[90] V. Kudriagov, E. Gaizauskas, and V. Sirutkaitis, "Beam transformation and permanent modification in fused silica induced by femtosecond filaments," *J. Opt. Soc. Am. B* **22**, 2619–2627 (2005).

[91] M. Mero, J. Liu, W. Rudolph, D. Ristau, and K. Starke, "Scaling laws of femtosecond laser pulse induced breakdown in oxide films," *Phys. Rev. B* **71**(11), 115109 (2005).

[92] R. M. Wood, *Laser-induced Damage of Optical Materials*, Series in Optics and Optoelectronics, Institute of Physics Publishing (2003).

[93] P. Hannaford, Ed., *Femtosecond Laser Spectroscopy*, Springer Science+Business Media, Inc. (2005).

[94] L. H. Holway, "High-frequency breakdown in ionic crystals," *J. Appl. Phys.* **45**(2), 677–683 (1974).

[95] M. Sparks, D. L. Mills, R. Warren, T. Holstein, A. A. Maradudin, L. J. Sham, E. Loh, and D. F. King, "Theory of electron-avalanche breakdown in solids," *Phys. Rev. B* **24**, 3519–3536 (1981).

[96] D. Arnold, E. Cartier, and D. J. DiMaria, "Acoustic-phonon runaway and impact ionization by hot electrons in silicon dioxide," *Phys. Rev. B* **45**(3) (1992).

[97] V. E. Gruzdev and J. K. Chen, "Laser-induced ionization and intrinsic breakdown of wide band-gap solids," *Appl. Phys. A* **90**(2), 255–261 (2008).

[98] V. E. Gruzdev, "Photoionization rate in wide band-gap crystals," *Phys. Rev. B* **75**(20), 205106 (2007).

[99] G. B. Arfken and H. J. Weber, *Mathematical Methods for Physicists*, Academic Press, 5th ed. (2001).

[100] C. L. Arnold, A. Heisterkamp, W. Ertmer, and H. Lubatschowski, "Computational model for nonlinear plasma formation in high na micromachining of transparent materials and biological cells," *Opt. Express* **15**(16), 10303–10317 (2007).